A FEASIBILITY STUDY OF INCORPORATING SURFACE TENSION ELEMENTS TO IMPROVE THE EFFICIENCY OF RESIDENTIAL CLOTHES DRYERS

by

MICHAEL PATRICK COCHRAN

B.S., Kansas State University, 2005

A THESIS

submitted in partial fulfillment of the requirements for the degree

MASTER OF SCIENCE

Department of Mechanical and Nuclear Engineering
College of Engineering

KANSAS STATE UNIVERSITY
Manhattan, Kansas

2007

Approved by:

Major Professor
Bruce Babin

Abstract

A Surface Tension Element (STE), device was successfully constructed and tested as the primary moisture removal device in a condensing dryer. The STE was tested via the SAE ARP901 bubble-point test method and resulted in an average micron rating of 46.8 microns. The operation of the STE was compared to that of the typical air-to-air heat exchanger/condenser used in condensing dryers. The total power consumption and IEC efficiency of each case were averaged and compared. The results indicated that the STE used an average of 0.616 kilowatt-hours per kilogram dry laundry while the air-to-air heat exchanger/condenser used an average of 0.643 kWh/kg. This resulted in an improvement of the European efficiency label from class C to Class B. An analytical model was also constructed that well predicted the operation of the STE under steady state conditions.

Table of Contents

List of Figures

List of Tables

Acknowledgements

I would like to acknowledge and thank Dr. Bruce Babin for his support, guidance, and mentorship. Without his enthusiasm for the understanding of science, I would not have pursued this advanced degree and thus forfeited this growing experience. He often brought the "big picture" into view, allowing me to see the appropriate path to take. I also would like to thank Dr. Steve Eckels for his support and guidance on this project and his kind generosity in providing equipment and additional financial funding for the project. He always had good insight into the physics of the process and always asked thought-provoking questions that helped me to think through the problem at hand. I would like to thank Dr. Hosni was very willing to spend his precious time mentoring me on this project. I would like to thank Jared Goodnight for his preparatory work in Surface Tension Elements, his willingness to familiarize myself with the technology, diligent work bubble-point testing the STE modules, and his help throughout the entire project. Finally, I would like to thank Gerard Daniel Worldwide for their generous donation of the wire mesh used to construct the Surface Tension Elements.

Dedication

I would like to dedicate this work first and foremost to my role model and savior Jesus Christ, the Father, and the Holy Spirit. Without your divine craftsmanship of my intellect and passions, I would not have excelled in this field of study. Thank you for your grace in my life and this chance to receive this additional education.

I would also like to dedicate this work to my wife Susan who lovingly stood by my side through this degree. Your love and encouragement are more than I deserve. I only hope that I will have the opportunity to show you how much you mean to me.

CHAPTER 1 - Introduction

1.1 Today's Energy Crisis

During the industrial revolution, when humanity first began to realize the energy potential available in the earth's natural fuels, no one could have foreseen how the world could grow to be entirely dependent on them as a way of life. Nearly every human alive today has grown up during a period of time when energy resources have been plentiful and the question of not having them at our fingertips is very far from our minds. In the 1970s, a different story began to emerge – humanity's current rate of energy consumption cannot be supported indefinitely. People began to look to new ways of generating energy, renewable energy resources, energy efficiency, other technologies, and most importantly, lifestyle changes. That time came and went as new energy reserves were found, energy and fuel prices dropped, people's old lifestyles could economically continue, and the problem slipped out of the public's consciousness. The 1970s energy crisis was nature's warning to humanity telling us to not abuse it – a warning that has not been taken very seriously. The United States in particular is power hungry – hybrid technology in vehicles is being used to make engines that have more horsepower instead of higher fuel economy. The scientific community needs to be focusing on how to reduce our energy consumption, not increase it! Today, energy resources are dropping at alarming rates due to the massive global demand for them. Projections of how long the reserves will last are not encouraging either. The public is becoming increasingly aware that this time, the energy crisis is for real. The time for change is at hand.

1.1 Inefficiencies in today's Driers

Historically, the practice of washing one's clothes was an extremely labor and time intensive process accomplished entirely by one's own strength and the natural environment. As the industrialized world has become increasingly sensitive of one's optimal time management, washing and drying laundry by hand has become a nearly obsolete practice as automated machines have been developed to accomplish this mind-numbing task. The first machine invented to aid the practice was called a "mangle", where clothes were pressed in order to extract excess water content from the textile fibers prior to ironing (Watts, 1991). These machines are

recorded of being in use as early as 1696. This originally heavy machine evolved from needing to be operated by a strong man to being simple and easy enough to be operated by a single maid. Figure 1.1 shows a mangle manufactured around 1934.

Figure 1.1 Norahammars Bruk Model 3005-2 Mangle:
Taken from: http://en.wikipedia.org/wiki/Mangle_(machine)

The Germans later invented a centrifuging technique to remove the moisture content from and to dry clothes – a concept that was later refined by the Americans and is incorporated in vertical axis washing machines available today. One limitation of all of the mangle machines and centrifuging machines is that a typically large percentage of water remained absorbed in the clothes. A typical machine could remove no more than a remaining moisture content of 100% of the cloths dry weight. The Europeans later developed a centrifuging design where the washing axis was reoriented to be horizontal. This resulted in much less water consumption of the clothes, and allowed for less energy consumption for washing the clothes. Through later development, the centrifuging speeds increased as vibration damping strategies were implemented and gradual speed increases were used to balance the load. Today's washing machines incorporate this centrifuging technique at the end of the washing cycle in order to remove excess water. Centrifuging speeds in compact washing machines of up to 3000 rpm

allow for the remaining moisture content to be reduced to 45-50% of the cloths dry weight. This represents a significant amount of water that the dryer does not need to evaporate, and hence means energy savings for the entire laundry process.

The ease of use of modern washing and drying machines has made them a necessity from the consumer's point of view. The old habit of wearing a set of clothing more than once is no longer common since there are now fewer repercussions of frequent washing and drying. Instead of occupying several days' worth of intensive work, washing a set of clothes can be completed in several hours with minimal human interaction. All of this is to say that a substantial amount of electrical and fossil fuel energy is consumed for laundry purposes.

Current energy consumption practices are, however, at the precipice of change as the public becomes increasingly aware of the imminent energy crisis to occur when the world's fossil fuel reserves become depleted in the near future. Increases in fuel costs due to lack of supply are causing society to give more thought to just *how* necessary various energy intensive practices are and *if* more efficient means of accomplishing these processes can be implemented. The 2005 Annual Energy Review compiled by the Department of Energy tells us that 57% of all households contain electric clothes dryers and 17% contain gas clothes dryers (Department of Energy, 2007). According to the U. S. Department of Energy's 2001 Residential Energy Consumption Survey, electrical clothes dryers account for roughly 5.8% of total energy consumption for households (Department of Energy, 2007). It therefore stands to reason that current clothes drying technology is such a procedure; energy is needlessly wasted and significant energy savings could be achieved through careful implementation of thermodynamic principals.

1.2 European Efficiency Requirements

High population concentrations in Europe may be one of the primary motivations for Europeans to be concerned not only about space efficiency, but also energy efficiency. Smaller vehicles present in these countries, compared to the U.S., hint at the underlying motto, "smaller is better". This philosophy is clearly evident in the area of residential clothes dryer design and energy efficiency. Europeans have actively pursued small footprint, higher efficiency dryer designs. The EU public has readily accepted each wave of improvements, even if it means longer drying times. In the U.S., residential clothes dryer manufacturers are not currently

required to display the energy consumption of the dryer as is done for washing machines, refrigerators, and other appliances. In the store, a dryer manufacturer can make high-efficiency claims, but the consumer has no information to tell them that this "high-efficiency" model actually is incredibly inefficient compared to other drying technologies that are currently available.

In the European Union, the story is different. Dryers are divided up into classes based on the amount of energy required per unit mass of water removed from a standardized test load. The classes are labeled from A to G with A being the most efficient and G being the least. The energy label requirements for the various ratings are displayed in Table 1.1.

Table 1.1 EU Energy Label Specifications [Market Transformation Programme, 2006]

EU Energy Label	Condensing Dryer Energy Consumption (kWh / kg)	Air-Vented Dryer Energy Consumption (kWh / kg)
A	EC <= 0.55	EC <= 0.51
B	0.55 < EC <= 0.64	0.51 < EC <= 0.59
C	0.64 < EC <= 0.73	0.59 < EC <= 0.67
D	0.73 < EC <= 0.82	0.67 < EC <= 0.75
E	0.82 < EC <= 0.91	0.75 < EC <= 0.83
F	0.91 < EC <= 1.00	0.83 < EC <= 0.91
G	EC > 1.00	EC > 0.91

One feature to be pointed out about the above table is the fact that the air-vented dryers are held to more stringent classification rules than condensing dryers are.

1.3 Commercially Available Technologies

This section will describe drying technologies currently available to the public. There are of course additional techniques that are not mentioned here, for example the traditional clothesline air drying, and experimental methods, but for simplicity's sake, only the widespread methods are described here. All of the dryers of clothes that are described here fall under the category of "tumble dryers", where the clothes are placed in a rotating drum that causes the clothes to "tumble" and have plenty of contact with the air in the drum.

1.3.1 Dryers not just for clothes

Some of the most scientifically approached drying problems are those of paper, grain, and food drying. This could be attributed to the fact that both of these commodities are typically mass produced, thus the drying efficiency is relatively important. Savings in both drying time and energy easily are translated into increased profits for the industry responsible for the drying process.

1.3.1.1 Paper Dryers

Paper drying in industry is an extremely important process in that it significantly affects the end product. The paper's integrity, roughness, color, and other parameters can be affected by the drying process. The drying of a sheet of paper being processed through an assembly line of various heated rollers is also a very repeatable process that lends itself to mathematical modeling. The velocity, paper composition, and physical size, and the drying environment is relatively easy to quantify. For these reasons, this problem has been quite extensively pursued by various researchers. The current industry process involves rolling paper through a series of hollow rollers that are heated internally by steam. As the steam condenses on the internal surface of the roller, the heat of vaporization is conducted through the roller wall and to the paper's surface. This activity raises the paper's temperature and encourages the rapid evaporation of the paper's water content. Low-humidity air is then forced over the surface of the paper absorbing the moisture and carrying it away from the paper. Slight variations of this process are also used to dry various other textiles besides paper.

A newer approach to paper and textile drying was proposed by van Deventer (van Deventer, 1997) in an effort to make the process more efficient. He proposed to blow superheated steam directly onto the textile surface. This would be done at a rate that allows the superheated steam to completely vaporize the liquid moisture within the textile without reducing the superheated steam's internal energy below the saturated vapor state. The remaining steam just above the saturated vapor state is then drawn away from the textile. A portion of the steam is reheated to continue the drying process while the remaining portion can be reused for other heating purposes within the plant. Deventer calculates that with this method and utilizing the waste heat present in the recovered steam, up to 50% of the energy input for the drying process can be recovered for paper and 75% for textiles. It is to be noted that this method is intended for

large production plants and much thought would have to be given to it in order to make it feasible for residential clothes dryers.

1.3.2 Venting Tumble Dryers

Venting dryers are prevalent in the United States, and are used internationally as well, though they do not dominate the market, as is the case in the United States. Many U.S. citizens don't even realize that there are other types of dryers besides the common venting dryer.

Venting dryers operate by drawing air into the machine from the surrounding room, heating the air either by using a resistive heater or by combusting some type of fuel such as natural gas. The next stage is to draw the heated air into the rotating drying drum where it comes in contact with damp clothing and facilitates the evaporation of liquid water from the textiles. The humid air is then drawn out of the drum through a lint filter of some type, through a blower of some type, and is finally exhausted to the environment through ducted tubing. A flow schematic of the system is shown below in Figure 1.2.

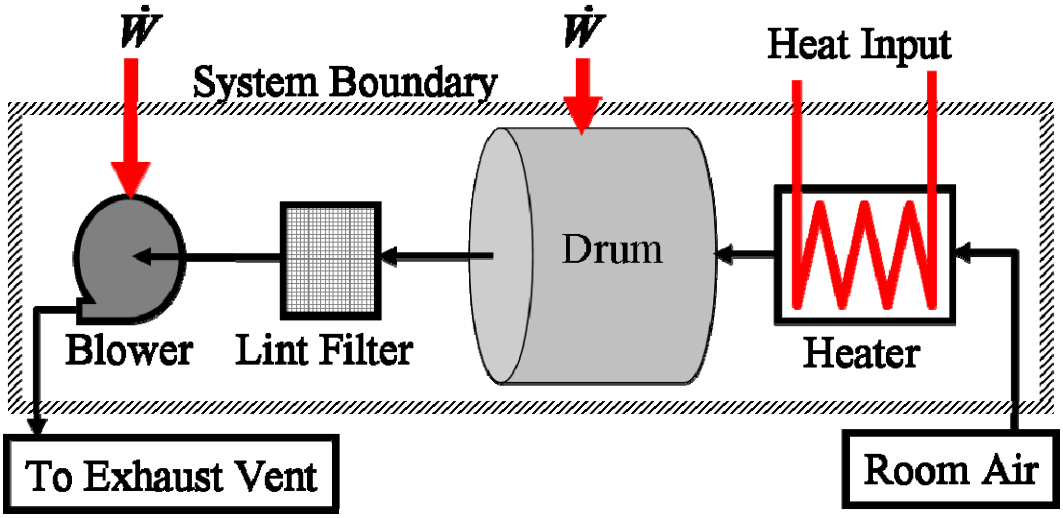

Figure 1.2 Venting Dryer Flow Schematic

It is a simple matter to see where the major inefficiency lies in this design – the key fact that the energy of the exiting humid air is not recovered in the slightest bit clues us in that this design is far from optimal. In more temperate geographical regions, room air being drawn into the dryer is exhausted out of the house which means that the household heating system must compensate for the removed air by additional heating. The obvious solution to eliminating the additional heating costs is to vent the humid dryer air inside the household, but there are two problems associated with this, however. The first problem is lint that was able to bypass the

dryer's lint filter will escape into the house and become a mess. This problem can be circumvented by the installation of a filter device, much like a sock, that fits over the end of the dryer's exit duct and can greatly reduce the amount of lint escaping into the household. The second issue with venting the dryer's exhaust inside the house is the addition of the humidity content of the dryer's exhaust air that can be either comforting or irritating based on an individual's living environment preferences.

1.3.3 Heat Pump Tumble Dryer

The Heat Pump Dryer is a relatively new concept that has only recently come to the commercial market. The first patents were filed in 1973 and the first concepts appeared in 1993 at Domotechnica, the International Trade Fair for Household Appliances (Dahlman, 2006). In 1997, Electrolux introduced the first dryer to the market, but there were significant problems that prohibited the product from succeeding commercially. Among the problems were manufacturability, high price, and poor drying characteristics. Since that time, many improvements have been made to the original concept that are mass-producible. Switzerland has become a major advocate for the heat pump dryer and has implemented various strategies to encourage its use. S.A.F.E., the *Swiss Agency for Efficient Energy Use* performed comparison studies on the efficiencies of heat pump driers and found that they were vastly superior to other drying technology on the market, consuming less than ½ of the energy as conventional dryers (Bush, 2006).

The heat pump dryer is a closed-loop drying system that removes the moisture from the drying air (henceforth called the drying fluid). The concept is a variation of the condenser dryer, which is described in the next section, but has significant differences also. A flow schematic of the dyer is shown in Figure 1.3.

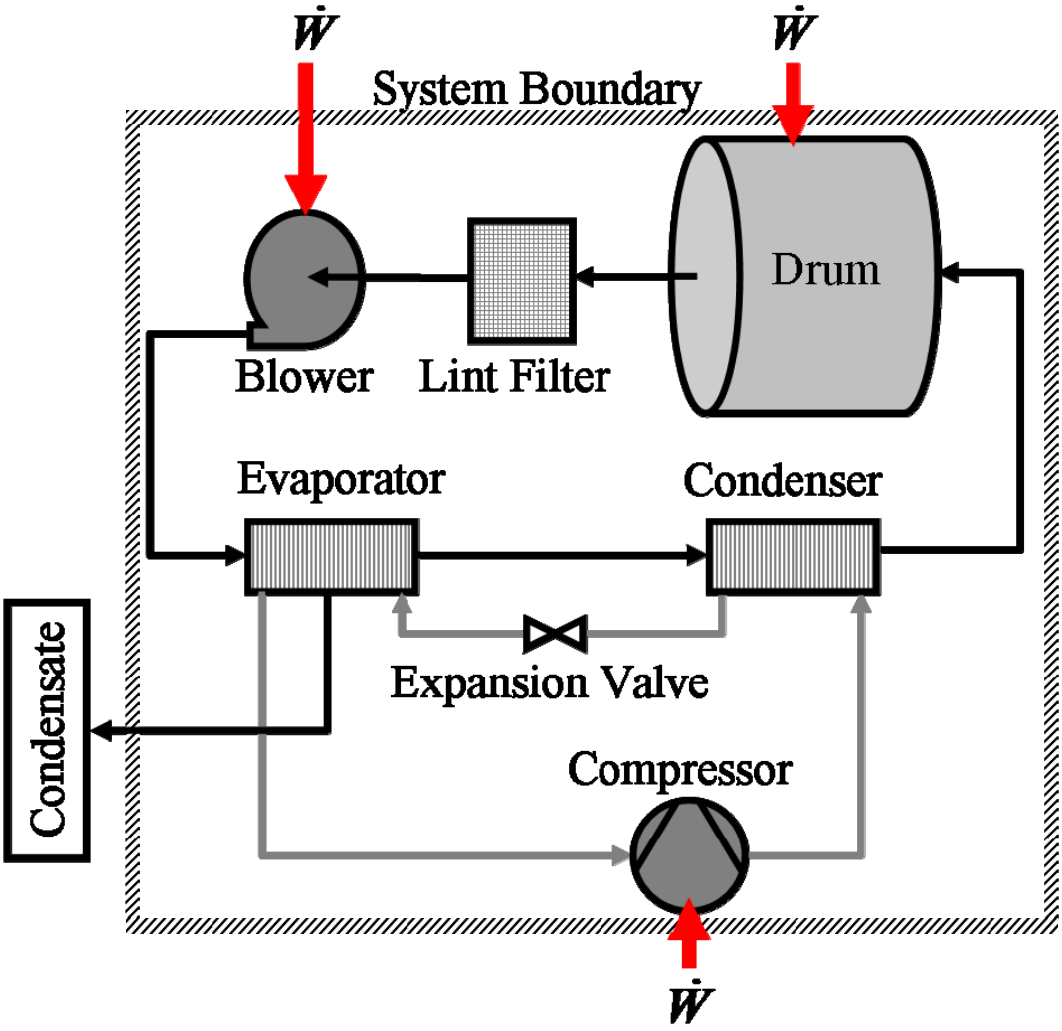

Figure 1.3 Heat Pump Dryer Flow Schematic

The dryer drum, lint filter, and blower are nearly identical to the venting dryer, but substantial differences occur after the air exits the blower. A vapor-compression cycle heat pump is inserted into the flow loop such that the high-humidity exiting the drum and blower is blown through the heat pump's evaporator. The temperature of the drying fluid through the evaporator is reduced to below its dew point, causing excess moisture in the drying fluid to condense on the evaporator's cooling fins. The condensate is then collected and removed from the system. After the air passes through the evaporator, it is then blown through the heat pump's condenser where heat is added to the drying fluid.

If a control volume boundary is drawn as is shown above in Figure 1.3, an energy balance is constructed, and heat transfer losses across the boundary are assumed to be negligible, we can see that the primary energy interactions with the surroundings of the dryer are the work required

for the blower, drum rotation motor, and heat pump compressor, as well as the enthalpy times the mass flow rate of the exiting condensate. We see that in this design, the energy required to evaporate the liquid water from the textiles in the drum is recovered and reused to continue the evaporation process. In the end, the major technological concept in this design is that the latent heat of vaporization of the water can be recovered instead of being ejected wastefully to the environment.

This concept's efficiency also benefits from the fact that the heat pump not only functions as a way to move thermal energy, but the losses in the compressor of the heat pump add additional energy to the drying fluid – aiding the drying process. This can be seen from the definition of the coefficient of performance, γ, for a heat pump:

$$\gamma_{heating} = \frac{Q_{out}}{W_{cycle}} = \frac{Q_{out}}{Q_{out} - Q_{in}} \qquad \textbf{Equation 1}$$

where W_{cycle} is the work required to operate the compressor. Typically, heat pumps operating in heating mode have coefficients of performance around three or higher.

1.3.4 Condenser Tumble Dryer

Condenser (or condensing) dryers have not yet appeared in the United States to date, to the author's best knowledge that is, however, they are common place in the EU. These dryers are generally more compact and have the ability to be placed virtually at any location within the house because they do not require a venting duct to the exterior of the dwelling. If one were to compare venting and condensing dryers in the EU, on average one would find that the condenser dryers consume a little more energy per load than venting versions do (Market Transformation Programme, 2006). This could be attributed to the fact that the air venting dryers draw in from their surroundings, holds much more moisture content once heated than the high-humidity air typically present in a condenser dryer (post reheating). This air that is used by the venting dryer must be replaced for by the house's heating/cooling system. Since the household heating system energy consumption is not measured as part of the dryer's performance, this represents a slight error in the dryer's true use of energy required to dry a load of clothes. This is the reason for penalizing venting dryers more for their energy efficiency labels in the EU.

Like the heat pump dryer, the condenser dryer also uses a closed-loop drying process. An air-to-air cross-flow heat exchanger is incorporated in the flow loop to de-humidify the drying fluid. Room air is blown across one side of the heat exchanger and drying fluid is blown across the other side. Since the drying fluid entering the heat exchanger is typically around 55°C and 100% relative humidity and the room air is usually below 23°C, the room air essentially cools the heat exchanger's fins and causes a reduction in temperature of the drying fluid, which results in moisture content removal from the drying fluid. This process prevents the drying fluid from becoming too saturated with water vapor and ensures that evaporation from the cloth load continues. Condensate that occurs on the heat exchanger's fins is blow off the fins, drains out of the heat exchanger's compartment, collects in an intermediary holding tank, and finally is pumped out to a drain or a larger holding tank for periodic manual removal. This feature allows the dryer to be placed anywhere in the house. For simplicity's sake though, placement next to a drain is advantageous since it does not require the user to periodically empty the large condensate holding tank. A flow schematic of the system is shown below in Figure 1.4.

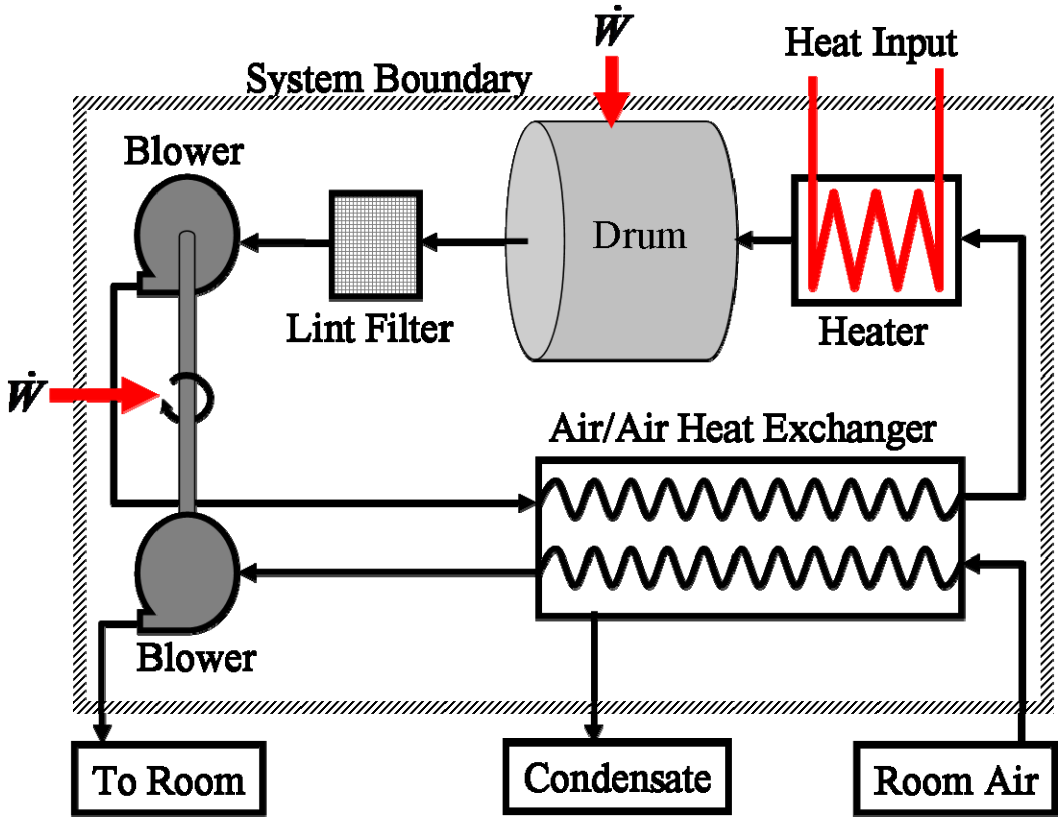

Figure 1.4 Condenser Dryer Flow Schematic

Because of their closed loop configuration, condenser dryers operate at a substantially higher drum inlet humidity ratio than their venting dryer counterparts (in the range of one order of magnitude greater), however this seemingly does not greatly hinder water evaporation from the textiles. Excess water that has not exited through the compartment's drain can sit stagnant between drying loads and can create problems. One issue that sometimes comes up is that of mildew growing in the condenser compartment. This problem can be avoided though with periodic maintenance of the dryer's heat exchanger. In temperate environments, condenser driers do well in the fact that waste heat remains inside the living environment, unlike venting dryers do. Condensing dryers are typically more expensive to buy that venting dryers are due to added components, but they tend to be the favored method for automated drying in the EU.

1.4 Dryer Technology and Efficiency Literature

If one explores the different technologies that are either in use or being developed, they would find a significant number of them. Besides the three commercially available technologies of venting dryers, heat pump dryers, and condensing dryers, other methods include the obvious clothesline drying, super heated steam/mechanical steam compression (SMS/MSC) drying, microwave assisted drying, as well as waste heat recovery drying. In the United States, venting dryer manufacturers are not required to display an "Energy Guide" label telling consumers how much energy the venting dryer uses. According to the American Council for an Energy Efficient Economy, dryers are not required to display this label due to little to no variance in the power consumption of each dryer. Because of this, it was very hard to get average power consumption data for this type of dryer. Heat Pump Dryers have been on the market now for a while, and the efficiencies reported vary a bit with the better ones approaching 0.3 kWh/kg IEC efficiencies.

1.4.1 Solar

Solar ovens have been used to take advantage of the sun's free radiative thermal energy for drying clothes. Abdullah *et al.* used a forced ventilated solar chamber to dry clothes and reported drying times of around three hours for 2 kg of laundry. Energy consumption for the setup is nothing due to the use of solar cells for powering the ventilation fans, etc.(Abdullah, 2006).

1.4.2 Superheated Steam/Mechanical Steam Compression Dryer

A more recent concept, SMS/MSC dryers are based on the same concept as the paper dryer proposed by van Deventer (van Deventer, 1997) where superheated steam is used to boil off the liquid water content in the clothes. These dryers have 4 separate phases for the drying process including an initial warm-up to 100 ^{o}C, an air purge with steam, drying phase using superheated steam, and a final cooling phase. The drying technology is very promising in that it has a IEC efficiency on the order of 0.346 *kWh/kg* (Palandre, 2003).

1.4.3 Microwave

Microwaves have also been used to augment the dryer's electric or gas heating system. Microwaves aid the drying process because heat is generated volumetrically through the clothes. If the temperature of the clothes is greater than the surrounding air this will allow thermodiffusion to aid the transport of the water vapor out of the textile's porous structure into the drying fluid (Kowalski, 2003). M. Hamid experimented with this technology and obtained IEC efficiencies in the range of 0.458 kWh/kg (Hamid, 1991).

1.4.4 Waste Heat Recovery from A/Cs

Some drying designs have incorporated waste heat recovery from the condenser unit of air conditioners. As the waste heat from the air conditioner is transfer to the air, this heated air is used to dry clothes in a drying chamber. Their test Energy consumption in this case is negligible however, drying times of two hours for slightly less than 2 kg of laundry may be a bit long (Ameen, 2004).

1.4.5 Condenser Dryer

Condensing dryers also vary quite a bit in performance due to the numerous designs and manufacturers continuously modifying and changing the design of this dryer. Improving this technology has its bounds however due to thermodynamic limitations in the method in which the water is removed from the clothes. Because the latent heat of vaporization is not recovered, as in the case of the heat pump dryer, but is blown out through the heat exchanger, the amount of thermal energy required to do so is a function of the temperature at which the wet clothes are put into the dryer and the operation temperature at which the majority of the water in the clothes

evaporates. A simple thermodynamic analysis can be done to calculate the minimum amount of energy required to evaporate the water as follows:

$$E = m_{water}\left(h_{fg} + Cp_{water}\left(T_{operating} - T_{clothes,initial}\right)\right)$$

where m_{water} is the mass of the water in the clothes, h_{fg} is the latent heat of vaporization at the operating temperature, Cp_{water} is the average specific heat of the water at constant pressure, $T_{operating}$ is the average operating temperature of the dryer, and $T_{clothes,initial}$ is the initial temperature of the clothes when placed in the dryer. A typical dryer that operates at 70 ^{o}C drying a 6 *kg* load initially at 23 ^{o}C and 70% initial moisture concentration and assuming an average specific heat of $4.182\frac{kJ}{kg\cdot^{o}C}$ requires 10,121 *kJ* of energy, or 2.8114 *kWh*. This translates to an IEC efficiency of 0.469 *kWh/kg*, which is just below the class A IEC efficiency marker. To the author's best knowledge, there are no class A IEC efficiency designs available currently available, but there still stands room for improvement of the device.

1.5 More efficient removal of moisture than a condenser

In a condenser dryer, the moisture removal process is governed by the condenser. If the moisture in the dryer could be removed at a faster rate, at lower temperatures, or lower cooling fluid flow rates, then the power required by the dryer would be less, and therefore would improve the efficiency of the dryer. The focus of this work is to test an alternative way to remove the moisture from the dryer using devices called Surface Tension Elements.

CHAPTER 2 - Surface Tension Elements

Surface Tension Element (STE) technology is a relatively unexploited area of research and development that has been known to the scientific community for quite some time. At the heart of the technology is surface tension, an intriguing property of fluids. If properly applied, STE technology could be incorporated into existing technologies to enhance their operation. One such area is humidity control, which will be the focus of this study. First, a summary of previous work using STE technology to control moisture is given, followed by a short history and general description of the technology. Next, the governing physics responsible for surface tension, how surface tension can be harnessed using STE technology, and examples of STE technology are presented. Finally, a discussion of how we intend to use STEs to attempt to improve the operation of residential dryers is presented.

2.1 Using Surface Tension Elements to Remove Moisture

Only recently has the use of surface tension been harnessed to control moisture. The primary application of this technology has been used in space plant irrigation and nutrient delivery systems where precise moisture content and nutrient concentration of the soil is crucial to the optimal growth of plants. Too much moisture can result is the release of excess water from the soil and floating around in the spacecraft interior environment. By using STEs, or membrane-based irrigation systems, the release of liquid moisture into the spacecraft interior environment, pathogen growth, plant flooding, and oxygen depletion in the root zone can all be prevented or limited (Scovazzo, 2001). As a result, there has been significant work in this area.

2.2 History of STE Development

Historically, STEs were called Propellant Management Devices, or PMDs, by the aeronautics and astronautics industries. Many of these industries still continue to use the PMD terminology. In this work, we consider STE and PMD terminology to be interchangeable. In a microgravity environment, the location of the rocket fuel or oxidizer inside a tank is not necessarily at the “bottom” of the tank. The vehicle’s net acceleration and spin affect the location of the fluid as well as time dependencies. For example, if the fuel tank at rest in a zero g

environment, surface tension will cause the liquid to uniformly coat all surfaces on the interior of the tank and form a spherical vapor bubble in the center of the tank. If the tank is subjected to a net acceleration in a given direction, the fuel will then move in the opposite direction and collect at this new "bottom" of the tank. This will cause a vapor pocket at the new "top" of the tank. If the fuel extraction point for the tank happens to be located at this point, then vapor will be drawn into the rocket engine's fuel supply lines, causing problems. The primary purpose of a PMD is therefore to prevent vapor from entering the engine until the fuel supply is as close to depletion as possible.

PMDs take advantage of surface tension in order to dominate gravitational, inertial, and forces acting on a liquid. The exact method of how this is done varies from design to design. Screens, perforated sheets, vanes, sponges, troughs, and various types of fluid permeable porous structures have been used for PMD construction (Rollins, 1985).

2.3 Theory of Operation

2.3.1 Surface Tension Background

It is known that at the interfacial region separating the gas and liquid phases of a substance, a phenomenon commonly called as surface tension arises. Surface tension can be attributed to the existence of intermolecular forces acting on the individual molecules of the liquid phase. Basic kinetic theory tells us that as two molecules are brought closer together, intermolecular forces begin to exert themselves in the form of electrostatic, induction, and dispersion forces. In water, electrostatic forces, caused by the imbalance of the electron distribution between the hydrogen and oxygen atoms, causes the molecules to have a finite dipole moment and the ability to attract or repel one another based upon their orientation to each other. These forces cause the individual water molecules to attract one another until the molecules are brought into such close proximity that the electron clouds of each molecule's atoms begin to interfere with those of the other one at which point the molecules begin to repel one another. This tendency can be represented mathematically by the Lennard-Jones 6-12 potential (Faghri and Zhang, 2006):

$$\phi(r) = 4\varepsilon\left[\left(\frac{r_o}{r}\right)^{12} - \left(\frac{r_o}{r}\right)^{6}\right] \qquad \textbf{Equation 2}$$

Where ε is the energy of interaction, r_o is the equilibrium distance, and r is the distance between the molecules. Figure 2.1 shows a plot of the potential as a function of distance between two spherical, nonpolar molecules.

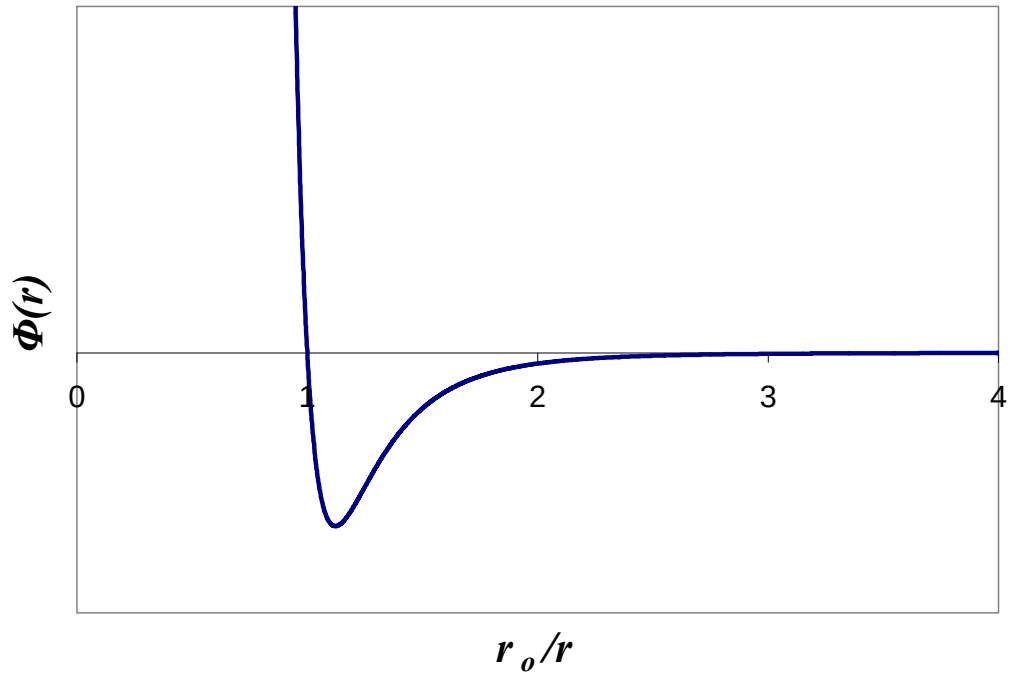

Figure 2.1 Lennard-Jones Potential Function

While this relationship is limited to the case of nonpolar molecules, which excludes water due to its finite dipole moment, the Lennard-Jones potential can be augmented to incorporate a term for the molecule's polarity. This new potential function is called the Stockmayer Potential. In the liquid phase, these intermolecular forces keep the individual molecules in close proximity to each other while the thermal energy of each individual molecule prevents it from "locking" itself into an organized lattice structure characteristic of the solid phase. In the gaseous phase, the molecules have such a large thermal energy, that the molecules are very far from one another, causing the intermolecular attractions between gaseous molecules to be drastically smaller than those of the liquid phase.

When a liquid phase is bounded by a gaseous phase, an interesting phenomenon occurs from the imbalance in intermolecular forces. Figure 2.2 shows how a water molecule surrounded by other water molecules in the liquid phase is pulled evenly in all directions from intermolecular forces resulting in a zero net force acting on the molecule whereas a molecule located at the interface is not.

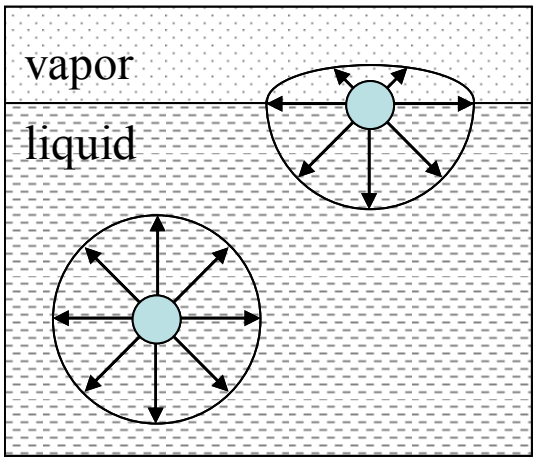

Figure 2.2 Intermolecular Forces at a Gas/Liquid Interface

Adapted from: Faghri and Zhang, 2006

The molecule at the interface has a net force in the direction of the bulk fluid, which causes the motion of the fluid molecules until the minimum number of molecules at the interface and maximum number in the interior is achieved. This typically manifests itself as a curved surface since curved surfaces minimize surface area while maximizing internal area.

In 1805, Thomas Young presented the results of his analysis of a drop of fluid on a solid surface. He explained that the surface tension at work at the liquid-vapor interface can be related to the surface tensions between the solid and vapor and between the solid and liquid. Young's model construction is shown in Figure 2.3 and in Equation 4.

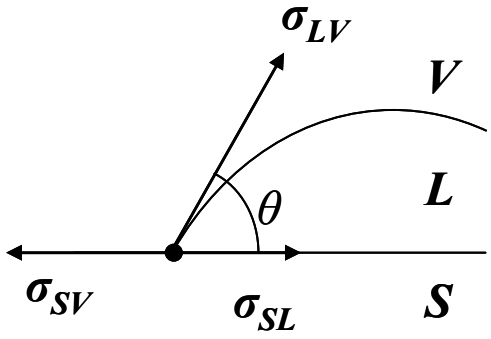

Figure 2.3 Young's Model Construction

$$\sigma_{LV}\cos\theta = \sigma_{SV} - \sigma_{SL} \qquad \textbf{Equation 3}$$

From this, we can see that the surface tension acting at the contact line bounding all three phases must balance each other in the components parallel to the solid surface.

In 1806, Pierre-Simon Laplace analyzed this phenomenon at work at a spherical interface of a liquid and vapor from a mechanical equilibrium standpoint. If a curved interface between a liquid and vapor is present, there will be a pressure discontinuity across the interface. Laplace looked at the forces required to retain the curved surface to balance the pressure discontinuity much like the hoop stress in a cylindrical pressure vessel balances the pressure discontinuity through the chamber wall. Figure 2.4 shows a graphical construction of an arbitrary liquid-vapor interface where the liquid is contained on the concave side of the curved surface.

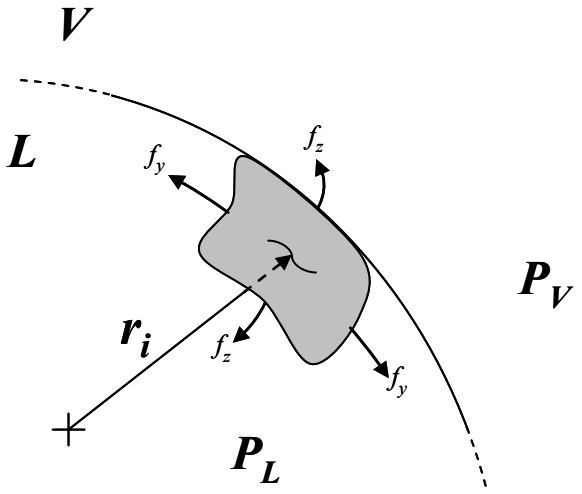

Figure 2.4 Laplace's Model Construction

The interface is spherical according to the drawing, but for completeness, we will consider a curved surface composed of two separate radii of curvature, r_1 and r_2. A balance of pressure forces and tension forces within the liquid yields Laplace's equation, shown below.

$$P_L - P_V = \sigma_{LV}\left(\frac{1}{r_1} + \frac{1}{r_2}\right) \qquad \textbf{Equation 4}$$

Where σ_{LV} is the surface tension of the fluid. Notice that when the radii are positive, the liquid pressure is greater than the vapor pressure. In the case of the meniscus having negative radius (convex surface towards the fluid), the vapor pressure is greater than the liquid pressure. If the radii are equal to each other, then the surface is spherical.

J. W. Gibbs brought a more rigorous element to Laplace's and Young's purely mechanical equilibrium derivations by proving that the equations are necessary boundary conditions for thermodynamic equilibrium of the liquid, vapor, and solid interfaces. In the derivation, Gibbs derives a method of keeping track of the free energy of the global system, and then solves the equations such that the total free energy of the system is minimized (Roura, 2005).

2.3.2 Utilizing Surface Tension

Surface tension can be utilized to only allow liquid flow through a porous structure while arresting gaseous flow. This concept has been used for years in what are called as propellant management devices, PMDs, as described earlier. To begin explanation, it is probably best to start with the circular capillary model, where the STE porous structure consists of circular passageways through the bulk material.

Figure 2.5 shows a cross-sectional view of the porous structure with a spherical interface between the gas and liquid phases.

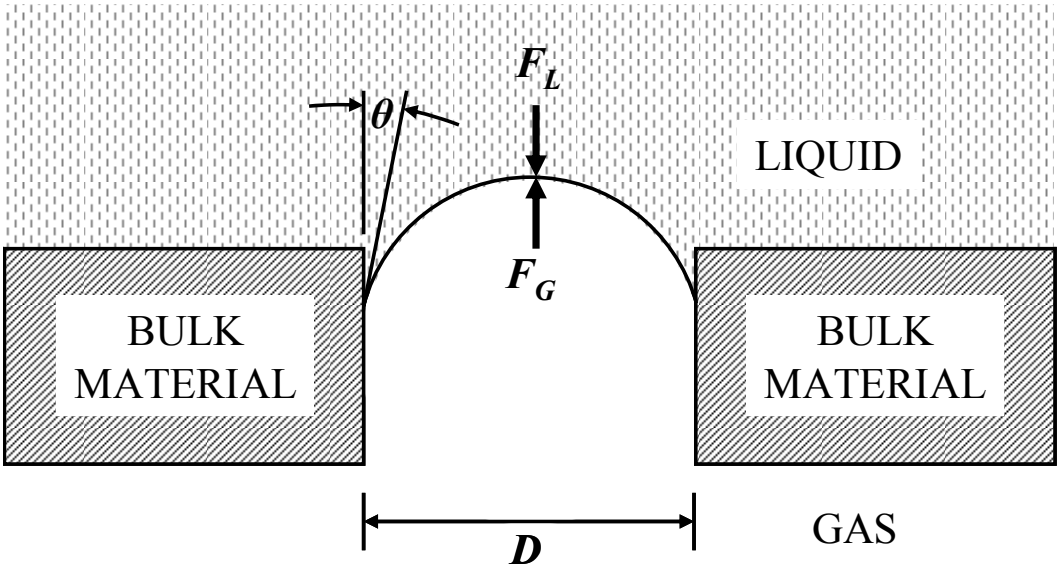

Figure 2.5 Circular Capillary Model Cross Sectional View

A force balance in the direction along the pore's axis can help us to quantify the effects of surface tension. Surface tension acts along the circumference of the solid/liquid/vapor interface where the liquid intersects the solid surface at some advancing contact angle, θ. This force can be summed along the contact length, L, as follows:

$$F_L = \sigma_{LV} \cos(\theta) L \qquad \textbf{Equation 5}$$

Since the total contact length L is equal to the circumference,

$$F_L = \sigma_{LV} \cos(\theta) \pi D \qquad \textbf{Equation 6}$$

The total force exerted by the gas in the opposite direction may be found by projecting the area of the spherical interface onto a plane, and then multiplying by the pressure difference that the gas exceeds the liquid.

$$F_G = \Delta P A = \Delta P \pi \frac{D^2}{4} \qquad \textbf{Equation 7}$$

Since the forces must be equal to one another but opposite in direction, they may be equated to each other to obtain equilibrium:

$$F_G = F_L \qquad \textbf{Equation 8}$$

Which when Equation 6 and 7 are substituted becomes

$$\Delta P \pi \frac{D^2}{4} = \sigma_{LV} \cos(\theta) \pi D \qquad \textbf{Equation 9}$$

Upon rearrangement and solving for the pore diameter, D, becomes

$$D = \frac{4\sigma_{LV}\cos(\theta)}{\Delta P} \qquad \textbf{Equation 10}$$

Equation 10 and its various forms is the basis for quantifying the ability of an STE to arrest gaseous flow while allowing fluid flow. In most applications for rocket propellants or in our case, water, the contact angle is assumed to be zero or very small. With this assumption, *cos(θ)* tends to unity, and the relation reduces to Laplace's equation for a spherical interface when the radii are equal to one another. It must be noted however, that this model is valid only for circular pores.

If the pore happens to be a rectangular slot, as shown in Figure 2.6, a triangle, or some other geometry, Laplace's equation may be used as follows:

$$\Delta P = \sigma_{LV}\left(\frac{1}{r_1}+\frac{1}{r_2}\right) = \sigma_{LV}\left(\frac{2}{D_1}+\frac{2}{D_2}\right) \qquad \textbf{Equation 11}$$

If D_1 is much larger than D_2, then its total contribution to the pressure difference is negligible and the equation reduces to

$$\Delta P = \frac{2\sigma_{LV}}{D_2} \qquad \textbf{Equation 12}$$

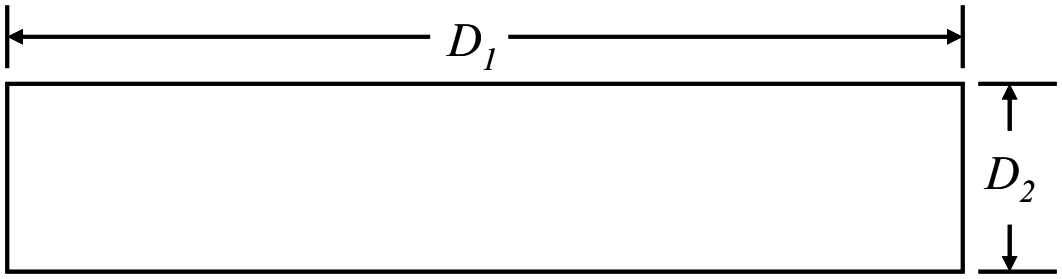

Figure 2.6 Rectangular Pore Slot

More difficult pore shape structures can be analyzed with the help of the SAE ARP901 document (SAE, 2001).

2.3.3 STE Micron Rating

The performance of a STE is commonly quantified by the STE's largest pore diameter, which is found by a procedure called the bubble-point test. This diameter is commonly called the *micron rating* of the STE and is usually expressed in micrometers, *μm*, or microns. The standard procedure for determining the micron rating of an STE is the *bubble-point test method*, which is discussed later in Chapter 4.

2.3.4 STE Application Examples

Consider the tank shown in Figure 2.7 where a porous wall separates the left chamber from the right chamber. The right chamber has an outlet whereby liquid may be removed from that chamber via pumping action.

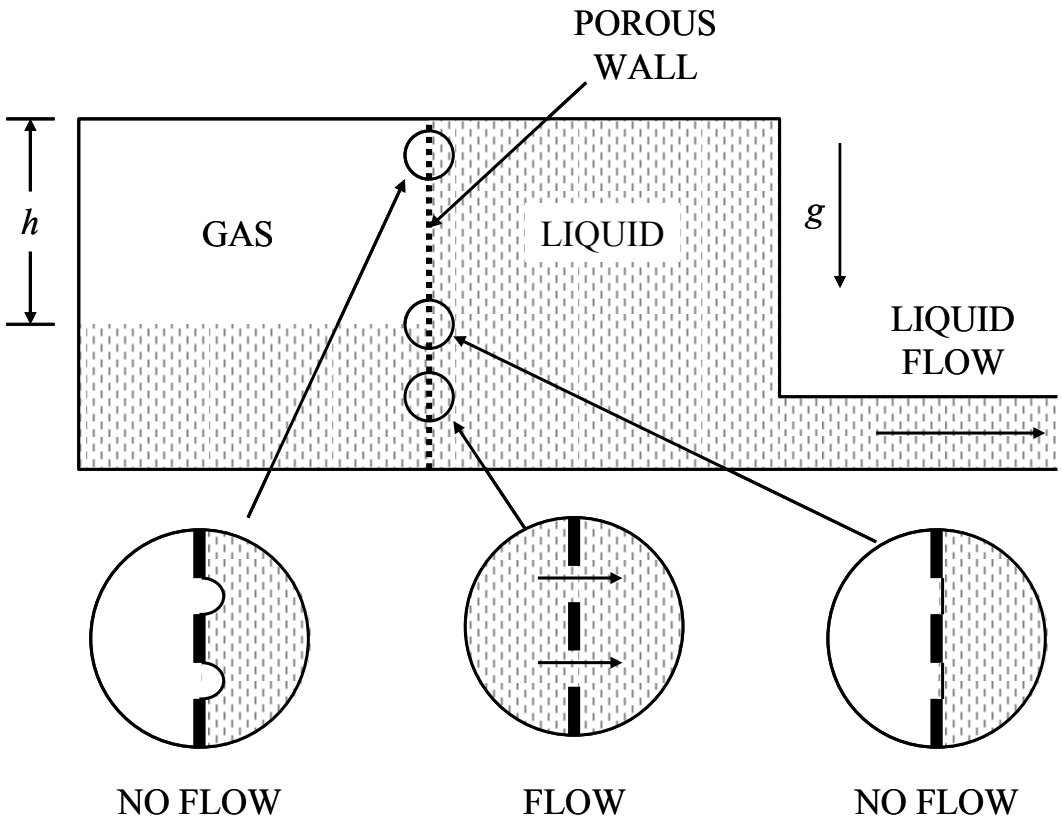

Figure 2.7 Porous Wall Liquid Flow / Gas Arrest

At the bottom of the porous wall, where liquid exists on both sides of the wall, liquid is free to move through the porous structure. A small pressure drop across the wall will exist, but we will assume that the flow is small enough for this pressure drop to be negligible.

At the location where the liquid phase ends and the gas phase begins at the porous wall, the pressure on either side of the wall is exactly equal. If the pressure on the right side of the wall were to ever exceed the pressure on the left side, liquid would flow through the structure from right to left.

At the top of the porous wall, the largest pressure difference across the wall exists. If hydrodynamic pressure in the right chamber is set to be equal to zero at the liquid level in the left chamber, pressure will decreases with increase in height in the right chamber. Since gas pressure in the left chamber remains relatively constant, this results in a pressure differential equal to

$$\Delta P = \rho_{liquid} g h \qquad \textbf{Equation 13}$$

Which can be substituted to Equation 10 and solved for *h* assuming the circular pore model and the porous structure can be completely wetted (zero contact angle):

$$h = \frac{4\sigma_{LV}}{\rho_{liquid} g D} \qquad \textbf{Equation 14}$$

Equation 14 allows us to quantify the theoretical maximum difference in liquid height between the left and right chambers. If this height is exceeded, the capillary forces restraining the gas from entering the right chamber will be overcome, and gas will begin to enter the right chamber at the top. As an example, we will consider that the fluid is water having a surface tension of 0.0742 *N/m* (74.2 *dynes/*cm) and density of 998.2 kg/m^3 at 20 ^oC and a pore diameter of 20 microns.

$$h = \frac{4 \cdot \left(0.0742 \frac{N}{m}\right) \cdot \left(\frac{kg \cdot m}{N \cdot s^2}\right)}{\left(998.2 \frac{kg}{m^3}\right) \cdot \left(9.807 \frac{m}{s^2}\right) \cdot \left(20 \cdot 10^{-6} m\right)} = 1.516 m$$

Therefore, the maximum difference in height possible through a porous wall structure containing 20-micron diameter holes at 20 ^oC is 1.516 *m*, which is quite substantial.

If we were to consider a two dimensional enclosure filled with liquid consisting of three solid walls and the fourth consisting of a porous wall. If the structure is oriented as shown in Figure 2.8, the same phenomenon is observed where the porous structure will allow liquid to be trapped in the enclosure.

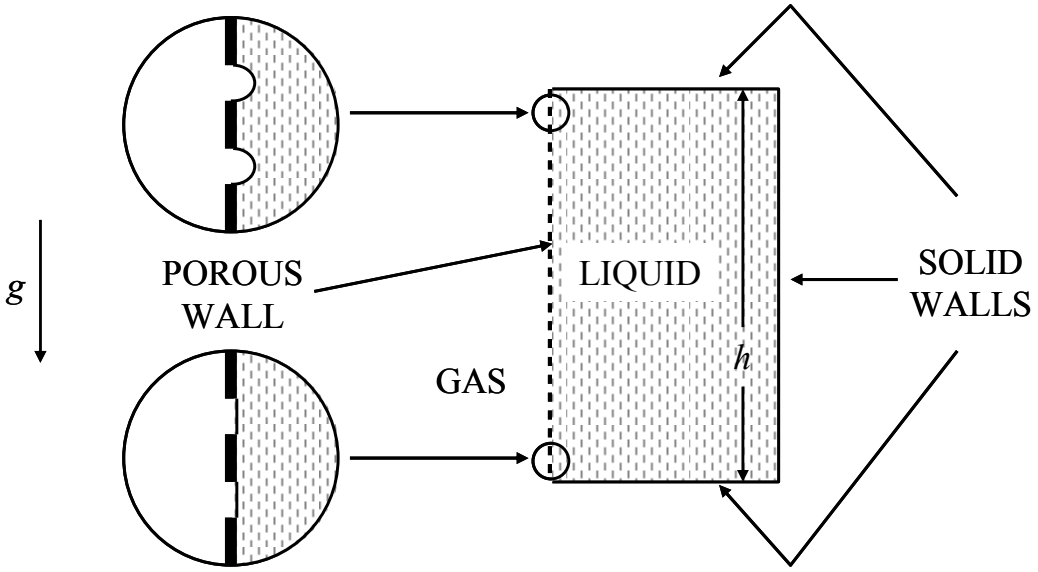

Figure 2.8 Two-Dimensional Porous Wall Liquid Trap

At the bottom of the wall, the gas pressure is equal to the liquid pressure. At the top of the wall, the same equilibrium condition of the previous example holds where a hydrostatic pressure head can be supported by the capillary forces of the porous structure.

These simple examples show how STEs (PMDs) could be used in space applications to control the location of the propellant and/or prevent air bubbles from entering the fuel lines to the engine until the tank is nearly empty. They also show how surface tension can be used to dominate gravitational and inertial forces for other applications.

2.3.5 Using STEs to Improve Drying

As was mentioned before, the focus of this work is to attempt to use STE technology to remove the moisture in the drying fluid of a modern condenser dryer. The performance of the modern condenser suffers from the method in which condensate forms on the cooling fins of the unit. There are two known methods that condensate forms – *filmwise* and *dropwise*.

In filmwise condensation, the condensation surface is wettable and allows the liquid phase to spread out on its surface. In the initial stages of condensation, the cool surface promotes vapor molecules to condense on the surface and give up their latent heat energy to the cool surface. This latent heat is then conducted through the condenser's walls and to the cooling fluid via convection. As condensation continues, the vapor molecules link up and spread out across the surface forming a thin film covering the surface. There are several ways of removing this thin film from the surface. If there is interfacial shear on the liquid surface (when the vapor

is blown over the fins) or if the fins are oriented such that gravity can act on the film, then the liquid film will flow, forming hydrodynamic and thermal boundary layers. This thin film introduces a significant added thermal resistance to heat transfer process and thus to the coupled mass transfer process.

As vapor molecules condense in dropwise condensation, the liquid tends to group together forming beads of liquid on the surface. These beads can be blown off or fall of if gravity is oriented correctly. Because much more of the surface area is directly exposed to the vapor phase, the thermal resistance present in filmwise condensation is greatly reduced, but not completely eliminated due to the presence of the liquid droplets still having a thermal resistance.

In lieu of a condenser, a STE could be implemented such that a suspended sheet of liquid water promotes the condensation of the vapor. This can be accomplished if the STE can overcome gravitational forces with surface tension forces. There are two areas that condensers could be improved in by using a STE in this manner. The first improvement is to remove the parasitic heat transfer effects of the liquid film and the second is to remove the heat transfer losses through the condenser's walls separating the two fluids. If we remember that a STE will allow liquid phase flow and arrest vapor flow, these parasitic losses can easily be removed because the liquid condensate that forms on the STE will flow right through the STE wall without allowing any vapor to flow through. This results in an effective film thickness of zero. If the bulk liquid on the interior of the STE is constantly pumped through the STE and changed, any condensate that enters the STE will automatically be entrained in the flow. Also, if the STE material consists of a wire mesh (which is to be differentiated from a thick porous ceramic), which is typically about 0.001" thick, then liquid flow velocity through and in the near vicinity of the STE material will not be greatly affected. The overall outcome of this STE implementation results in a very small temperature gradient present in the liquid phase, thus greatly reducing the parasitic heat transfer and mass transfer losses through a liquid film and wall present in a traditional condensing unit.

By using a STE in lieu of a condenser in a condensing dryer, the improvements stated above should promote more rapid condensation within the dryer. This will in turn allow the dryer to run at significantly lower humidity ratios than would be typical of a condenser dryer. Because evaporation of water from a cloth load is mostly a function of water vapor concentration difference between the cloth surface and drying fluid, running at this lower humidity ratio should

increase the rate of evaporation of water from the textile load. This should allow the drying time to shorten, thus decreasing energy losses through heat transfer.

CHAPTER 3 - Problem Statement

The object of this study is to determine whether or not the efficiency of a European condensing dryer can be improved by using Surface Tension Elements. To this end, a European condensing dryer was tested utilizing a standard dryer condenser and a STE. By comparing the energy consumption of each type of test with the other, the relative performance of the STE was evaluated. A total of ten tests were run composed of five tests for the condenser and five tests for the STE. These results are discussed in Chapter 6.

3.1 Description of Setup

A Whirlpool AWZ9993 condenser dryer was used for the tests. This dryer was modified as described in the next chapter to allow for temperature, humidity, pressure, and power consumption measurements. Temperatures were measured at various key locations such as at inside the drum, after the lint filter, before and after the condenser or STE, and finally before and after the heater. Humidity measurements were recorded before and after the condenser or STE. Pressure measurements were made in the drum and in the region of the condenser or STE. These measurements allowed for the monitoring of the drying process and for providing data by which a comparison of an analytical model could be done. Other modifications were necessary to allow it to run here in North America utilizing a different power cycle frequency than is present in the unit's intended geographical implementation. This was done by rotating the drum and blower fans with a speed-controlled motor.

The STE was designed such that it could fit into the docking port of the dryer's existing condenser. This way the moisture removal device, whether it be the condenser or STE, could be simply interchanged. As was mentioned at the end of Chapter 2, the liquid water on the interior of the STE had to be constantly pumped through the device in order to ensure that the device's surface temperature was of negligible difference than that of the bulk of the fluid flow. The STE was plumbed such that one side was attached to the suction side of a positive displacement pump and the other side was plumbed to a reservoir of liquid water open to the atmosphere. This plumbing setup ensured that the internal STE pressure was at all times less than atmospheric pressure – which allows the STE to effectively "hold" the sheet of liquid water in the dryer's

drying fluid. On the positive side of the pump, the water was forced through a filter and a heat exchanger before it was dumped back into the reservoir. The heat exchanger helps to prevent the STE water temperature from drastically increasing and prohibiting the moisture removal process. Instrumentation was attached to this flow loop to keep track of the temperature of the water in the reservoir and exiting the heat exchanger. The power consumption of the pump was also monitored.

3.2 Test Load

A cloth test load composed what are called as "energy cloths" were used. These cloths are described in detail in the Chapter 4. The load size was determined by allowing the cloths to sit in room air for several days to allow them to reach equilibrium with their surroundings. The cloths were then added together until a cumulative weight as close as possible to the dryer's capacity of 6 *kg* was reached (meaning that the load weight as close as possible to 6 *kg*). To achieve an initial moisture concentration for the tests, the load was run through the "rinse" cycle of a washer. A digital scale measured the load weight before and after the tests in an effort to quantify the amount of water gained through the rinse cycle and removed through the drying process.

3.3 Test Procedures

There were two separate test procedures used– one for the condenser "baseline" tests and one for the STE tests. Each test was run no more than several hours after a previous test to ensure that the dryer's temperature had reached equilibrium with its surroundings.

3.3.1 Condenser Test Procedure

1. Test Load is placed in washing machine. Washing machine is set to *Rinse/Spin* cycle, *Cold/Cold* temperature selection, and *High* spin speed. The washer then rinses the test load to achieve the initial moisture content.
2. While waiting for the test load, the lint filter is removed and cleaned by a vacuum cleaner to remove any lint that might alter the test's results. An empty 3 liter glass beaker is also placed under the exit of the dryer's condensate tube. Ensure that the condenser is docked in its docking port in the dryer.
3. When the washer finishes, remove and weigh the load.

4. Place the clothes in the dryer and immediately close the door. Set the drying programme to *Cotton Cupboard Dry* + setting.
5. Initiate Data Acquisition
6. Turn on the dryer motor with the speed controller
7. Turn on the dryer
8. Measure the speed of the dryer motor to ensure that the dryer is rotating properly.
9. Wait until the dryer's time remaining clock indicates that the load is dry.
10. Turn off the dryer
11. Turn off the dryer motor with the speed controller
12. Terminate Data Acquisition
13. Remove and weigh the test load.
14. Weigh the beaker used to catch the condensate and calculate the weight of the water collected.

3.3.2 STE Test Procedure

The STE test must be superseded by a period of allowing the STE element to soak completely submerged in water for at least several hours. This allows the water to seep into all parts of the device. In these experiments, the STE was simply submerged in the flow loop reservoir.

1. Test Load is placed in washing machine. Washing machine is set to *Rinse/Spin* cycle, *Cold/Cold* temperature selection, and *High* spin speed. The washer then rinses the test load to achieve the initial moisture content.
2. While waiting for the test load:
    - Remove and clean the lint filter by a vacuum cleaner to remove any lint that might alter the test's results
    - Place an empty 3 liter glass beaker under the exit of the dryer's condensate tube
    - Fill the flow loop reservoir with fresh tap water (typically around 18 ^{o}C).
    - Make sure that all trapped air pockets on the interior of the STE are removed
    - Initiate the flow loop pump to make sure flow loop is operating properly.

- Insert STE in docking port
- Set the flow loop reservoir water height to the correct level ($2\ ^{5}/_{8}$ inches from the top of the reservoir).

3. When the washer finishes, remove and weigh the load.
4. Place the clothes in the dryer and immediately close the door. Set the drying programme to *Cotton Cupboard Dry* + setting.
5. Turn on flow loop heat exchanger's fan
6. Initiate Data Acquisition
7. Turn on the dryer motor with the speed controller
8. Turn on the dryer
9. Measure the speed of the dryer motor to ensure that the dryer is rotating properly.
10. Wait until the dryer's time remaining clock indicates that the load is dry.
11. Turn off the dryer
12. Turn off the dryer motor with the speed controller
13. Terminate Data Acquisition
14. Remove and weigh the test load.
15. Measure the flow loop reservoir water height
16. Weigh the beaker used to catch the condensate and calculate the weight of the water collected.
17. Remove the STE from the dryer and place it back in the flow loop reservoir
18. Turn off the flow loop pump
19. Turn off the flow loop heat exchanger's fan

CHAPTER 4 - Experimental Setup

4.1 Condenser Dryer

The condenser dryer used in these experiments is a Whirlpool AWZ9993 Condenser Dryer manufactured in France. Below in Table 4.1, selected specifications for the dryer are displayed, and a picture of the dryer is shown in Figure 4.1.

Table 4.1 Condenser Dryer Parameters

Parameter	**Description**
Rated Capacity	6 kg
Energy Label	Class C
Average Power Consumption per 6kg Load	4.2 kWh
Drum Volume	112 Liters
AC Voltage	220-240 V
AC Frequency	50 Hz
Drum Rotation Speed	54 rpm

Figure 4.1 Whirlpool AWZ 9993 Condenser Dryer

This dryer presented itself to be a challenge to experiment with here in North America where supply voltage magnitude could be supplied but the frequency is not. Upon careful inspection of the dryer's systems, it was determined that the dryer could function on standard 210V 60Hz supply voltage. The electrical system and heating elements would have no significant changes in their operation. The motor however would experience an increase in speed on the order of 20%. At first, this was not seen as a drawback until several calculations revealed that it could be problematic. Generally, tumble dryers are designed to rotate at a speed just slow enough so that centrifugal forces from drum rotation do not overcome gravitational forces(Watts,1991). If this is the case, then the gravity will cause the clothes to "tumble" down

when they reach the top of the drum. In our case, a simple check of rotation speed revealed the problem. The centripetal acceleration from rotation can be found by:

$$a_c = \omega^2 r$$

Where ω is the angular velocity and r is the radius of the drum. The drum diameter is approximately 0.572 *m* which gives *r* to be approximately 0.286 *m*. If the drum rotates at 20% faster rate than the manufacturer states, it will rotate at 64.8 *rpm*. Using a stroboscope tachometer, the drum speed was measured as 63.85 *rpm* with a 6 *kg* dry load in the drum, which validates the previous speed increase calculation. The angular velocity can be found accordingly:

$$\omega = \frac{63.85\,\text{rotation}}{\text{min}} \cdot \frac{\text{min}}{60s} \cdot \frac{2\pi rad}{\text{rotation}} = 6.686\frac{rad}{s}$$

The centripetal acceleration is then found to be:

$$a_c = \omega^2 r = \left(6.686\frac{rad}{s}\right)^2 \cdot 0.286m = 12.9\frac{m}{s^2}$$

It is plain to see that the centripetal acceleration is greater than gravitational acceleration of 9.81 m/s^2, therefore, the tumbling action of the clothes will be impacted by the increased supply voltage frequency.

4.1.1 Dryer Rotation Speed Modifications

Upon discovery of the effects of the increased drum rotation speed, a method that could correct the rotation speed was sought. The solution to this problem was to alter the drive system by externally driving it with another motor capable of being speed controlled. A 3φ motor controlled by a variable frequency drive (VFD) was chosen to drive the system. The 3φ motor's maximum speed is *1740 rpm*, thus a belt and pulley system was also used to drive the dryer motor at the required *2700 rpm*. The main drive motor was disconnected from the dryer's control electronics. Next, a shaft with a $1\ ^{11}/_{16}$ inch outer diameter pulley was coupled to the motor's shaft and supported with a mounted bearing. A 4L-310 V-belt was used to drive the shaft. The 3φ motor's pulley used a $3\ ^{13}/_{16}$ inch outer diameter pulley. An idler pulley was also used as a belt tensioning device. Figure 4.2 shows a picture of the shaft that couples to the dryer's motor shaft and Figure 4.3 shows a picture of the entire setup being calibrated for the correct rotation speed.

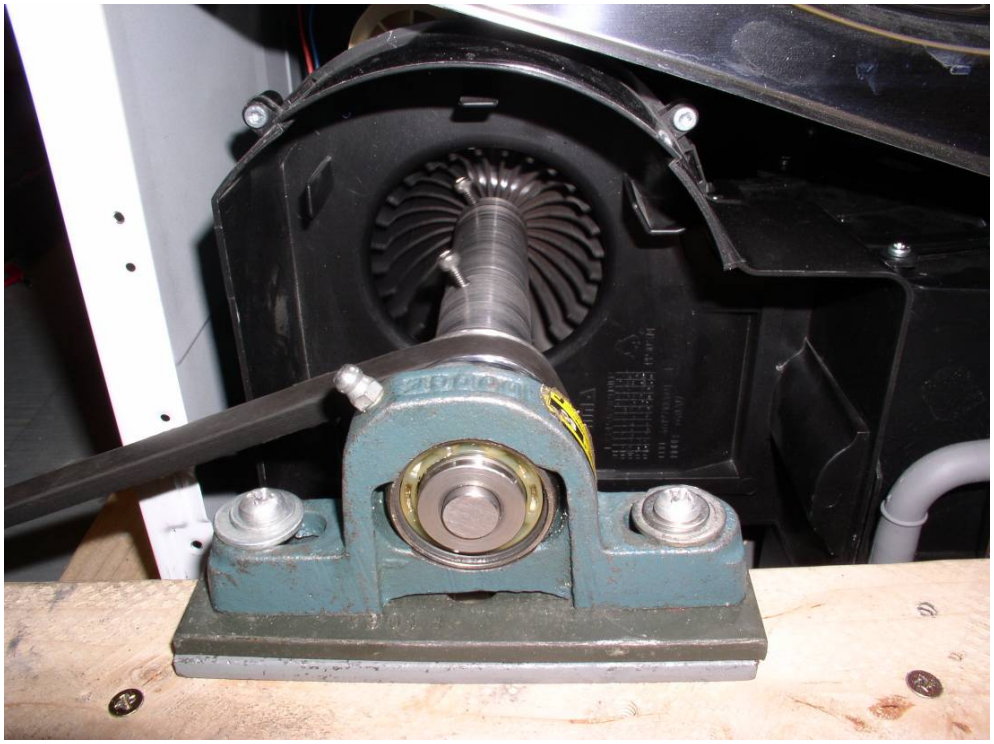

Figure 4.2 Drum Motor Coupling Shaft and Pulley System

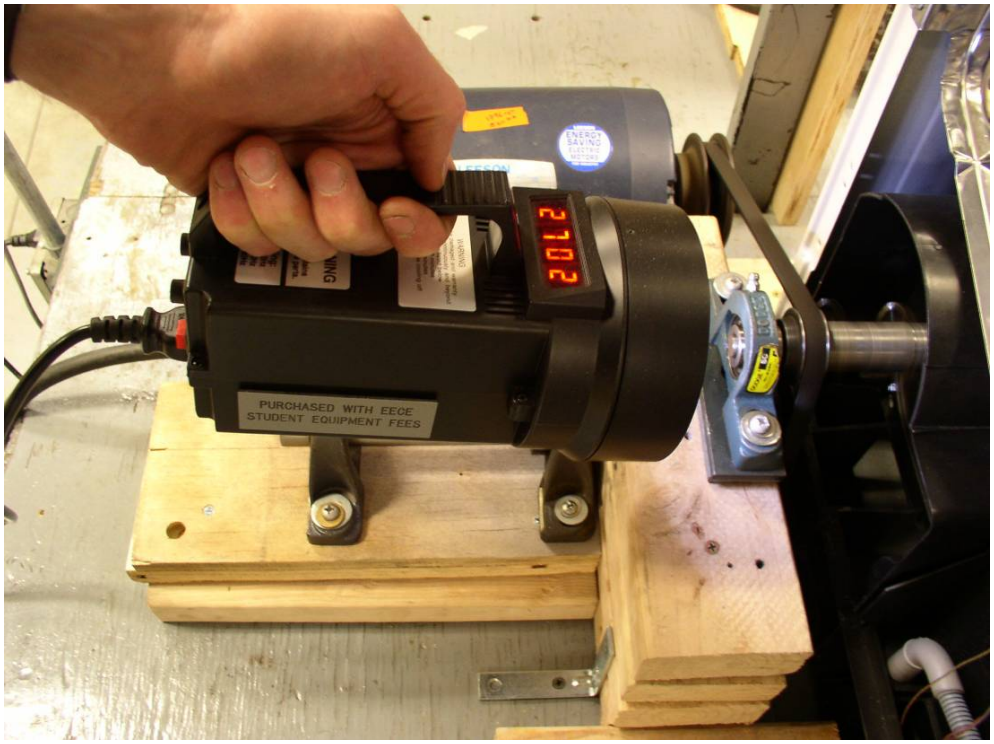

Figure 4.3 Dryer Speed Correction System Calibration

The rotational speed of the dryer motor was set with a Digital StroboTach manufactured by Extech Instruments. The accuracy of the StroboTach is stated by the manufacturer to be

±0.05% reading +1 least significant digit. Thus, the speed of the dryer motor was 2700 ± 2.35 rpm. The VFD drive setting producing the correct rotational speed was 45 Hz. Using this setup and controlling the drum motor's rotational speed to 2700 rpm, the drum speed can be calculated. The motor to drum speed ratio was previously measured as:

$$\chi = \frac{rpm_{motor}}{rpm_{drum}} = \frac{3285rpm}{63.85rpm} = 51.45$$

Therefore, the speed of the drum using the new drive system is:

$$rpm_{drum} = \frac{rpm_{motor}}{\chi} = \frac{2700rpm}{51.45} = 52.48rpm$$

which is acceptable for our purposes.

4.1.2 Condensation System

The dryer uses an air/air crossflow heat exchanger as a condenser. Figure 4.4 shows a picture of the heat exchanger. The unit is very compact and "plugs in" to a cavity hidden behind a vent door on the bottom left of the dryer. If one views the heat exchanger from the front (the side that has the locking handle), the drying fluid passes through the hollow plates from right to left and moisture condenses on these plates. From the picture, it is easy to see that several lint fragments have escaped being captured by the lint filter and have dried on the condensing surface. The unit has a handle such that it can lock the heat exchanger into the cavity as well as compress the heat exchanger's sealing gasket surfaces to prevent the drying fluid from leaking into the room. Room air is blow through the hollow plates entering at the rear section and exiting out the front (it would blow on your face if you were looking at it from the front).

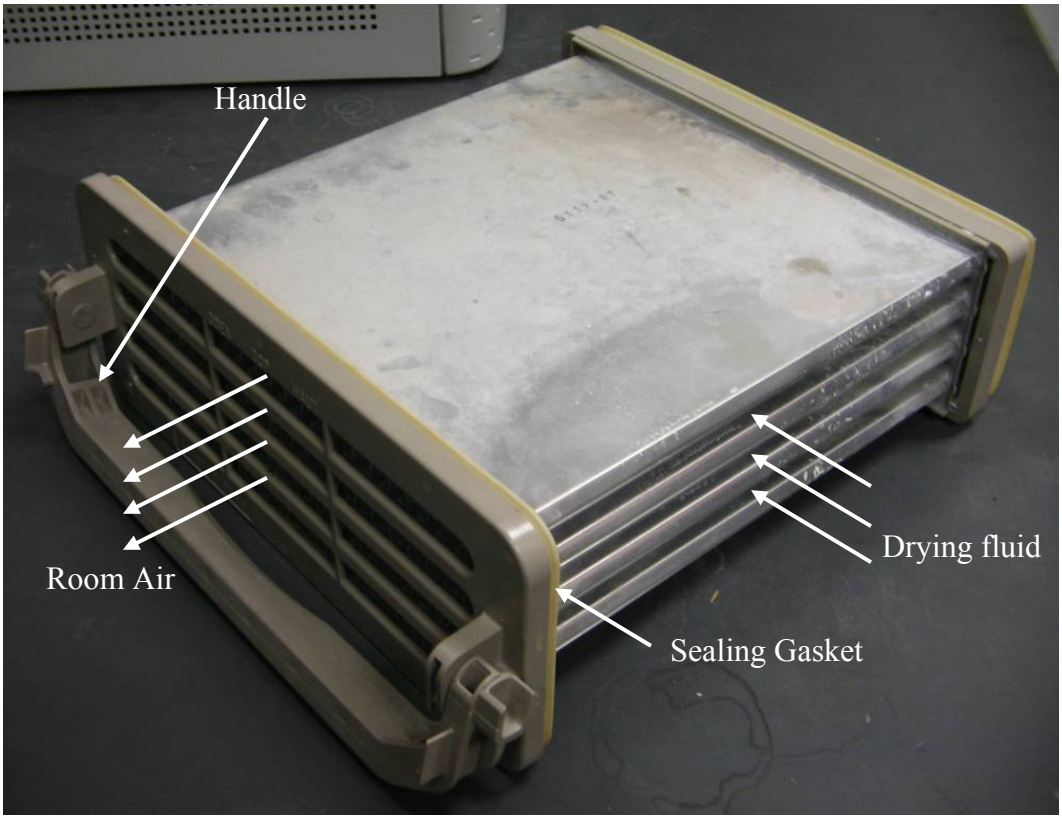

Figure 4.4 Air/Air Crossflow Heat Exchanger

As moisture condenses on the plate surfaces, it runs off and collects at the lowest point in the dryer's heat exchanger cavity. At this point, a hole leading to a small water tank allows excess liquid to leave the cavity and collect in the small tank. A level switch on the small tank detects when the liquid level exceeds a certain height, and then activates a small pump housed in the tank. The small pump's outlet is connected to tubing which can be connected either to a larger tank located at the top of the dryer or to a household drain. When the dryer was first tested, it was observed that the pump did not function correctly and would not pump liquid out of the small tank. This system was therefore bypassed by drilling and tapping a new pipe fitting into the bottom of the small tank. The fitting had a barbed tube fitting on the output side, so a flexible u-tube was constructed and attached to the fitting to direct the condensate to a drain. A u-tube configuration was chosen so that the condensate would form a vapor trap and prevent the drying fluid from escaping through the condensate hole, tank, and u-tube to the environment. This allows the level in the tank to never activate the level switch, thus eliminating the need for the small pump in the tank.

4.2 STE

A surface tension element for use in these experiments was designed built and tested. The theory of operation of surface tension elements is described to provide general theoretical information for the reader.

4.2.1 STE Design Considerations

Much iteration was required to arrive at a viable design for the STE. The primary design consideration for the STE was to maximize the surface are exposed to the humid air stream, thus maximizing the mass transfer rate of water vapor from the humid air to the surface of the STE. The secondary design consideration was minimizing the diameter of the holes in the STE porous material, which allows for larger differences in pressure between the surrounding air and the internal liquid. Because it was important to maintain the relatively low temperature of the liquid water at the STE gas/liquid interface in comparison to the bulk gas flow, the design had to incorporate some method of bulk fluid flow within the STE. This facilitated the energy associated with condensation to be drawn away from the gas/liquid interface and continue to promote condensation on the STE surface. It was very important to not modify the existing dryer in any way that would prevent the dryer from operating as it was designed. Because of this constraint, it was very desirable to have the ability to insert the STE into the docking port for the condenser module of the existing dryer. This allowed for easy installation and removal of the STE so that testing either the existing dryer's condenser or the STE was possible. This also allowed for the STE to be housed in a water-friendly housing that already incorporated a drainage mechanism in the event that the STE leaked water out into the docking port. Another feature that was desired was to emulate the air flow characteristics of the condenser. This criterion was easily meet by constructing plate-like STE structures in a modular fashion that mimicked the geometry of the condenser's cooling fins.

4.2.2 General STE Design

This section describes the physical design of the element and general descriptions of how the STE was designed to operate. Engineering drawings are available for viewing in Appendix B.

As previously mentioned, the STE was constructed in such a manner that it mimicked the design of the plate condenser. The STE consists of four modular units that stacked one upon the

other. Each module has two separate sides that are porous and achieve the desired surface tension characteristics. Figure 4.5 shows an unassembled STE module and Figure 4.6 shows an actual assembled module. Each module consists of one polycarbonate base frame, two perforated aluminum support plates, two sheets of STE porous material (not shown in the model), two vegetable fiber gaskets, two aluminum pressure plates(in the engineering drawings, these are called “holding plates”), and the various fasteners. The perforated sheets fit into a recessed groove machined into each side of the STE making the polycarbonate frame flush on each side with the top of the perforated sheet. The STE is then sandwiched between this surface and the gasket, which is compressed by the aluminum pressure plate. The entire assembly is compressed with screws around the STE porous material’s perimeter in an effort to minimize leaks.

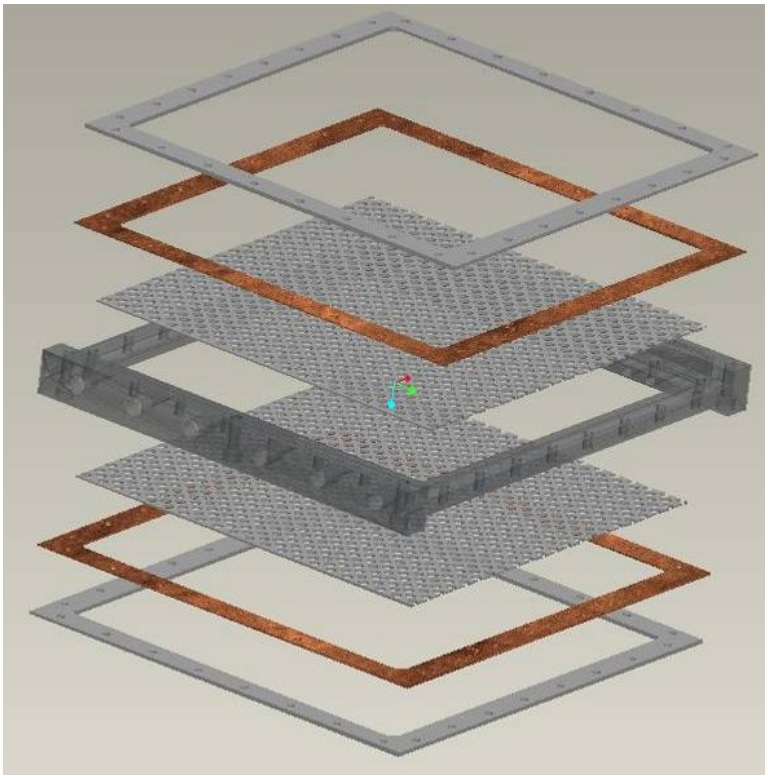

Figure 4.5 Unassembled STE Plate Module (Pro/Engineer Model)

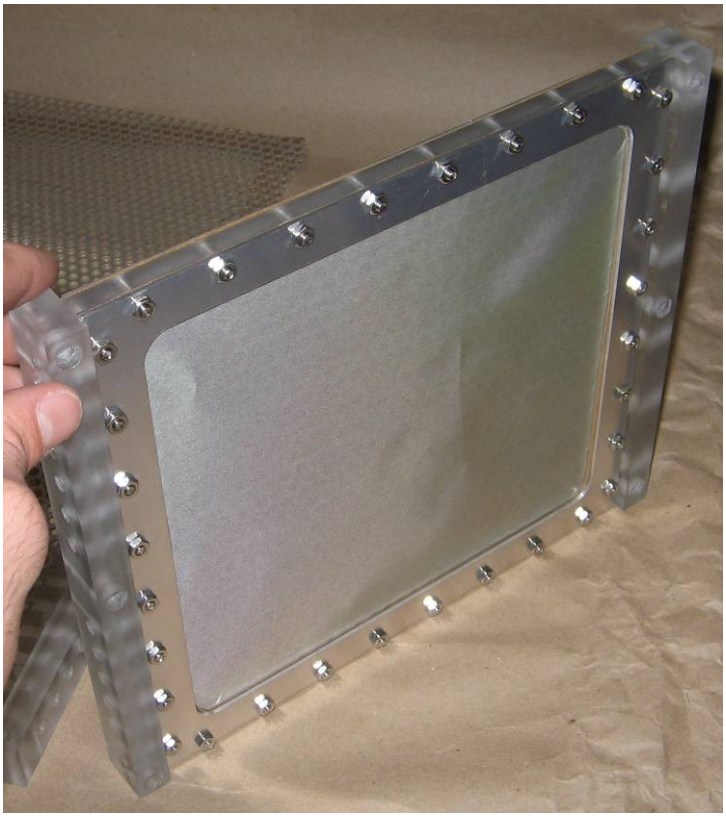

Figure 4.6 Assembled STE Plate Module

The plate modules were designed such that fluid could be flowed through the interior of the module. Figure 4.7 shows a cross-sectional view of two STEs assembled such that the flow is circuited between them and sealed with gaskets.

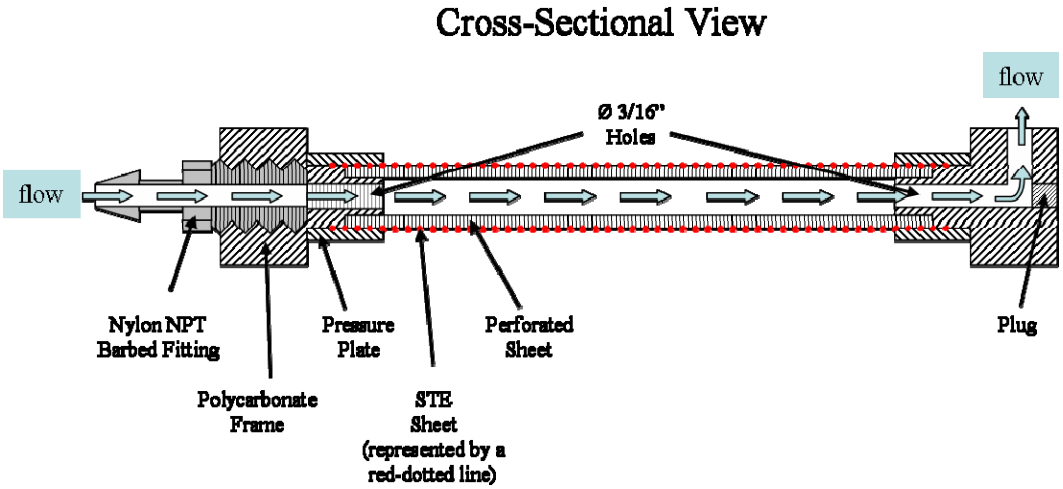

Figure 4.7 STE Module Flow Schematic

From the cross-sectional view, one can see that flow enters the module through a NPT barbed tube fitting which is screwed into the polycarbonate base frame (there are actually six

fittings along the depth of the module – only one is shown here for simplicity's sake). Six $^{3}/_{16}$ inch through holes from the fittings to the interior of the polycarbonate frame allows fluid flow from the fitting into the interior of the module. The perforated sheet is constructed from 3003 aluminum with $^{3}/_{16}$ inch holes drilled ¾ of an inch apart in a staggered pattern. Fluid on the interior of the polycarbonate frame can therefore pass freely through the perforated sheet and be allowed to wet the STE material. The pressure plate and gasket prevent the fluid from leaking out of the interior around the perimeter of the STE material. Fluid will continue to flow through the module's interior to the opposite side of the base frame where it exits through twelve $^{3}/_{16}$ inch holes drilled in that side (once again, only one is shown in the cross-sectional view for simplicity). A $^{1}/_{8}$ inch channel cut from the top of the frame and intersecting with each of the $^{3}/_{16}$ inch holes allows fluid to flow through the holes, make a 90° turn, through the $^{1}/_{8}$ inch channel, and out the top of the module. Plugs are then inserted into the end of each of the $^{3}/_{16}$ inch holes. These plugs function to prevent fluid from leaking out these holes at the right hand side of the module instead of flowing out of the top $^{1}/_{8}$ inch channel. These plugs are simply an artifact of the fabrication methods available to be used to create the polycarbonate base frame.

These modules were designed such that if two of them are assembled together with gaskets, they form a complete fluid circuit with simple barbed fitting tube attachment points, as Figure 4.8 shows below. As was previously mentioned, the complete STE consisted of four separate modules stacked one upon another. Because each set of two modules contains its own flow circuit, there were two separate flow circuits for the four modules.

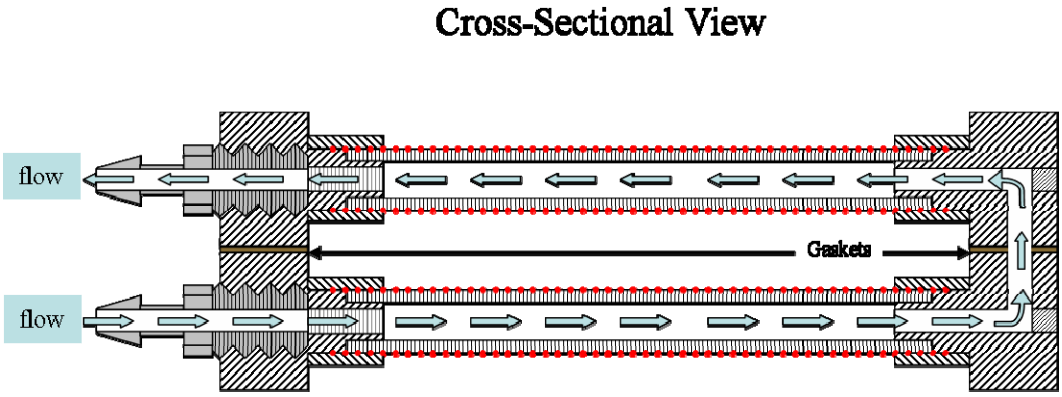

Figure 4.8 STE Flow Circuit Schematic

A picture of the completed set of four modules is shown in Figure 4.9. The modules are fastened together with six long screws.

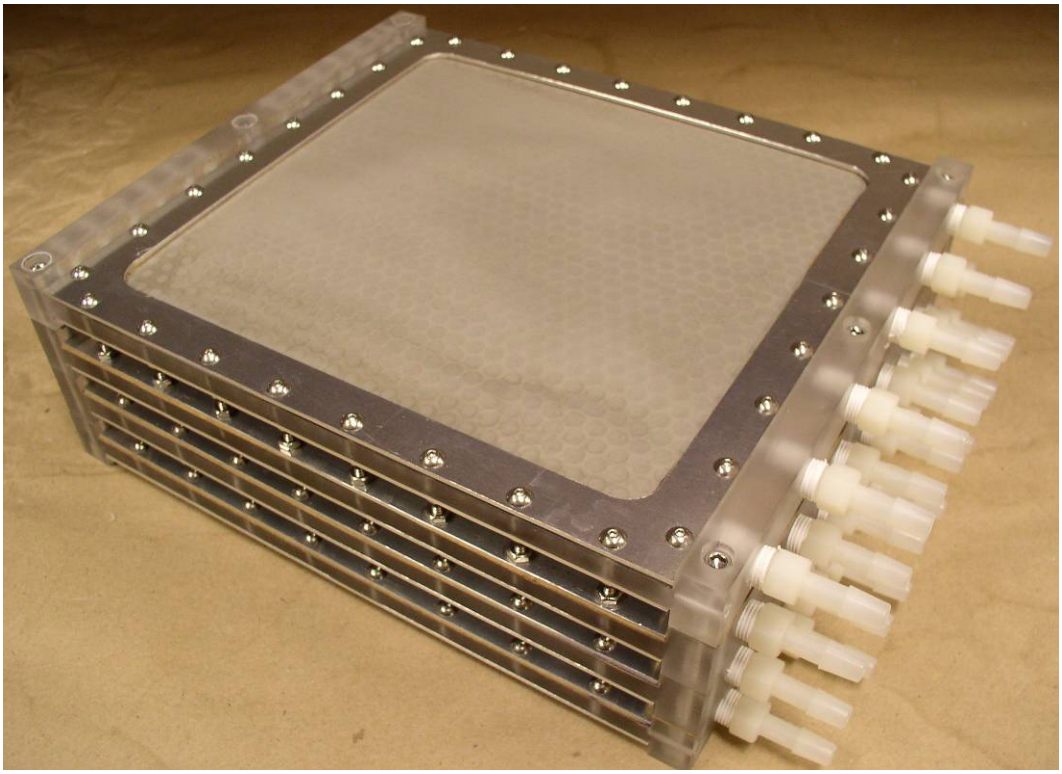

Figure 4.9 Assembled STE Modules

4.2.3 STE Docking

The STE was designed to dock into the existing docking port for the dryer's condenser module. In order to accomplish this, two plates were attached to either end of the STE modules such that the geometry mimicked that of the condenser module's sealing surfaces. Figure 4.10 shows these two sealing plates, or sealing surfaces, attached to the STE modules. These two plates have grooves machined into them that accept the same gaskets used for the condenser module. These gaskets ensure that the dryer's drying fluid does not leak into the atmosphere from the docking port.

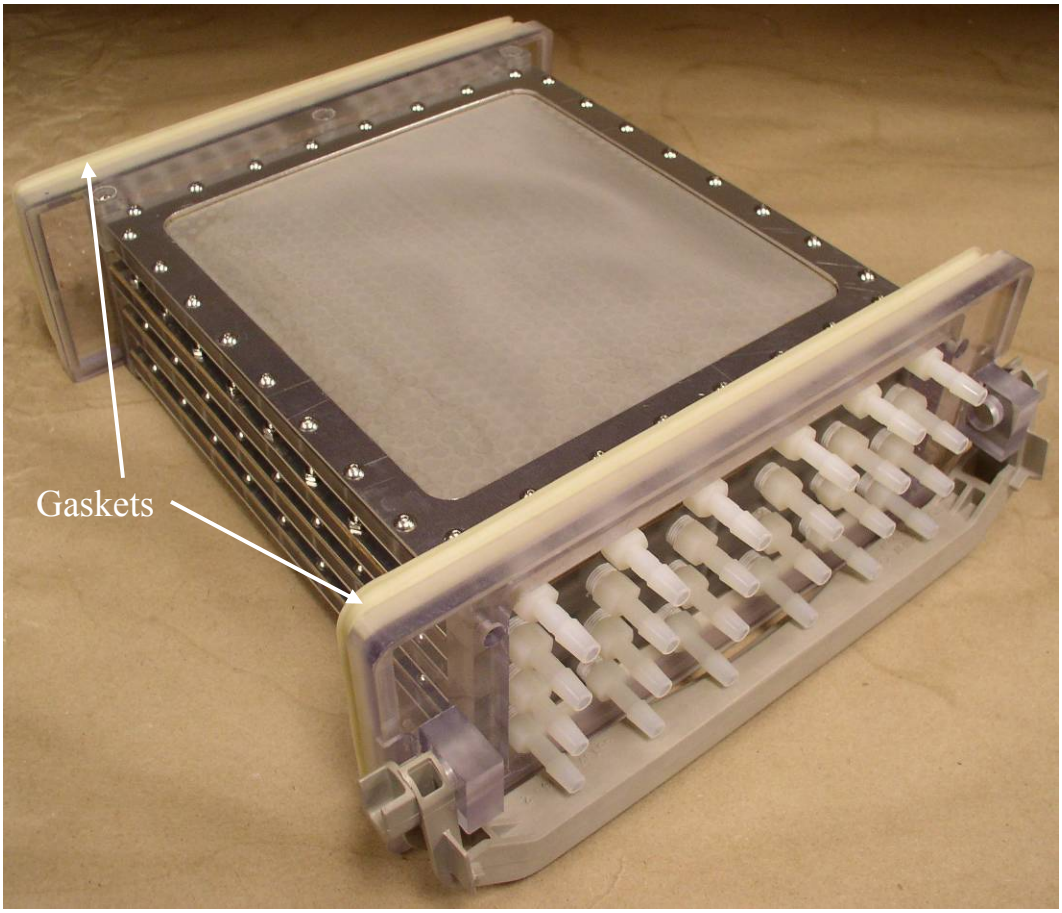

Figure 4.10 Assembled STE Modules with Docking Surfaces Attached

4.2.4 STE Drying Fluid Flow

The dryer's drying fluid is designed to pass between the STE modules in the same manner as the condenser. The drying fluid flow cross-sectional area is smaller for the STE than for the condenser, but the difference is minimal. The condenser has a cross-sectional area of *13.261* in^2 whereas the STE has a cross-sectional area of *18.01* in^2. This results in a *36%* increase in cross-sectional flow area.

4.2.5 STE Porous Material

Twilled weave wire cloth with ultra-small mesh openings was used to create the surface tension effects that were necessary for the STE. Gerard Daniel Worldwide was kind enough to donate quite a large sample of the wire cloth mesh for use in this experiment. Below, in Table 4.2, the specifications of the mesh are shown.

Table 4.2 Wire Cloth Specifications

Mesh	500 X 500
Weave Type	Twilled Weave
Material Type	316 Stainless Steel
Opening	0.001 inches

In the above table, the specifications are defined by wire cloth manufacturers as follows: "Mesh" is determined by counting the total number of openings from the center of any wire to the center of a parallel wire, one inch in distance away. "Twilled Weave" is the pattern of weave used where each wire goes under two wires, then over the next two wires, then under…et cetera. Figure 4.11 shows a close-up microscope picture of what the twilled weave looks like.

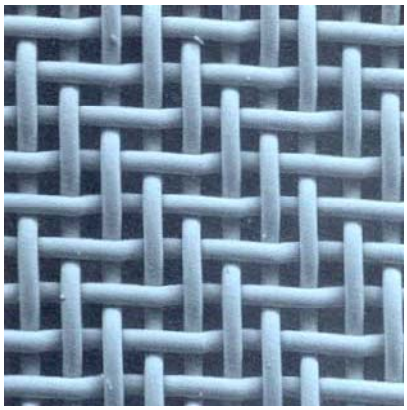

Figure 4.11 Twilled Weave Wire Cloth

Taken from: http://www.aircraftmaterialsuk.com/

"Opening" refers to the clear opening between adjacent parallel wires. This dimension is not affected by diameter of the wire. The opening of this mesh is stated by the manufacturer to be 0.001 inches, which is equivalent to 25.4 microns. Below, Figure 4.12 shows the material used for construction of the STE.

Figure 4.12 STE Wire Cloth supplied by Gerard Daniel Worldwide

4.2.6 STE Flow Circuiting

As was previously mentioned, two STE modules form a complete flow circuit that enters one module through six NPT barbed tube fittings and exits the other STE modules through six NPT barbed tube fittings. Because of the substantial number of tube fittings, manifolds were used to distribute the flow to and from the tube fittings. Figure 4.13 shows a picture of the manifolds attached.

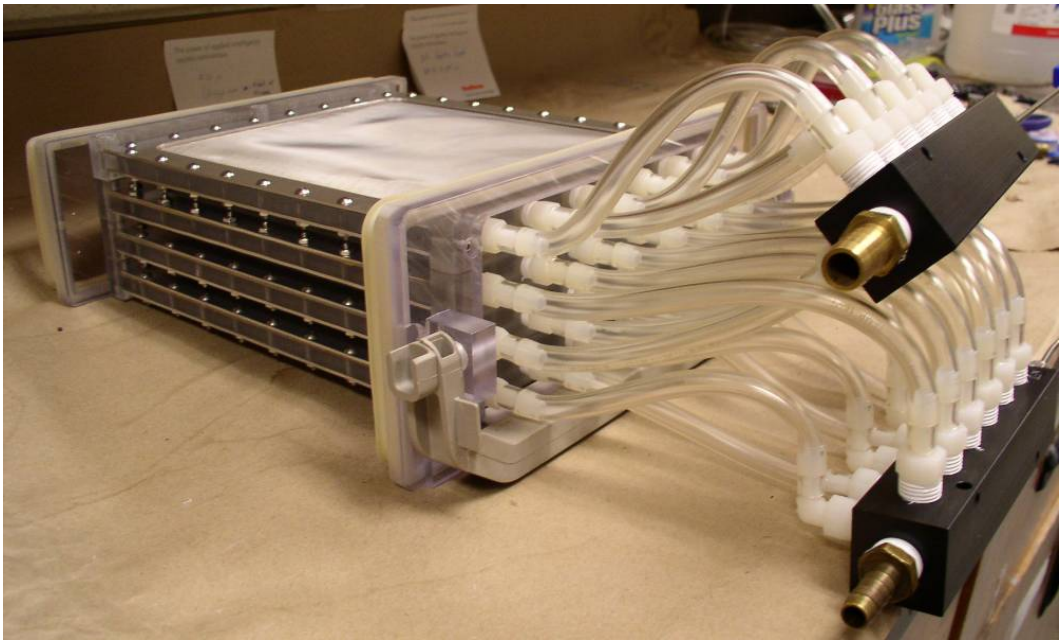

Figure 4.13 STE Flow Circuiting Manifolds Attached

4.2.7 Bubble-Point Test and Micron Rating

To evaluate the performance of the STE, a standard procedure is used which is thoroughly described in the SAE ARP901 Report entitled "Bubble-Point Test Method" which is referenced in the REFERENCES section of this work.

4.2.7.1 Scope

The Bubble-Point Test Method's scope was intended for measuring "the largest pore or hole in a filter or similar fluid-permeable porous structure." While the specific application of the porous structure is different for filtering applications, the method calculates the pressure discontinuity across the porous structure where the vapor and liquid phases meet, which is exactly what is needed for the current application.

4.2.7.2 Brief Method Outline

The STE is first closely inspected to insure that there are no contaminants on the surface that might alter the performance of the device. The STE is then immersed in American Chemical Society (ACS) reagent grade isopropanol (isopropyl alcohol), or IPA, and the fluid is allowed to completely wet the porous structure. Gas pressure is then applied to one side of the porous structure so that the liquid is completely displaced on that side. The gas pressure is then

increased to the point where gas is able to penetrate through the porous structure in a steady stream of bubbles. This point where the gas is able to penetrate through the structure is the largest pore. The STE is then turned to orient this area at the top of the STE. The pressure that was required to make the first bubble is then recorded as the pressure necessary to overcome the delicate balance between surface tension forces and gas pressure forces across the porous structure. Corrections are then made to account for hydrodynamic pressure as a function of immersion depth. This pressure is a standard characterization of the largest pore size of the STE.

4.2.7.3 Bubble-Point Test Experimental Setup

A schematic of experimental setup used to evaluate the bubble point of the STE is shown below in Figure 4.14.

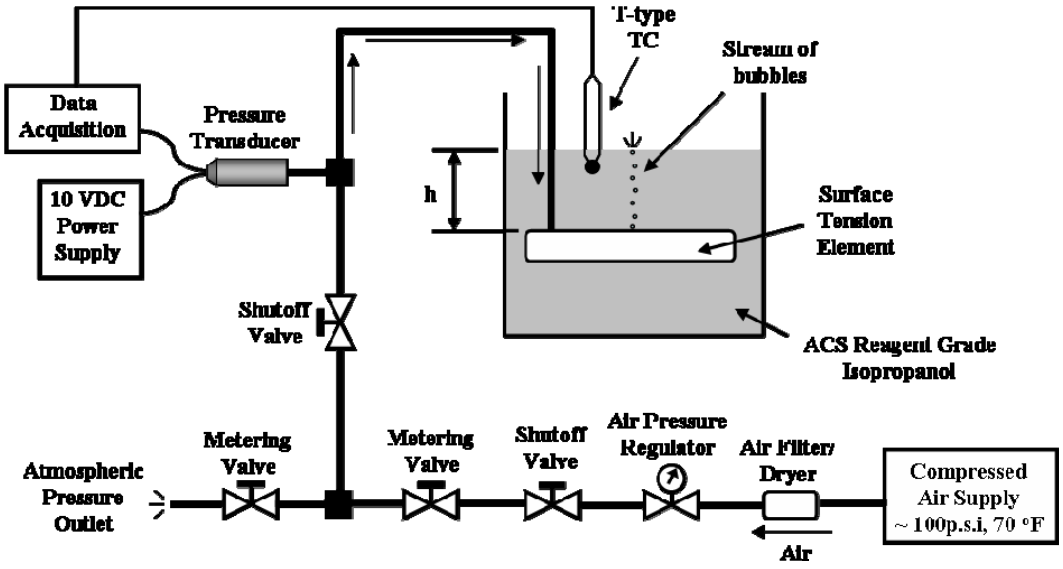

Figure 4.14 Bubble-Point Test Experimental Setup

Compressed air from the building is routed through a filter and dryer with a desiccant to remove the moisture content from the air. Next, an air pressure regulator is used to reduce the line pressure to about 5 *psi*. A series of metering and shutoff valves are then used to precisely control the pressure supplied to the interior of the STE. The first metering valve (closest to the compressed air supply) is used to control the total air flow through the later parts of the system while the second metering valve controls the pressure drop between the line and atmospheric. This combination allows the pressure inside the line, and hence the pressure supplied to the pressure transducer and STE, to be precisely controlled and slowly incremented up to the STE failure pressure. The extra shutoff valves are simply precautions to control which parts of the

line are pressurized. Table 4.3 gives detailed information regarding the specifications of each individual component.

Table 4.3 Bubble-Point Testing Plumbing Components

Item	Description
Filter / Dryer	*Speedaire* model 6ZC63A, 125 psi max, ¼" FNPT
Pressure Regulator	*Watts Fluidaire* model R364-02AG, 0-25 psi Regulated Pressure, 300psi Maximum Inlet Pressure, ¼" FNPT
Shutoff Valve	*Neles-Jamesbury* Clincher® Series 2000 Threaded-End Ball Valve, ¼" FNPT
Metering Valve	*Swagelok* model SS-1RS6 Stainless Steel Integral Bonnet Needle Valve, 0.73 Cv, 3/8" Swagelok Tube Fitting, Regulating Stem

Bubble Point Instrumentation

The pressure supplied to the STE is measured using an Omega Engineering PX-800-002GV pressure transducer capable of sensing 0-2.5 *psig*. The transducer outputs a 0-25mV signal proportional to the gage pressure. The manufacturer's stated accuracy is ±0.1% best fit straight line (BFSL) accuracy. An excitation voltage of 10VDC was supplied to the sensor by an Omega Engineering model PST-4130 adjustable output regulated voltage power supply specifically designed for use with pressure transducers. The transducer was calibrated with a micro-manometer in the range of 0 to 10 inches of water column (0 to 0.361273 *psi*). This low range appropriately captures the range of bubble point pressures that are typical for the STE modules.

The temperature of the IPA is measured with a common T-type thermocouple. Both the pressure transducer and thermocouple signals are routed to the data acquisition instrumentation for constant monitoring. The data acquisition consisted of a HP 34901A 20-Channel Armature Multiplexer card, a HP 34970A Data Acquisition/Switch Unit, and a 900MHz PC running LabVIEW 7 Express. A LabVIEW virtual instrument was created to talk to the HP 34970A commanding it to continuously measure the pressure and temperature signals and return them to the LabVIEW VI. Once the data was retrieved from the HP34970A, it then converted the signals

to the appropriate dimensions, displayed them on the front end of the instrument in graphical form, and recorded them in an excel spreadsheet for later evaluation.

4.2.7.4 Bubble-Point Test Liquid

The "standard referee test liquid" for the bubble-point test is specified to be American Chemical Society reagent grade isopropanol (isopropyl alcohol), or IPA. IPA has a surface tension of 21.15 *dynes/cm* ± 0.10 *dynes/cm* at 25 ^{o}C. Other liquids such as Ethanol 3-190, MIL-H-5606 hydraulic oil, or JP-5 fuel may be used, but IPA is the "standard referee test liquid", and is used as the test liquid for the bubble-point tests in these experiments.

4.2.7.5 Bubble-Point Testing Results

Initial testing of the STEs revealed several design flaws, but were encouraging in that the flaws did not severely impact the performance of the STE. It was noted that the majority of "largest pore" locations were along the gasket/STE interface. Figure 4.15 shows the leak developed when the internal pressure of the STE exceeds approximately 0.3 *psi* in IPA test liquid with a depth of immersion of approximately 1 inch. Prior to this pressure, no leaks could be detected.

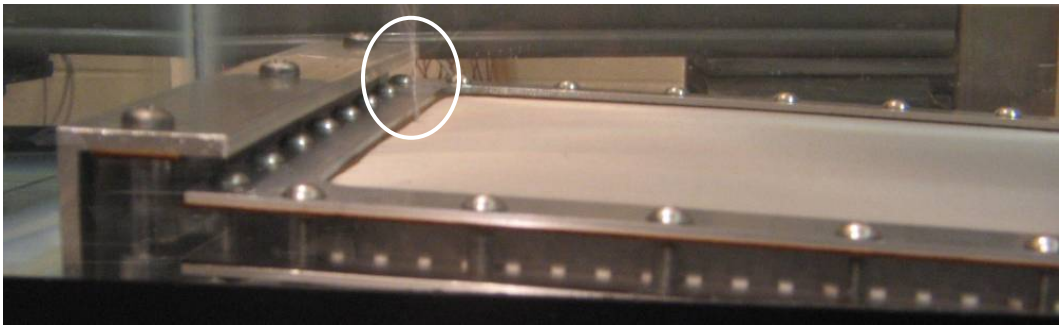

Figure 4.15 STE Bubble-Point Test Air Leak

After all of the rectifiable design flaws were fixed, the STEs were tested accordingly:

1. The STE module was visually inspected for any contaminants and thoroughly cleaned with IPA.
2. The STE module is then connected to the experimental set up and submerged in the test liquid, allowing the element to become completely flooded by the liquid. This insures proper wetting, which can significantly alter the results – see the "Bubble Point Anomalies" for a more detailed discussion.

3. The device is connected to the compressed air supply, the DAQ is started and data is written to a specified file. The pressure is then gradually raised by 0.1 *psi* per minute in the testing device by adjusting the needle valves.
4. While gradually increasing the pressure, the STE is observed carefully until the first continuous stream of bubbles appears from the specimen's surface. At this instant the shut-off valve closest to the operator is closed, cutting of the air supply and dropping the pressure down to zero. This effectively creates peaks in the data where the local maximum will represent the bubble-point pressure. The height of liquid above where the first stream of bubbles appeared is then measured to the nearest $^{1}/_{16}$" and recorded.
5. The location of the first continuous stream of bubbles did not always occur in the same place each test, thus measuring the immersion depth of each location is necessary.

This procedure was repeated five times for each side of each STE module to create five peaks and five samples of the Bubble-Point pressure. Figure 4.16 shows a sample of the data collected for STE module number 2, side A:

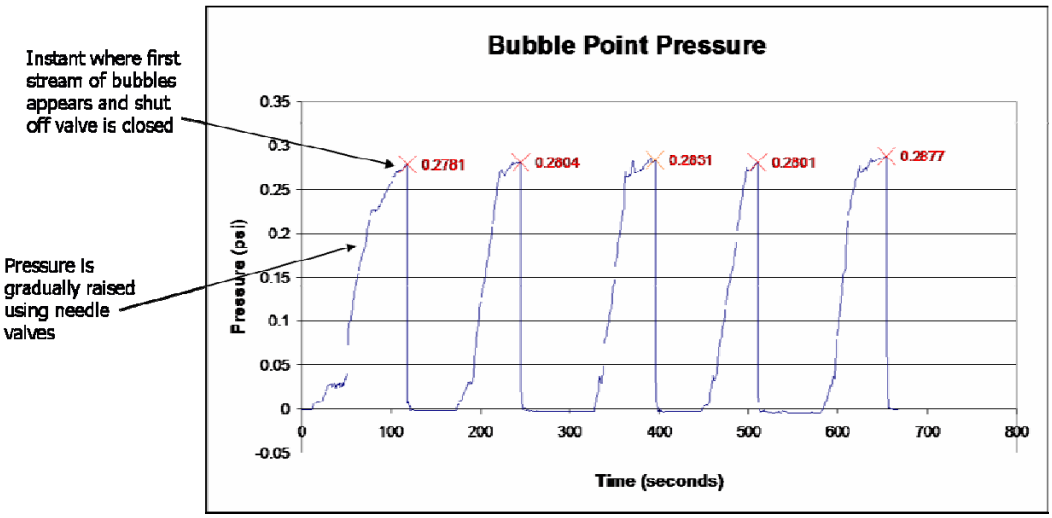

Figure 4.16 Bubble-Point Sample Data Graph

Once the Bubble-Point has been measured and corrected for hydrodynamic pressure, the circular capillary model, Equation 10, is employed to determine the largest pore size assuming that the IPA completely wets the pore ($\theta = 0^{o}$).

For example, for the first measurement on the graph above, the following data applies:

$$P_{bp} = 0.2781 \frac{lbf}{in^2}$$
$$h_{immersion} = .3125in$$
$$T_{IPA} = 71.84^o F$$
$$\rho_{IPA} = 0.02823 \frac{lb}{in^3}$$
$$\sigma_{IPA} = 1.22848 \cdot 10^{-4} \frac{lbf}{in}$$

The corrected Bubble-Point pressure is:

$$P_{bp\_corrected} = P_{bp} - \rho_{IPA} g h_{immersion}$$
$$P_{bp\_corrected} = 0.2781 \frac{lbf}{in^2} - 0.02823 \frac{lb}{in^3} \cdot \frac{32.2 ft}{s^2} \cdot \frac{lbf \cdot s^2}{32.2 lb \cdot ft} \cdot 0.3125in = 0.2693 \frac{lbf}{in^2}$$

The largest pore size is then calculated as follows:

$$D = \frac{4\sigma_{LV} \cos(\theta)}{\Delta P} = \frac{4 \cdot 1.22848 \cdot 10^{-4} \frac{lbf}{in} \cdot \cos(0)}{0.2693 \frac{lbf}{in^2}} = 0.001825in = 46.35 \mu m$$

The micron rating corresponding to the Bubble-Point test is therefore 46.35 microns. Table 4.4 shows the end result analysis of the tests.

Table 4.4 Bubble-Point Test Data Results

STE Module #	STE Side #	Average Micron Rating (μm)	Standard Deviation (μm)
1	A	54.2	0.45
	B	45.7	0.21
2	A	45.8	0.62
	B	44.5	0.51
3	A	46.0	0.64
	B	45.5	0.75
4	A	46.6	1.1
	B	46.0	0.85

When the STE modules were assembled, thought was given to how to maximize the capillary effect of the modules. Because of this, the modules were assembled with #1 being on

the bottom, #2 on top of that, and so on with #4 being on the top. This allowed a module with a smaller micron rating to be exposed to the highest pressure differential and the module with larger micron rating to be exposed to the least pressure differential, which allowed the entire STE assembly to be operated at higher overall pressure differentials.

If water at the following conditions is used as the working fluid, the maximum pressure differential across the STE elements can be found:

$$T_{H2O} = 70^{o} F$$

$$\rho_{H2O} = 1.936 \frac{slug}{ft^3}$$

$$\sigma_{H2O} = 4.97 \cdot 10^{-3} \frac{lbf}{ft}$$

$$D = 54.2 \mu m = 0.000178 ft$$

$$\Delta P = \frac{4\sigma_{H2O} \cos(\theta)}{D} = \frac{4 \cdot 4.97 \cdot 10^{-3} \frac{lbf}{ft} \cdot \cos(0)}{0.000178 ft} = 111.7 \frac{lbf}{ft^2} = 0.7757 \frac{lbf}{in^2}$$

$$\Delta P = 111.7 \frac{lbf}{ft^2} = \rho_{H2O} g h_{H2O}$$

$$h_{H2O} = \frac{111.7 \frac{lbf}{ft^2}}{62.34 \frac{lb}{ft^3} \cdot \frac{32.2 ft}{s^2} \cdot \frac{lbf \cdot s^2}{32.2 lb \cdot ft}} \cdot \frac{12 in}{ft} = 21.50 in$$

Therefore, the maximum height of water column that the STE can support is 21.5 inches, or a water pressure at 0.7757 *psi* vacuum.

Bubble-Point Testing Anomalies

One interesting observation was noted regarding the bubble-point pressure of the STE when the air leak occurred along the mesh/gasket interface. The following description documents the steps taken to produce this observation:

The pressure supplied to the interior of the STE is equalized with atmospheric pressure and the STE is allowed to completely fill with liquid such that the entire mesh is completely wetted. After this initial wetting phase, the pressure on the interior of the STE is increased until it is observed that the bubble-point pressure has been reached. This first measurement is recorded. At this point, the pressure is gradually reduced until the leak stops, and then slowly

increased again until the leak develops at the exact spot of the first leak. This second pressure is recorded. A comparison of the two pressure measurements shows that the first is significantly higher than the second. Typically, the first measurement's values were around 0.30 *psi* and the second measurement's values around 0.25 *psi*. If the pressure is once again reduced until the leak stops and then increased until the leak develops, the bubble-point pressure will remain at the lower value of around 0.25 *psi*. If the procedure is repeated, the same difference in bubble-point pressures will occur. This anomaly could possibly be attributed to air bubbles becoming "stuck" in the gasket interfacial area and preventing the IPA from re-wetting the slot. As air is re-applied to the STE, air lingering in the STE gasket's interface allows air to escape without having to overcome the capillary effects present with a wetted gasket interface.

4.2.8 STE Flow Loop

There were several important design criteria that were used to design the STE liquid flow loop. These factors included the fluid used as well as the control of the fluid pressure, flow rate, and temperature supplied to the STE. Because the STE is to be used to remove moisture, the obvious choice of an internal fluid is water. Water's high surface tension on the order of 75 dynes/cm makes it a very practical choice. Other fluids could be possible, but then the fluid mixing would have to be taken into consideration. On important factor to account for was that the absolute pressure of the water side of the STE must not exceed the pressure of the moist air on the air (drying fluid) side. If the internal pressure were to ever exceed the external pressure, water would leak out of the STE until the pressures were equalized. We must therefore operate the STE at a negative internal pressure. However, if the negative pressure difference ever exceeds the STE's bubble-point pressure, air will penetrate through the STE's porous material and the STE's ability to remove moisture will be compromised. Because of this, it was important to control the pressure inside the STE. Another consideration was that it is desirable to be able to control the flow rate of the water through the STE modules. By controlling the flow rate, the heating effect of the STE water is controlled. In other words, the STE is operating just like a heat exchanger. It was also important to have the ability to cool the water, going through the STE. As moisture is captured from the drying fluid, the energy heat of vaporization is added to the bulk fluid – which can significantly heat the water in the STE. Because the temperature of the water in the STE is essentially the temperature of the STE surface in contact with the drying

fluid, cooler water temperatures in the STE promote better moisture removal. Figure 4.17 shows a schematic of the flow loop that was constructed. A variable speed DC motor driven gear pump creates the necessary negative gage pressure required to draw water from a reservoir at atmospheric pressure, into a flow manifold where it is distributed to the two separate STE flow circuits, through the STE flow circuits, out of the flow circuits into a second flow manifold, and into the negative side of the gear pump. On the positive side of the pump, the water first flows through a filter to remove lint and any other contaminants in the water, through an air/water heat exchanger, and then finally to the reservoir. A blower fan forces cool room air through the air/water heat exchanger thus cooling the water in the flow loop.

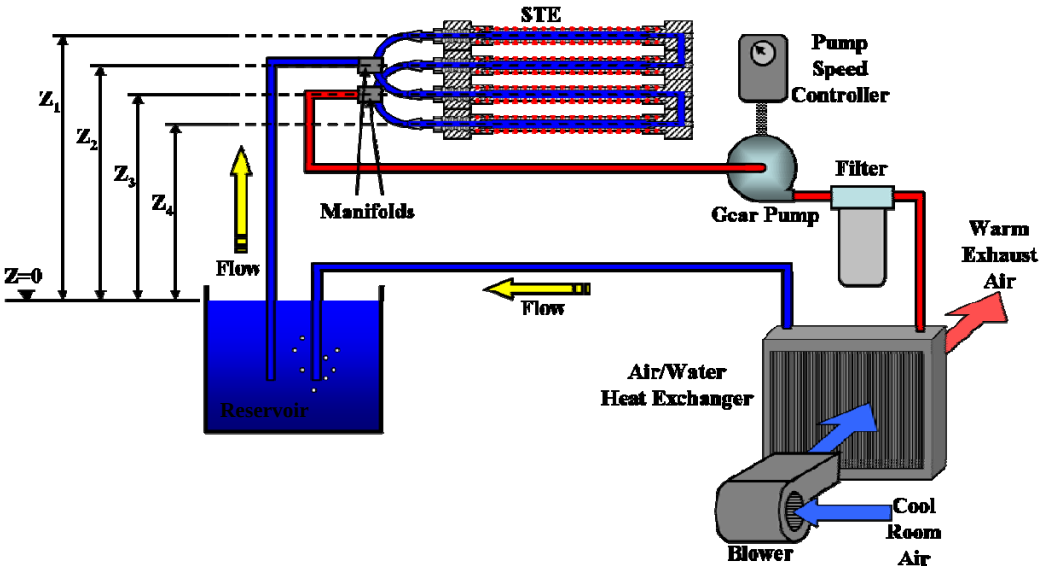

Figure 4.17 STE Flow Loop Schematic

Table 4.5 describes each of the components in greater detail. The exact model number of the Gear Pump is unknown due to the information sticker on the pump being damaged, but the manufacturer and model series of the pump were decipherable.

Table 4.5 STE Flow Loop Components

Item	Description
Gear Pump	*Tuthill* Control-Mate TXCM-series Magnet Drive Gear Pump
Gear Pump Controller	*Dart Controls* DC Motor Speed Control Model 253G-200E
Filter	*Aquapure* API12T Whole House Filter
Air/Water Heat Exchanger	*Peugeot* automotive compact heat exchanger
Blower	*Dayton* Model 4C006B, 1/40 H.P.
Reservoir	*Coleman* Cooler ~12.4 gallon capacity
Manifolds	Aluminum Distribution Manifold 12 Outlets, 90 Deg, 3/8" NPT Inlet X 1/4" NPT Outlet
Tubing from Reservoir to STE Modules	*Tygon* Clear PVC Flexible Tubing $^1/_2$" ID, $^5/_8$" OD, $^1/_{16}$" Wall Thickness
STE Manifold Tubing	*Tygon* Clear PVC Flexible Tubing $^1/_4$" ID, $^3/_8$" OD, $^1/_{16}$" Wall Thickness
Remaining Tubing	*Tygon* Clear PVC Flexible Tubing $^3/_8$" ID, $^1/_2$" OD, $^1/_{16}$" Wall Thickness

The gear pump's flow rate is a function of the supplied voltage to the pump's permanent magnet DC motor. This DC supply voltage was manually controlled with a potentiometer on the controller listed above. For all of the tests a pump setting of 4.5 out of 10 was used. At this rate, a simple calculation was performed to quantify the flow rate of the gear pump – the time necessary to fill a 3 liter container:

$$\frac{Volume}{time} = \frac{3l}{39.65s} = 0.07566\frac{l}{s} = 7.566E^{-5}\frac{m^3}{s} = 1.199gpm$$

The Air/Water heat exchanger was attached to one end of a flow box with the blower attached to the other end. The blower would force cool room into the flow box, through several wire screen filters, and finally out of the box through heat exchanger's air fins.

The reservoir was covered during tests by a thin plastic sheet in order to minimize evaporation of the water in the reservoir. It was by no means an air-tight seal, but it helped prevent water mass from leaving the system. The reservoir's approximate horizontal area was calculated as 0.15397 m^3.

Figure 4.18 shows a picture of the flow loop during an actual experiment. The dryer is visible in the upper-right corner with the STE installed in the dryer's condenser docking port (the lower left of the dryer).

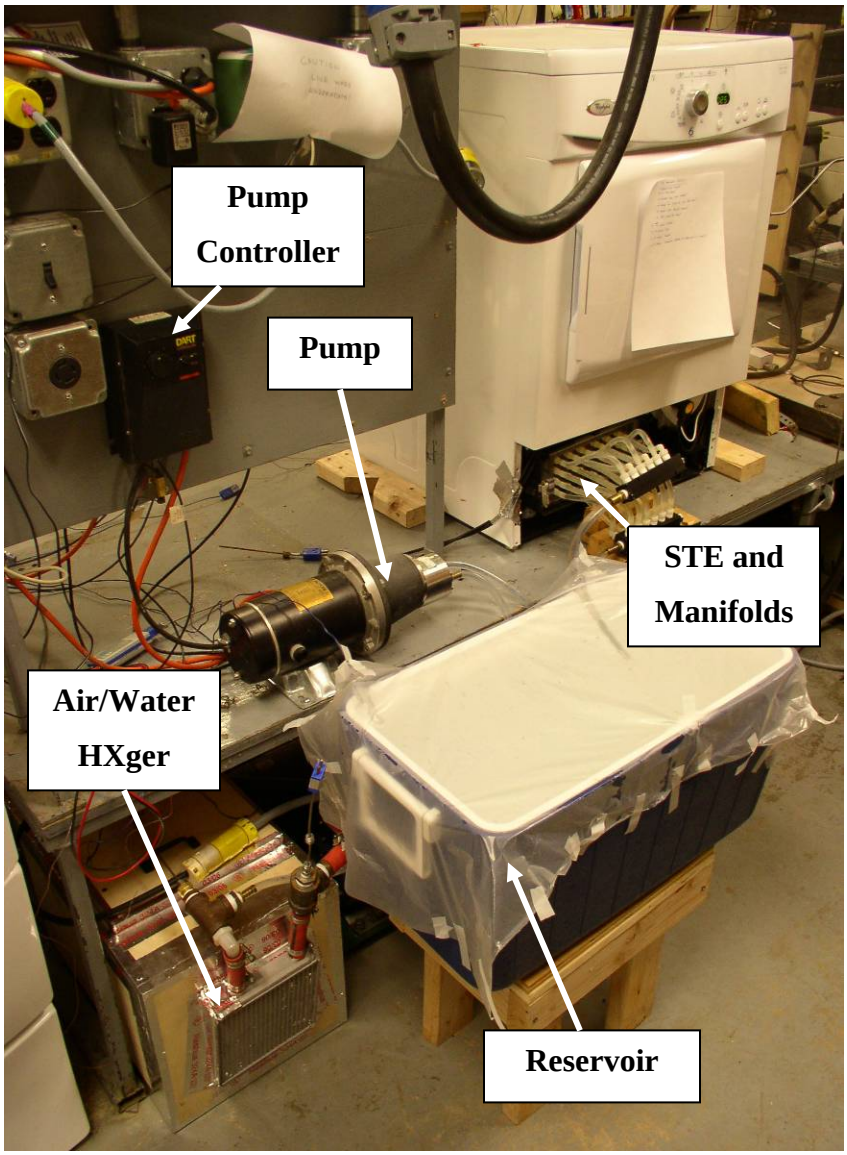

Figure 4.18 STE Water Loop Experimental Setup

4.3 Test Load Specifics

The performance of a residential dryer is greatly impacted by the types of textiles being dried. For example, cottons tend to hold on to water more than polyester type fabrics. The density, shape, and size of the fabrics also play a role in how efficiently a dryer operates. For this reason, a test load was chosen that attempts to conform as close as possible to the

International Electrotechnical Commission (IEC) standards for how to prepare a test load for measuring the energy consumption of a tumble dryer as well as Department of Energy (DOE) standards. The corresponding European standard is "IEC 61121 International Standard". In the standard, the material type and garment type to be used for testing varies from test to test. For example, for a 6 kilogram rated capacity dryer using a cotton test load, the test load consists of 2 sheets, 8 pillowcases, and the number of hand-towels required to make up the rated capacity. If an easy-care textile test load is used, then men's shirts and pillowcases are used. It is easy to see that there could be significant variation in the test load in shape, size, textile weave, and other parameters if this standard is used. For this reason, energy test cloths specified by the US DOE were used (Department of Energy,1997). Energy cloths are described as being a 50/50 blend of cotton/polyester, weighing 5.75 ounces per square yard, 24 inches wide by 36 inches long hemmed to 22 inches by 34 inches. DOE specifies a variety of rules for testing the cloth such as the total number of tests the cloths are allowed to run before they must be discarded that were not followed by our procedures. The reasoning for this was that the primary concern was not exactly replicating a standard energy consumption test, but wanted to experimentally quantify the difference between the dryer's energy consumption using the condenser verses the STE as a method for humidity removal.

Because the dryer utilized in these experiments had a rated capacity of 6kg, we chose to follow the IEC standards for the weight of the test load. IEC specifies that the weight of the test load must be as close as possible to the rated capacity of 6 kg as possible. The weight of the load must be recorded *after* the load has reached equilibrium moisture content with its surroundings. In our case, the ambient air temperature and humidity of the experimental testing facility was 23^{o}C and 28% respectively. At these conditions, the test load weighed 6.058 kg. IEC defines the rated capacity by the variable W_o.

4.3.1 Test Load IEC Moisture Specifications

The IEC standard quantifies the initial moisture content of the test load as follows:

$$\mu_i = 100 \times \frac{W_i - W_o}{W_o} \qquad \textbf{Equation 15}$$

where W_i is the weight of the load after the initial moisture content has been achieved. IEC specifies acceptable ranges for the initial moisture content as a function of the EU Energy Label as Table 4.6 shows.

Table 4.6 IEC Initial Moisture Content Specifications

	Nominal		Allowable Range	
EU Energy Label	A	B	A	B
Initial Moisture Content, μ_i	70%	60%	69% to 71%	59% to 61%

IEC also defines the Final Moisture Content at the end of the drying cycle as:

$$\mu_f = 100 \times \frac{W_f - W_o}{W_o} \qquad \textbf{Equation 16}$$

where W_f is the weight of the load after the drying cycle. IEC has similarly specified acceptable ranges for the final moisture content depending on the "Drying Programme" used as Table 4.7 shows.

Table 4.7 IEC Final Moisture Content Specifications

Drying Programme Used	Nominal,	Allowable Range
Dry Cotton, μ_f	0%	-3% to +3%
Iron Dry Cotton, μ_f	+12%	+8% to +16%
Easy-care Textile, μ_f	+2%	-1% to +5%

4.3.2 Test Load Preparation

The test load was initially placed in a Whirlpool Duet Horizontal-Axis Washing machine, model number GHW9150PW0. The washer was set to run on the "Rinse/Spin" cycle setting using the "Cold/Cold" temperature setting and the "High" spinning speed setting. Building tap water at approximately 18^{o}C was fed to the washer's water supply through a 5-micron water filter to remove dirt and rust from the tap water.

This procedure took roughly 20 minutes and achieved uniform initial moisture content (IMC) within the test load. The IMC varied from load to load with a mean of 66% and a standard deviation of 0.64% (evaluated using baseline test data). The mean initial moisture content is clearly out of the "allowable" range for the efficiency tests, but as was said before, the primary concern was in showing the difference between the condenser and STE dryer performance. The initial moisture content was fairly repeatable; therefore no countermeasures were employed to bring the IMC to within the allowable range of the IEC standard test.

Once the washing machine finished the cycle, the load's weight was measured and recorded as quickly as possible in an effort to minimize moisture exchange between the load and the ambient environment prior to initiating the drying test.

4.4 Test Configuration Instrumentation

This section describes the instrumentation used for the experimental setup.

4.4.1 Data Acquisition

The data acquisition consisted of two HP 34901A 20-Channel Armature Multiplexer cards, a HP 34970A Data Acquisition/Switch Unit, and a 900MHz PC running LabVIEW 7 Express. Two LabVIEW virtual instruments (VIs) were created to talk to the HP 34970A and make the required measurements. One VI was exclusively for STE tests and the other VI was for the condenser baseline tests. This was because the STE tests had additional measurements to be taken than the baseline tests. Each VI communicated with the HP 34970A commanding it to continuously measure and return the instrumentation signals to the VI. Once the data was retrieved, the VI then scaled the signals to the appropriate dimensions, displayed them on the front end of the instrument in graphical form, and recorded them in an excel spreadsheet format for later evaluation. This system worked very well in handling all of the signals at a sampling rate sufficient to capture the transient processes of the experiment. The system's capabilities and specifications are listed below in Table 4.8 and Table 4.9.

Table 4.8 HP 34901A 20-Channel Armature Multiplexer Specifications

20 channels of 300 Volt switching
2 channels for DC or AC current measurements (100 nA to 1A)
Built-in thermocouple reference junction
Switching speed of up to 60 channels per second
Connects to the internal multimeter of the HP 34970A

Table 4.9 HP 34970A Data Acquisition / Switch Unit Relevant Specifications

± (0.005% of reading + 0.004% of range) for DC voltage measurements
± (1^{o}C + accuracy of temperature probe) for T-type thermocouple measurements
System speed of 25 channels per second when directly transferring via RS-232 to a PC

4.4.2 Weighing Instrumentation

All weight measurements were made using an Arlyn Scales model SAW-H high accuracy Surface Acoustic Wave scale. The scale is capable of measuring from 0 – 200 lbs with a resolution of 0.002 lbs or 0-88kg with a resolution of 1 gram. The manufacturer's stated accuracy is ±0.01% full scale. The scale has the capability of outputting a 4-20mA signal corresponding to the weight as well as interfacing with a computer via USB connections. For the experiments described in this work, weight measurements were manually written down after looking at the scale's digital readout.

4.4.3 Dryer Instrumentation

The parameters that were of key importance to use were primarily humidity ratios, temperature ratios, and power consumption.

4.4.3.1 Humidity Instrumentation

Humidity measurements were taken with two separate humidity and temperature transmitters manufactured by Rotronic Instrument Corporation. For each measurement location, a separate Hygroflex 1 Industrial Humidity and Temperature Transmitter equipped with an IC-1 probe was used. The Hygroflex transmitter is capable of accepting a variety of probes, each specific to different temperature and humidity environmental conditions. The transmitter is

configured to output a 0 to 10 Volt DC signal corresponding to the measured temperature and a separate signal for the measured relative humidity. The IC-1 probe is capable of withstanding up to 200°C and has a protective metal screen that prevents the probe's sensing electronics from being damaged by large particles in the measurement environment. Each probe was factory calibrated for humidity and temperature and came with a certificate of calibration. The manufacturer's stated accuracy of the transmitter and probe unit is +/- 1% RH and +/- 0.2°C.

Each probe was positioned in the dryer's air stream such that the entire probe housing was immersed in the flow. This procedure greatly reduces the possibility of thermal gradients existing within the probe's housing as conduction heat transfer could travel through the probe to its surroundings outside the air duct, which can skew the temperature and/or humidity measurements. One sensor was positioned immediately after the lint filter and one right after the condenser, or heat exchanger as shown in Figure 4.19.

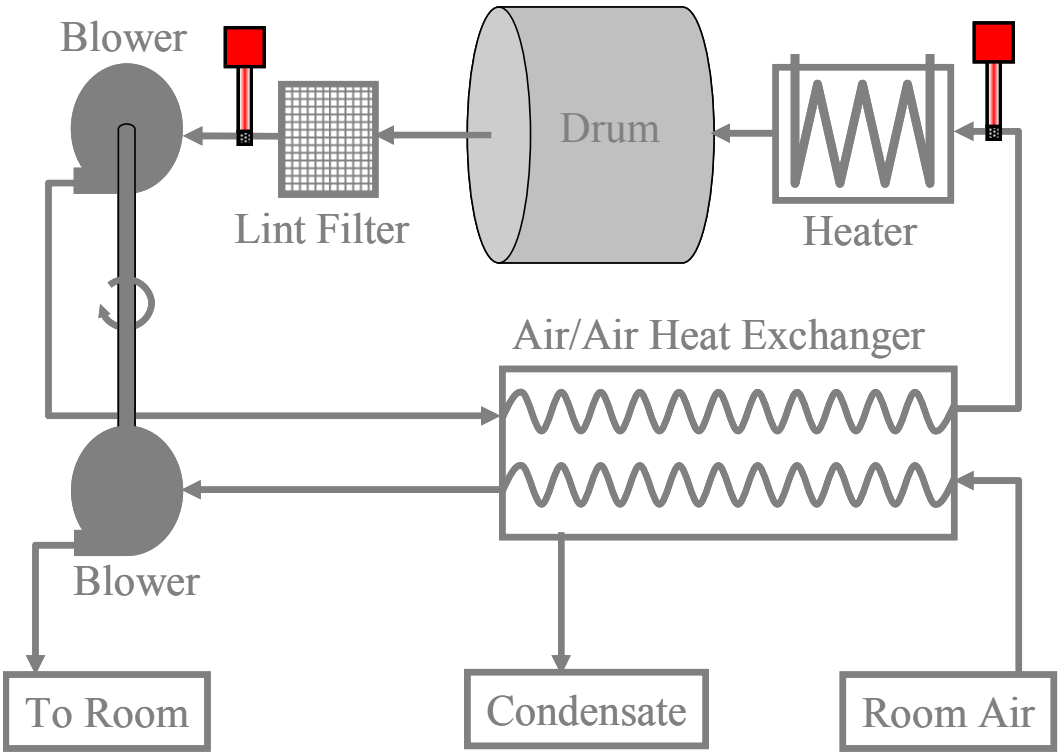

Figure 4.19 Locations of Humidity/Temperature Sensors

4.4.3.2 Temperature Instrumentation

Temperature within the dryer was measured at several locations in an effort to categorize the dryer's operation. In addition to the temperature sensing capabilities of the above humidity

instrumentation, T-type thermocouples were fabricated and utilized at the following locations on the schematic shown in Figure 4.20.

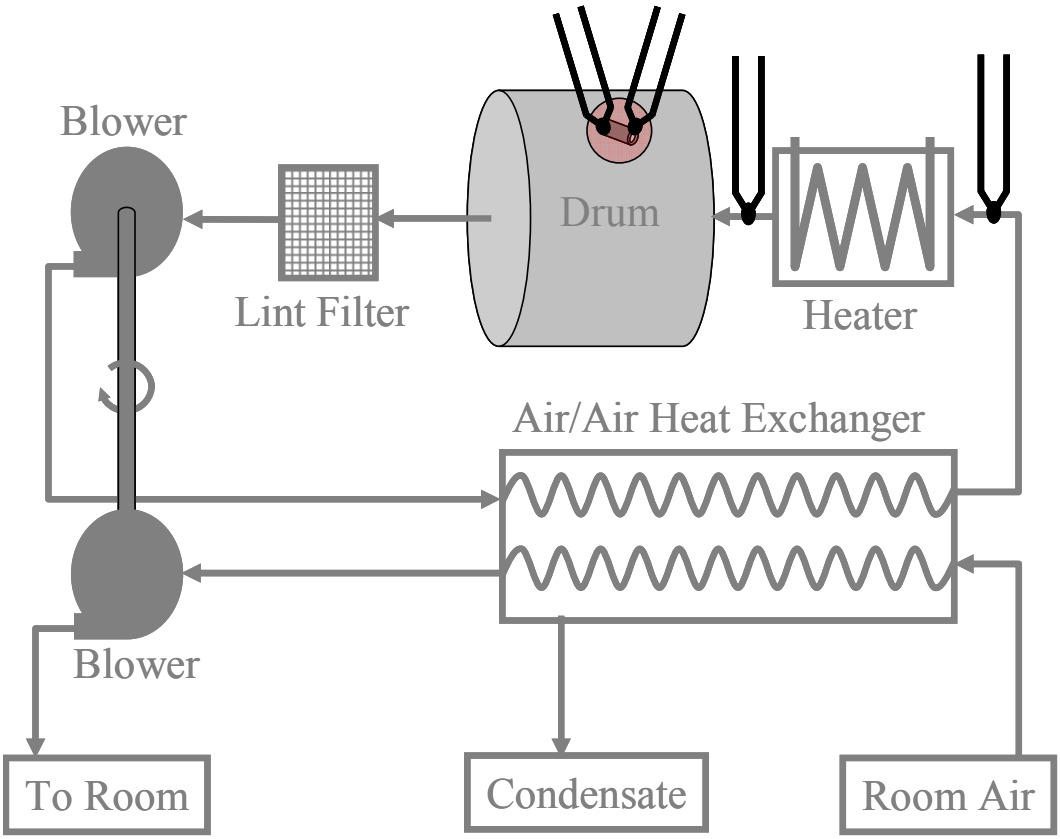

Figure 4.20 Locations of Thermocouples

Two thermocouples are located at the top of the rear bulkhead in the drum. These thermocouples were housed in a ¾" OD copper tube approximately 2 $^{3}/_{8}$" long. The first thermocouple's junction was suspended in the air such that it would measure the temperature of the air while the second's was attached to the interior of the copper tube wall. The location of the tube is circled and shown in Figure 4.21.

Figure 4.21 Thermocouple Tube Housing

The purpose of placing the thermocouples in the copper tube was initially for two reasons, which are described in the following paragraphs. However, it was determined that the second reason did not come into play for these experiments after initial testing.

The primary purpose of the tube is to protect the thermocouples from the tumbling action of the clothes. In previous tests were a thermocouple was simply suspended in the air at the top of the drum cavity without any protection (thermocouple wires passed through the rear bulkhead sheet metal wall), the thermocouple wires ended up being sheared off because of the tumbling clothes repetitively forcing the wires against the sharp sheet metal rear bulkhead wall. By using the copper tube, the wires are protected from this occurring.

Radiation shielding is the secondary purpose for using the tube. Since the heating element used to control the drying fluid air temperature was in line of sight of the thermocouple location, erroneous temperature readings due to radiation was a concern. By placing a thermocouple on the interior of the copper tube wall, the copper's temperature could be determined. Using this method, if the copper tube temperature was substantially higher than the air temperature, a correction for radiation effects could be utilized to account for radiative

heating of the thermocouple. It was later determined that radiation effects from copper tube to the air suspended thermocouple were negligible due to nearly identical temperatures.

At the very end of one test, the cloth load became tangled around the copper tube, and caused the belt that rotates the drum to overheat and fail. The data from the test was not compromised but modifications had to be made to the experimental setup in addition to replacing the drum belt. The copper tube was removed and the thermocouples originally in the tube were simply tapped to the dryer's rear bulkhead using aluminum high-heat tape. This prevented the clothes from becoming tangled again and breaking the replacement belt. Subsequent testing indicated that the operation of the drum had not been impacted after the modifications. The data from the thermocouple temperatures indicated that the thermocouples were in good thermal contact with the rear bulkhead (due to a substantially increased time constant), but the temperatures recorded were of roughly the same magnitude as before. Since the thermocouple temperatures were primarily used to monitor the operation of the dryer and not for analysis purposes, the modifications did not alter the validity of using the data of tests from both before and after the modification.

4.4.3.3 Energy Consumption Instrumentation

The instantaneous power consumption of the dryer was continuously monitored utilizing a precision AC watt transducer. The specifications of the instrument are listed below in Table 4.10.

Table 4.10 Precision Watt Transducer Specifications

Parameter	Description
Manufacturer	Ohio Semitronics, Inc.
Model Number	GW5-020D
Number of Sensing Elements	One
Number of Phases	Single
AC Volts	0-300
AC Amps	0-20
AC Frequency	58-62 Hz
Full Scale Watts	4000
Output	0-10 VDC
Accuracy	±0.2% of reading

By integrating the instantaneous power consumption of the dryer over time, the dryer's (not including the 3-phase drive motor) total energy consumption can be calculated. The watt transducer continuously monitors the instantaneous power consumed by the dryer and outputs a 0-10 Volt DC signal proportional to 0 to Full Scale Power Consumption. For example, if the dryer is consuming 2400 W, then the output would be 6 VDC.

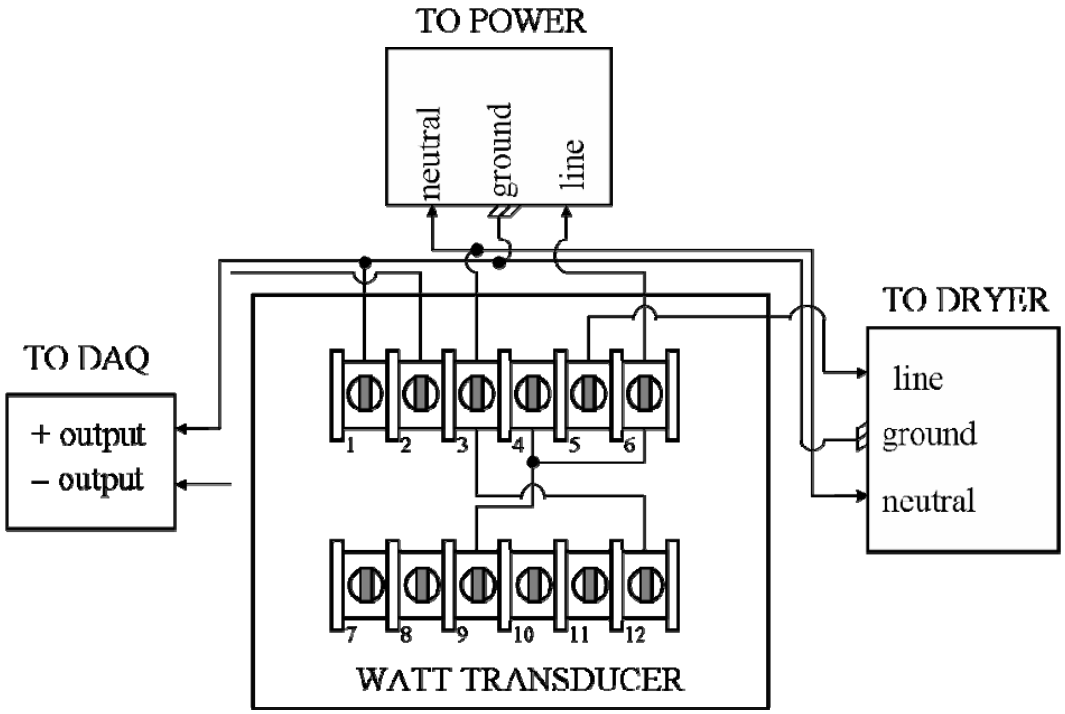

Figure 4.22 Watt Transducer Wiring Schematic

4.4.4 Water loop instrumentation

Important parameters that were to be recorded for the STE water loop, were temperatures, flow rates, and pressures. For the actual tests, the temperature was continuously recorded in the reservoir and at the outlet of the heat exchanger using immersion T-type thermocouples. A precision 0.5Ω - 25 watt energy-dissipating resistor, R_1, was inserted into the positive supply voltage line going from the speed controller to the pump motor. A simple calculation using the voltage drop across A and B and the drop across B and C allows for the gear pump's power consumption to be quantified:

$$P_{pump} = VI = V_{AB} \cdot \frac{V_{BC}}{R_1} = 2 \cdot V_{AB} \cdot V_{BC}$$

Figure 4.23 shows the locations of the various voltage measurement locations and thermocouple locations.

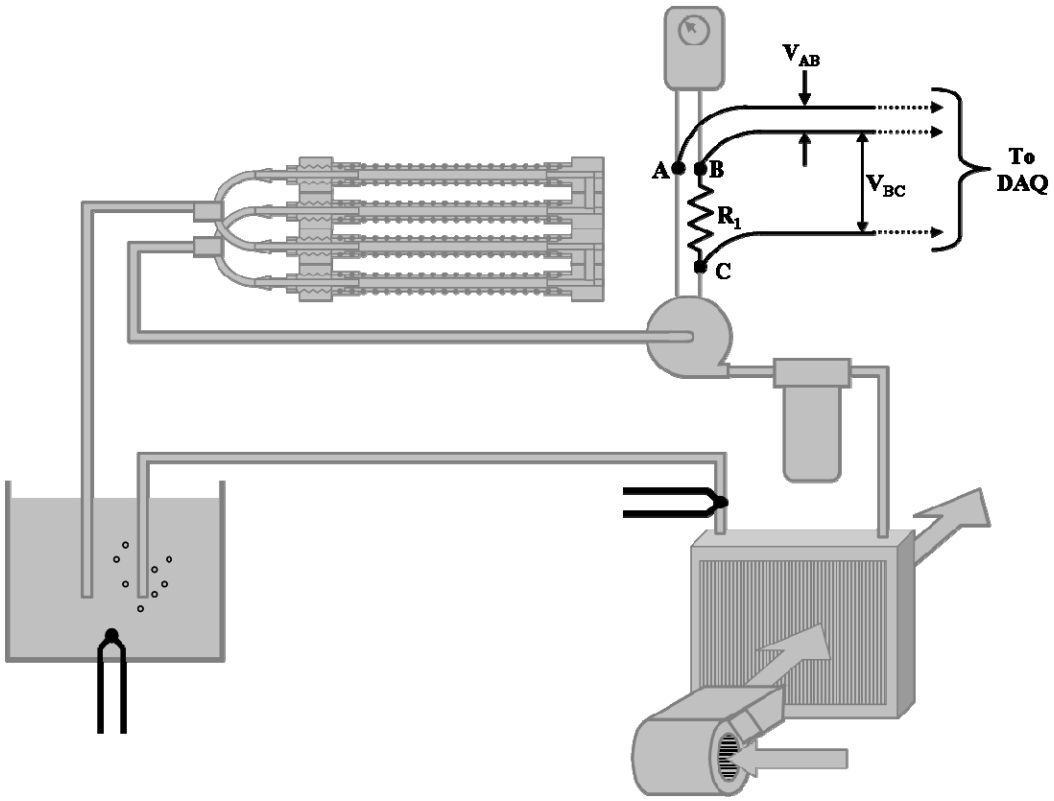

Figure 4.23 STE Flow Loop Instrumentation Schematic

CHAPTER 5 - Analytical STE Model

This section describes the analytical model that attempts to predict the performance of the STE element. The key phenomenon that is necessary to model the STE is fact that there is no thin film of condensate on the surface of the STE as is the case of a typical condenser undergoing filmwise condensation. As was previously discussed in Chapter 2, this film greatly hinders the condenser's ability to remove moisture. Because the STE's mesh automatically draws liquid condensate through it into the bulk fluid flow on inside the STE, the thin liquid condensate film does not exist on the STE surface, allowing the temperature of the bulk fluid flow inside the STE to be essentially the same as the surface temperature. This is the most important advantage of the STE module over a traditional condenser – the fact that the temperature of the STE surface in contact with the drying fluid is essentially the same as that of the bulk fluid flowing through the STE interior.

5.1 Modeling Methods

The STE was modeled as a parallel-flow heat exchanger, thus being able to use the simplified log-mean temperature and mass concentration differences to calculate the thermal and mass fluxes. The STE assembly actually behaves more like a cross-flow heat exchanger than the parallel-flow type. To ensure that this difference was not significantly influencing the results of the analysis, the model was also solved using counter-flow heat exchanger equations. When this was done, the correction factor used to modify the log-mean heat and mass transfer equations for cross-flow conditions was found to be nearly unity for all cases. Also, the results obtained from the model using the counter-flow equations do not significantly deviate from the outcome of the parallel-flow analysis. These results indicate that the assumption of parallel-flow is reasonable for this analysis. The following are the major assumptions made in modeling the STE:

1. STE behaves like a parallel-flow heat exchanger
2. Temperature within the CVs differs only along the length of the STE and not perpendicular to the STE wire mesh interface.
3. Both moist air and water vapor behave as ideal gasses.
4. Mass transfer between the CVs occurs only as saturated water vapor

5. Pressure remains constant in both CVs.

5.1.1 Model Governing Equations

The best place to start is with geometrical understanding of the device and how it interacts with the drying fluid. Figure 5.1 shows two control volumes (CVs) which represent each side of the STE surface. Warm, moist air from the dryer is pushed through the air CV while cool, liquid water from the reservoir is drawn through the water CV. To simulate the presence of the STE wire mesh separating the moist air and liquid water, both heat and mass transfer occurs across the boundary between the two CVs, which are represented by q and $\dot{m}_c$ respectively.

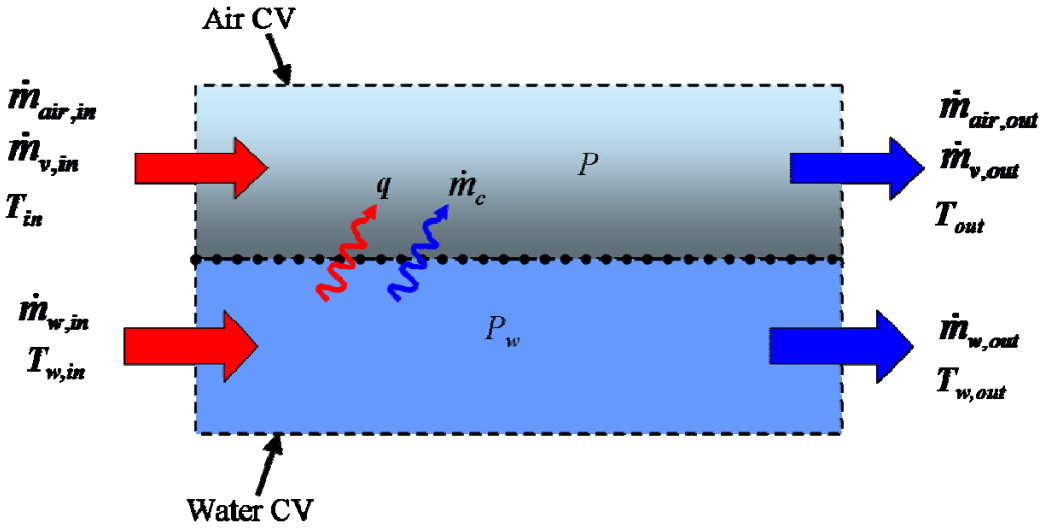

Figure 5.1 Model Schematic

The heat transfer can be calculated using standard heat exchanger heat transfer equations (Incropera, 2002). If it is first assumed the direction of heat transfer is assumed as in the above figure, one can account for the heat transfer to the air CV accordingly:

$$q = \bar{h} \cdot A_{thermal} \cdot \Delta T_{LM} \qquad \textbf{Equation 17}$$

where $\bar{h}$ is the average heat transfer coefficient, $A_{thermal}$ is the effective heat transfer area, and ΔT_{LM} is the log-mean temperature difference. The log-mean temperature difference is calculated accordingly:

$$\Delta T_{LM} = \left[\frac{\left(T_{w,out} - T_{out}\right) - \left(T_{w,in} - T_{in}\right)}{\ln\left(\left(T_{w,out} - T_{out}\right)/\left(T_{w,in} - T_{in}\right)\right)} \right] \qquad \textbf{Equation 18}$$

Mass transfer, is assumed to be driven by diffusion and fluid motion (advection), and is determined by the log-mean concentration difference between the surface and the bulk drying fluid flow:

$$\dot{m}_c = \overline{h_m} \cdot A_{mass} \cdot \Delta C_{LM} \qquad \textbf{Equation 19}$$

where $\overline{h_m}$ is the mass transfer advection coefficient, A_{mass} is the effective mass transfer area, and ΔC_{LM} is the log-mean concentration difference of the water vapor component of the moist air. The mass transfer coefficient is derived via the heat/mass transfer analogy. The log-mean concentration difference is calculated accordingly:

$$\Delta C_{LM} = \left[\frac{\left(\rho_{surface,out} - \rho_{out}\right) - \left(\rho_{surface,in} - \rho_{in}\right)}{\ln\left(\left(\rho_{surface,out} - \rho_{out}\right)/\left(\rho_{surface,in} - \rho_{in}\right)\right)} \right] \qquad \textbf{Equation 20}$$

where $\rho_{surface}$ is the water vapor concentration at the surface of the STE and ρ is the water vapor concentration in the bulk air mixture. The surface concentration is calculated assuming ideal gas behavior:

$$\rho_{surface} = \frac{P_{v,surface}}{R_g T_w}$$

Similarly, the bulk water vapor concentration is calculated:

$$\rho = \frac{P_v}{R_g T}$$

If a first law energy balance is done for the liquid water control volume, this results in:

$$q = \dot{m}_{w,in} \cdot h_{w,in} - \left(\dot{m}_{w,in} - \dot{m}_c\right) \cdot h_{w,out} - \dot{m}_c \cdot h_c \qquad \textbf{Equation 21}$$

where h_c is the enthalpy of the condensate (assumed to be saturated vapor). The condensate enthalpy is calculated at the average of the inlet and outlet water temperatures. This type of energy accounting allows for the energy associated with latent heat to be incorporated into the enthalpy instead of utilizing another equation equating this energy with the mass flow rate of the condensate times the heat of vaporization.

Similarly, an energy balance may be calculated for the air CV assuming that the dry air mass flow rate is constant:

$$q = -\left[\dot{m}_{air}\left(h_{in} - h_{out}\right) + \dot{m}_c \cdot h_c\right] \qquad \textbf{Equation 22}$$

where the enthalpies of the moist air mixture are expressed in *kJ* per *kg* of dry air. If these equations are analyzed, there are a total of 4 unknowns and 4 equations, thus the system is solvable.

5.1.2 Drying Fluid Flow Characterization

The STE was approximated as a sheet of liquid water suspended in the drying fluid flow. The dryer's centrifugal fan, located six inches upstream from the STE modules, directly blows the drying fluid across the STE modules. Because of this, the drying fluid flow is assumed to be turbulent. The geometry of the STE lent itself well to being modeled as channel flow where hydraulic diameters replaced circular diameters in the appropriate equations and correlations. Figure 5.2 shows a cross-sectional view of the orientation of two of the STE modules to the drying fluid flow.

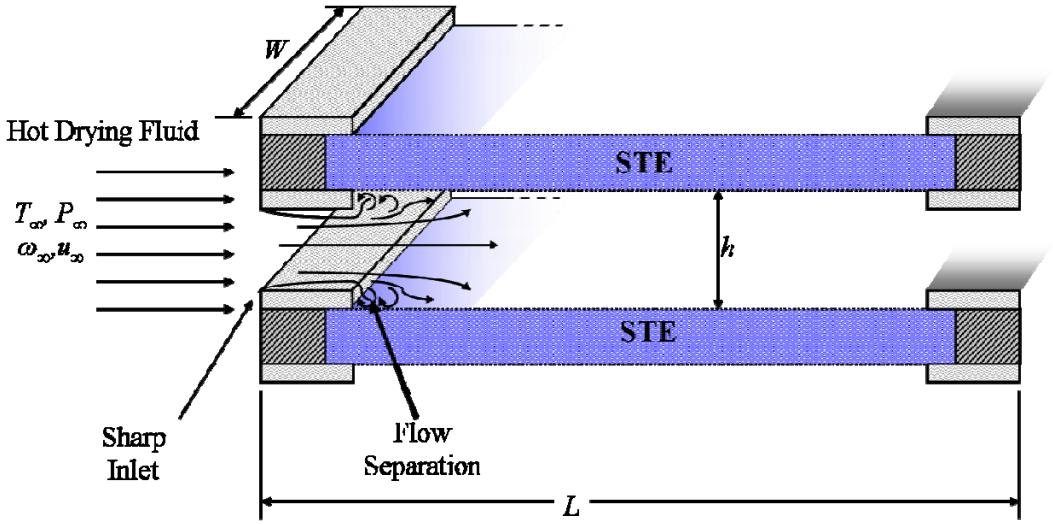

Figure 5.2 STE Drying Fluid Flow Orientation

As shown above, flow from the dryer's enters through the rather sharp inlet, initially flowing over the STE's pressure plate. As the flow leaves the pressure plate, there is a sudden change in the height between the plates of $^1/_8$ of an inch where flow separation is likely to occur. For the purposes of characterizing the flow, the following measurements were made:

$$L = 8.000in = 0.2032m$$
$$W = 8.394in = 0.2132m$$
$$h = .5212in = 0.01324m$$

Because there are four STE modules stacked one upon another with gasketing material, the total cross-sectional flow area can be found by multiplying the void vertical height by the width. The total height of the STE is equal to 3.346 *in,* or 0.08499 *m*. The void vertical height, h_{void}, is found by subtracting four times the STE module thickness from the total height, which equals 2.145 *in*, or 0.05448 *m*. The total cross-sectional flow area may now be calculated, which results in 18.01 in^2, or 0.01162 m^2.

The manufacturer of the dryer states that the nominal volumetric flow rate of the dryer's drying fluid centrifugal fan is 195.0 m^3/hr or 0.05417 m^3/s. As a rough approximation, the flow is assumed to be uniform. This assumption allows us to calculate an average drying fluid flow velocity as follows:

$$V_{STE} = \frac{Q}{A} = \frac{0.05417 \frac{m^3}{s}}{0.01162 m^2} = 4.662 \frac{m}{s}$$

The hydraulic diameter of each channel is calculated as four times the cross-sectional flow area of the channel divided by the wetted perimeter of the channel as follows:

$$D_h = \frac{4A_{channel}}{P_{channel}} = \frac{4(Wh)}{2W + 2h} = \frac{2(.2132m \cdot 0.01324m)}{.2132m + 0.01324m} = 0.02493m$$

In experiments where the temperature and humidity ratio of the drying fluid were measured, it was seen that typical values for the drying fluid as it entered the docking port housing the STE were 60°C dry-bulb and 0.1 kg H_2O per kg Dry Air respectively. These values were taken during the mid-point of the drying cycle. The Reynolds number was calculated as a quick check to determine whether the flow was laminar or turbulent. For moist air at 101.574 kPa (approximate pressure of drying fluid at this point) and at the temperature and humidity ratio stated above, the following properties of the drying fluid were calculated:

$$\rho = 1.0068 \frac{kg}{m^3}$$

$$\mu = 1.8693 \cdot 10^{-5} \frac{N \cdot s}{m^2}$$

$$\Pr = 0.77279$$

$$Sc = 0.7165$$

$$D_{ab} = 2.5913 \cdot 10^{-5} \frac{m^2}{s}$$

Therefore the appropriate Reynolds number describing the flow is calculated as:

$$\mathrm{Re}_{Dh} = \frac{\rho V_{STE} D_h}{\mu} = \frac{1.0068\frac{kg}{m^3} \cdot 4.662\frac{m}{s} \cdot 0.02493m}{1.8693 \cdot 10^{-5}\frac{N \cdot s}{m^2} \cdot \frac{kg \cdot m}{N \cdot s^2}} = 6260$$

which is clearly above the critical $\mathrm{Re}_{\mathrm{Dh,crit}}$ number of 2100~2300, thus our assumption that the flow is turbulent is valid.

5.1.3 Drying Fluid Fully-Developed Entry Length

As flow enters the STE channels, care must be taken that a numerical heat and mass transfer correlation for fully-developed flow is not applied to an entry-length problem and vice-versa. It is generally known that the hydrodynamic fully-developed entry length of the turbulent drying fluid flow can be approximated by the following expression (Incropera, 2002):

$$10 \le \left(\frac{x_{fd.h}}{D}\right)_{turbulent} \le 60 \qquad \textbf{Equation 23}$$

If the length of the plate is 8 *in*, or 0.2032 *m*, this ratio can be calculated and compared to the numbers above in Equation 23:

$$\left(\frac{L}{D_h}\right) = \frac{0.2032m}{0.02493m} = 8.15 < \left(\frac{x_{fd.h}}{D}\right)_{turbulent}$$

This indicates that fully developed hydrodynamic flow does not occur until after the flow has exited the STE channel, thus the entire case must be addressed as an entry-length problem.

5.1.4 Drying Fluid Heat and Mass Transfer Correlations

For hydrodynamic fully-developed turbulent flow in circular tubes with relatively small Reynolds numbers, Gnielinski's correlation for Nusselt number was used to obtain the fully developed Nusselt number (Incropera, 2002) as a function of the moody friction factor, *f*:

$$Nu_D = \frac{(f/8)(\mathrm{Re}_D - 1000)\mathrm{Pr}}{1 + 12.7(f/8)^{1/2}\left(\mathrm{Pr}^{2/3} - 1\right)} \qquad \textbf{Equation 24}$$

where the following restrictions to the Prandtl and Reynolds numbers must be followed:

$$0.5 \le \mathrm{Pr} \le 2000$$

$$3000 \le \mathrm{Re}_D \le 5 \cdot 10^6$$

To apply this correlation to channel flow, Re_D is replaced by Re_{Dh}. If we invoke the heat-mass transfer analogy, then the Sherwood number is similarly calculated by replacing the Prandtl number with the Schmidt number in Equation 24:

$$Sh_D = \frac{(f/8)(\mathrm{Re}_D - 1000)Sc}{1 + 12.7(f/8)^{1/2}\left(Sc^{2/3} - 1\right)} \qquad \textbf{Equation 25}$$

This correlation is similarly modified to replace the circular diameter based Reynolds number with the hydraulic diameter based Reynolds number. The moody friction factor, f, for the above relations was iteratively solved by utilizing the Colebrook formula (Munson, 2002):

$$\frac{1}{\sqrt{f}} = -2.0\log\left(\frac{\varepsilon/D_h}{3.7} + \frac{2.51}{\mathrm{Re}_{D_h}\sqrt{f}}\right) \qquad \textbf{Equation 26}$$

A surface roughness of 0.5 *mm* was used to approximate the roughness of the STE wire mesh surface. In order to correct the above correlations to account for fully-developed conditions never occurring and the entire problem being an entry-length one, Molki and Sparrow's correlation was used (Molki, 1986):

$$\frac{\overline{Nu}_D}{Nu_{D,fd}} = 1 + \frac{a}{(X/D)^b} \qquad \textbf{Equation 27}$$

where the values of a and b are functions of the Reynolds number:

$$a = 23.99 \cdot \mathrm{Re}_D^{-0.230} \qquad \textbf{Equation 28}$$

$$b = -2.08 \cdot 10^{-6} \cdot \mathrm{Re}_D + 0.815 \qquad \textbf{Equation 29}$$

This correlation was designed for the case of a sharp inlet where flow separation tends to occur, thus, the correlation applies to the current experiment. To see the effect of accounting for the entrance length in the above situation, the calculations are performed as follows:

$$a = 23.99 \cdot \mathrm{Re}_D^{-0.230} = 23.99 \cdot (6260)^{-0.230} = 3.21232$$
$$b = -2.08 \cdot 10^{-6} \cdot \mathrm{Re}_D + 0.815 = -2.08 \cdot 10^{-6} \cdot (6260) + 0.815 = 0.801979$$
$$\frac{\overline{Nu}_D}{Nu_{D,fd}} = 1 + \frac{a}{(X/D)^b} = 1 + \frac{3.21232}{(.2032m/.02493m)^{0.801979}} = 1.59711$$

which indicates that had this correction been made, by assuming fully developed flow the correlation would of miscalculated the transfer rates on the order of 60%. By combining

Equations 24, 25, and 27, general expressions for the Nusselt number and the Sherwood number can be obtained.

5.1.5 Heat and Mass Transfer Areas

In the above equations, separate values for heat and mass transfer areas were used. This is due to the fact that the STE material does not cover the entire area of each individual STE module. The thermal wetted perimeter and area were calculated using W_1 and L_1 while the mass transfer perimeter and area was calculated using W_2 and L_2 as shown below in Figure 5.3.

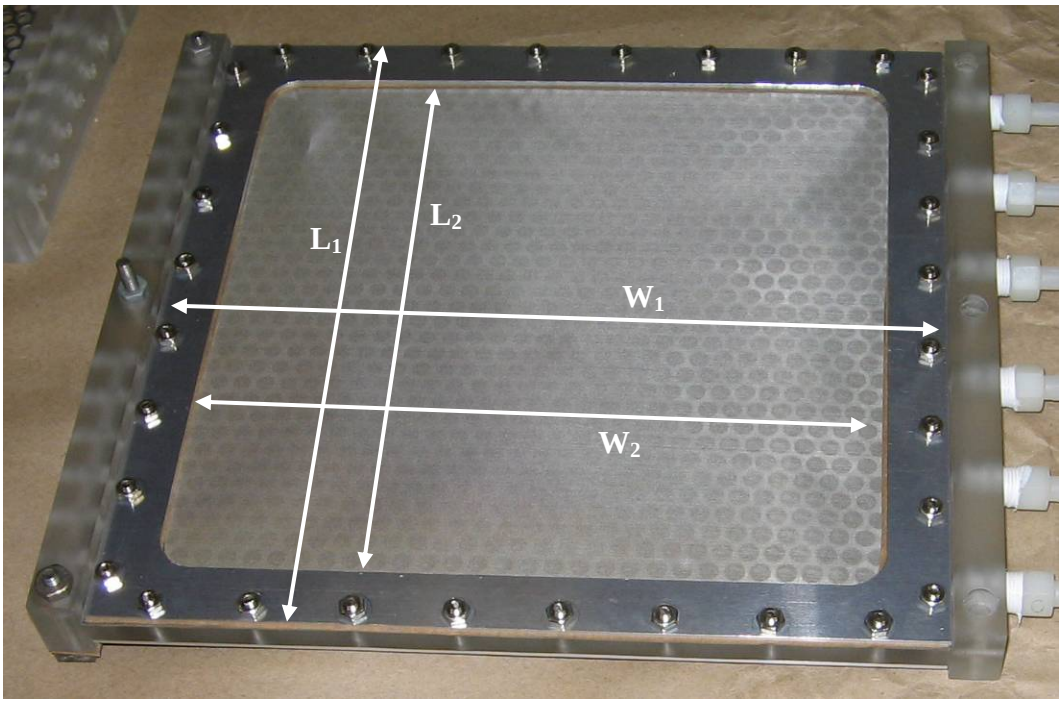

Figure 5.3 Dimensions of Thermal and Mass Transfer Geometries

The actual values for the perimeters and areas, taking into account that there are a total of 8 surfaces for the entire STE assembly, are:

$$L_1 = 8in = .2032m$$
$$L_2 = 7in = .1778m$$
$$W_1 = 8.394in = .213208m$$
$$W_2 = 7.394in = .187808m$$
$$P_{thermal} = 8 \cdot W_1 = 1.70566m$$
$$A_{thermal} = 8 \cdot W_1 \cdot L_1 = .346591m^2$$
$$P_{mass} = 8 \cdot W_2 = 1.50246m$$
$$A_{mass} = 8 \cdot W_2 \cdot L_2 = .267138m^2$$

5.1.6 Calculating the Water Vapor Concentration at the STE Surface

A good starting point is to begin with the Young-Laplace equation, Equation 4, for a liquid droplet in vapor (see Figure 5.4):

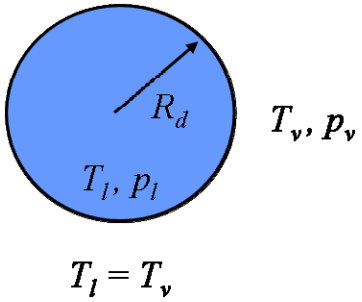

Figure 5.4 Liquid Droplet

If Equation 4 is differentiated, we obtain:

$$dp_l - dp_v = -\frac{2\sigma}{R_d^2} dR_d \qquad \textbf{Equation 30}$$

At phase equilibrium, the Gibbs free energy functions must be equal for the liquid and vapor phases (Faghri, 2006). By taking advantage of the fact that the temperature is constant through phase change, the following equation may be obtained:

$$v_l dp_l = v_v dp_v \qquad \textbf{Equation 31}$$

By combining Equations 30 and 31, the following equation is obtained:

$$v_l \left(dp_v - \frac{2\sigma}{R_d^2} dR_d \right) = v_v dp_v \qquad \textbf{Equation 32}$$

If the ideal gas law is then assumed for the vapor phase:

$$v_l p_v \left(dp_v - \frac{2\sigma}{R_d^2} dR_d \right) = R_g T dp_v \qquad \textbf{Equation 33}$$

By integrating Equation 33 from a flat surface to a give radius R_d, the following results:

$$p_v = p_{sat}(T) \exp\left(\frac{v_l \left(p_v - p_{sat}(T) + \frac{2\sigma}{R_d} \right)}{R_g T} \right) \qquad \textbf{Equation 34}$$

If we apply Equation 34 to the case of a water droplet suspended in moist air, then the partial pressure of the water vapor may be solved for given a pressure difference between the moist air mixture and liquid droplet. If we apply the above equation to the STE interfacial area,

we observe several differences. If the STE's interior is at negative gauge pressure, the curvature of the liquid-vapor interface is negative (as defined above in the derivation of Equation 24. For example, if the liquid water temperature is $40^{o}C$, then the following properties apply:

$$p_{sat} = 7417.2\frac{N}{m^2}$$

$$v_l = .0010078\frac{m^3}{kg}$$

$$\sigma = 0.069597\frac{N}{m}$$

The surface tension contribution to Equation 34 can also be replaced by noting that this contribution is solely a function of the liquid pressure minus the total gas pressure:

$$p_v = p_{sat}(T)\exp\left(\frac{v_l\left(p_v - p_{sat}(T) + \frac{2\sigma}{R_d}\right)}{R_g T}\right) = p_{sat}(T)\exp\left(\frac{v_l\left(p_v - p_{sat}(T) + \left(p_l - p_{air}\right)\right)}{R_g T}\right)$$

This equation can now be iteratively solved for the water vapor partial pressure at the interface. Figure 5.5 shows this relationship graphically for the above saturation pressure, specific volume, and surface tension properties of liquid water. The right plot shows how capillary radius also impacts the vapor pressure.

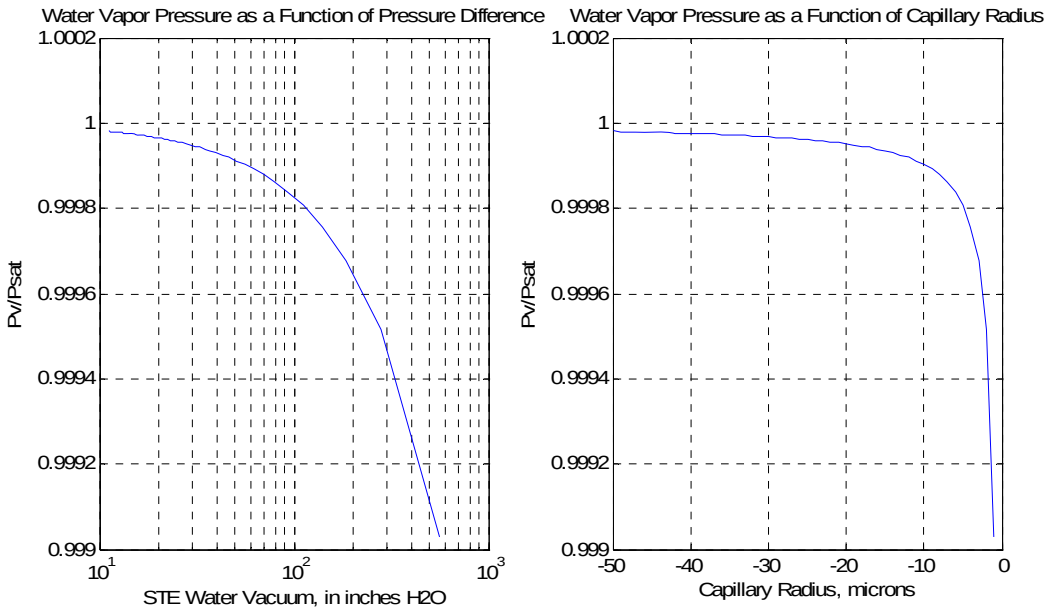

Figure 5.5 Capillary Effects on Water Vapor Pressure

As can be seen from the plots, capillary effects do not appreciably affect the water vapor pressure, and hence the water vapor concentration, at the STE's surface. For this reason, these effects have not been incorporated into the model, and the partial pressure of the water vapor at the surface of the STE is calculated as:

$$p_v = p_{sat}(T) \qquad \textbf{Equation 35}$$

5.1.7 Moist Air Property Calculations

The properties of the drying fluid proved to be a challenge to model in an algorithm due to the humidity of mixture. Using the ideal gas law, thermodynamic properties were relatively easy to solve for, but the transport properties such as dynamic viscosity, thermal diffusivity, binary diffusion coefficient, the Schmidt number, and the Prandtl number proved to be much more difficult. Thermophysical models of the moist air mixture were adapted from the models used in the psychrometric software package *WinPsychro* developed by M. Conde Engineering (M. Conde Engineering, 2007), as well as models from the 2001 ASHRAE Fundamentals Handbook, (ASHRAE, 2001). All formulas stated in this section may are taken from the above references, thus no references are made for each specific equation.

The mole fractions of the mixture are defined in terms of the humidity ratio, ω, in kg H_2O per kg Dry Air:

$$X_{air} = \frac{1}{1+1.607793\omega}$$
$$X_{water} = \frac{\omega}{0.62197058+\omega}$$

Equation 36

The mixture molecular weight was calculated via:

$$M_{mixture} = X_{air} \cdot M_{air} + X_{water} \cdot M_{water}$$

Equation 37

where the molecular weights of dry air and water are:

$$M_{air} = 28.9645 \frac{kg}{kmol}$$
$$M_{water} = 18.016 \frac{kg}{kmol}$$

The specific volume of the mixture is calculated using the ideal gas assumption:

$$v = \frac{R_{mixture} T}{p} = \frac{R_{universal}}{M_{mixture}} \frac{T}{p}$$

where $R_{mixture}$ is the gas constant for the mixture, T is the dry-bulb temperature in Kelvin, and p is the total pressure in kPa.

Thermal conductivity and dynamic viscosity of moist air can be calculated by the following equation:

$$P_{x,m} = \frac{P_{x,i}}{1+G_{i,j}\frac{X_j}{X_i}} + \frac{P_{x,j}}{1+G_{j,i}\frac{X_i}{X_j}}$$

Equation 38

where $P_{x,y}$ is the general property x of component y with m being the total mixture, X_y is the mole fraction of component y, and $G_{i,j}$ and $G_{j,i}$ are functions of the viscosity of components i and j as defined by:

$$G_{i.,j} = 0.277609\left[1+1.12605\left(\frac{\mu_i}{\mu_j}\right)^{1/2}\right]^2$$

Equation 39

where μ_y is the dynamic viscosities of the component y (adapted for air and water vapor mixture).

The viscosities of the each component can be approximated using the following formula:

$$P_x = \sum_{i=0}^{2} \xi_i T^i \qquad \textbf{Equation 40}$$

where T is the mixture dry-bulb temperature in Kelvin and the coefficients are:

Table 5.1 Coefficients for Equation 40

i	Water Vapor		Dry Air	
	ξ_λ	ξ_μ	ξ_λ	μ
0	-0.35376×10^{-2}	-0.97494×10^{-6}	0.669881×10^{-3}	0.143387×10^{-5}
1	0.654755×10^{-4}	0.359061×10^{-7}	0.942482×10^{-4}	0.656244×10^{-7}
2	0.174460×10^{-7}	0.241612×10^{-12}	-0.327450×10^{-7}	-0.29905×10^{-10}

where λ is the thermal conductivity coefficient and μ is the dynamic viscosity coefficient.

The units of Equation 38 for thermal conductivity are $\frac{W}{m \cdot K}$ and for viscosity are $\frac{N \cdot s}{m^2}$.

The diffusivity of water vapor in air is calculated via:

$$D\left[\frac{m^2}{s}\right] = 104.91143 \cdot 10^{-6} \frac{T^{1.774}}{p} \qquad \left(253.15K \le T \le 353.15K\right) \qquad \textbf{Equation 41}$$

$$D\left[\frac{m^2}{s}\right] = \frac{805.2375 \cdot 10^{-6}}{p} \frac{T^{5/2}}{T + 190} \qquad \left(353.15K \le T \le 573.15K\right)$$

Where p is the mixture total pressure in pascals, Pa.

The specific heat in $\frac{kJ}{kg \cdot K}$ at constant pressure of the mixture is determined by the following equation:

$$Cp = mf_{air} \cdot Cp_{air} + mf_{water} \cdot Cp_{water} \qquad \textbf{Equation 42}$$

where mf_y is the mass fraction of component y and Cp_{air} is calculated via:

$$Cp_{\text{air}} = \frac{1.9327 \cdot 10^{-10} \cdot \mathrm{T}^4 - 7.9999 \cdot 10^{-7} \cdot T^3 + 1.1407 \cdot 10^{-3} \cdot \mathrm{T}^2 - 0.4489 \cdot \mathrm{T} + 1057.5}{1000} \qquad \textbf{Equation 43}$$

and Cp_{water} is calculated via:

$$Cp_{water} = \frac{8.314}{18.02} \cdot \begin{pmatrix} 4.07 - 1.108 \cdot 10^{-3} \cdot T + 4.152 \cdot 10^{-6} \cdot T^2 - 2.964 \cdot 10^{-9} \cdot T^3 \ldots \\ + 0.807 \cdot 10^{-12} \cdot T^4 \end{pmatrix} \qquad \textbf{Equation 44}$$

The kinematic viscosity in $\frac{m^2}{s}$ is calculated from its definition:

$$\nu_{kinematic} = \frac{\mu}{v} \qquad \textbf{Equation 45}$$

The thermal diffusivity in $\frac{m^2}{s}$ is calculated from its definition:

$$\alpha = \frac{k \cdot v}{Cp \cdot 1000} \qquad \textbf{Equation 46}$$

The Prandtl number is calculated from its definition:

$$\mathrm{Pr} = \frac{\nu_{kinematic}}{\alpha} \qquad \textbf{Equation 47}$$

The Schmidt number is calculated from its definition:

$$Sc = \frac{\mu \cdot v}{D} \qquad \textbf{Equation 48}$$

5.1.8 Liquid Water Property Calculations

Saturated liquid water properties at various temperature increments were calculated using a polynomial correlation that was fitted to readily available property table data. The following equations were used for the important water properties in terms of the water temperature, in degrees Celsius.

$$\rho_w = -1.0362 \cdot 10^{-7} \cdot T^4 + 3.6196 \cdot 10^{3} \cdot T^3 - 7.1802 \cdot 10^{-3} \cdot T^2 + 4.4255 \cdot 10^{-2} \cdot T \ldots + 9.9993 \cdot 10^{2} \qquad \textbf{Equation 49}$$

$$\mu_w = 4.0724 \cdot 10^{-15} \cdot \mathrm{T}^6 - 1.5965 \cdot 10^{-12} \mathrm{T}^5 + 2.6307 \cdot 10^{-10} \cdot \mathrm{T}^4 - 2.4281 \cdot 10^{-8} \cdot \mathrm{T}^3 \ldots + 1.4378 \cdot 10^{-6} \cdot \mathrm{T}^2 - 6.0171 \cdot 10^{-5} \cdot \mathrm{T} + 1.7869 \cdot 10^{-3} \qquad \textbf{Equation 50}$$

$$psat_w = 9.6495 \cdot 10^{-4} \cdot \mathrm{T}^4 - 3.3243 \cdot 10^{-2} \cdot \mathrm{T}^3 + 3.5535 \cdot \mathrm{T}^2 + 18.204 \cdot \mathrm{T} + 6.6075 \cdot 10^{2} \qquad \textbf{Equation 51}$$

$$\sigma_w = 1.5436 \cdot 10^{-9} \cdot \mathrm{T}^3 - 4.9801 \cdot 10^{-7} \cdot \mathrm{T}^2 - 1.3237 \cdot 10^{-4} \cdot \mathrm{T} + 7.5590 \cdot 10^{-2} \qquad \textbf{Equation 52}$$

$$\mathrm{Pr}_w = -5.7915 \cdot 10^{-12} \mathrm{T}^6 - 3.4783 \cdot 10^{-10} \cdot \mathrm{T}^5 + 5.5841 \cdot 10^{-7} \cdot \mathrm{T}^4 - 1.0156 \cdot 10^{-4} \mathrm{T}^3 \ldots + 8.7612 \cdot 10^{-3} \cdot \mathrm{T}^2 - 4.3874 \cdot 10^{-1} \mathrm{T} + 13.008 \qquad \textbf{Equation 53}$$

$$\kappa_w = -7.1184 \cdot 10^{-6} \mathrm{T}^2 + 1.8347 \cdot 10^{-3} \mathrm{T} + 5.6806 \cdot 10^{-1} \qquad \textbf{Equation 54}$$

$$h_{fg} = -1.3911 \cdot 10^{-3} \cdot \mathrm{T}^2 - 2.2958 \cdot \mathrm{T} + 2.5010 \cdot 10^{3} \qquad \textbf{Equation 55}$$

The following table, Table 5.2, shows the units of each of the above quantities as well as how well the above polynomials fit according to their R^2 values.

Table 5.2 Property Correlation Specifics for Sat. Liquid Water

Property	Units	R^2
Density, ρ	kg / m^2	1.0000E+00
Dynamic Viscosity, μ	$(N s) / m^2$	1.0000E+00
Sat. Pressure, *psat*	$k Pa$	1.0000E+00
Surface Tension, σ	N / m	9.9999E-01
Prandtl Number, Pr	*Dimensionless*	9.9999E-01
Thermal Conductivity, κ	$W / (m^2 K)$	9.9969E-01
Heat of Vaporization, h_{fg}	kJ / kg	9.9999E-01

5.1.9 Model Implementation

The model was not able to be coded into a single programming language due to the difficulty of requiring a simultaneous non-linear equation solver and program function calling capabilities to be incorporated within one software program. For this reason, two separate software programs were used. This resulted in the model only being able to be solved for discrete points rather feeding data through a script for massive analyses. Solving the model was accomplished using MATLAB version 7.1 (R14) for scripting and function calling capabilities and MathCAD 2000 Professional for its simultaneous equation.

MATLAB was used to create a program that was responsible for calculating flow characterization variables, heat and mass transfer coefficients, water properties, and moist air properties. The basic outline of the main function, *STE.m*, is described by the following pseudo code:

1. Initialize STE Variable Geometry
2. Call Drying Fluid Properties Function
    a. Calculate Fluid Properties and Return to Main Function
3. Characterize Drying Fluid Flow
4. Calculate Entry Length Correction Factors
5. Calculate Nusselt and Sherwood Numbers
6. Calculate Heat and Mass Transfer Coefficients
7. Call Water Properties Function
    a. Calculate Water Fluid Properties and Return to Main Function

The fluid properties function, *Properties3.m*, calculates all pertinent moist air fluid properties and *H2O_Properties_1.m* calculates all the important water properties to this analysis. These files are all documented in Appendix C.

MathCAD was used to solve the system of equations described above. In certain cases, the model would solve for an exit relative humidity of slightly over 100%. In this case, the model was manually constrained to solutions at or below 100% relative humidity. The MathCAD model is also documented in Appendix C.

5.2 Model Results

The model was first tested by exploring the dependency of the predicted heat and mass fluxes based on drying fluid flow rate, drying fluid inlet temperature, STE water flow rate, and STE water inlet temperature. These cases all had a single point in common to provide reference between the results. This central point was set to be the following as shown in Table 5.3:

Table 5.3 Base Case for Model Variable Exploration

Variable	Description	Units	Nominal Value
T_{in}	Air temperature at inlet	$°C$	55
P_{in}	Air pressure at inlet	kPa	101.574
ω_{in}	Air humidity ratio at inlet	$kg\ H_2O\ /\ kg\ Dry\ Air$	0.090
T_{w_in}	Water temperature at inlet	$°C$	30
P_{w_in}	Water pressure at inlet	kPa	101.325
Q_{in}	Air volumetric flow rate	m^3/s	0.05417
Q_{w_in}	Water volumetric flow rate	m^3/s	$7.566*10^{-5}$

The four variables were incremented holding all other parameters constant (except for the case where relative humidity is held constant) accordingly:

Table 5.4 Model Variable Exploration Sweep Ranges

Model Inputs

		Actual Inputs						Calculated Inputs		
Test Type	Test #	T_{air}	P_{air}	W_{in}	Q_{in}	Tw_in	Q_{w_in}	RH1	$mdot_{air}$	$mdot_{water}$
		°C	kPa	kg H2O / kg Dry Air	m^3/s	°C	m^3/s	%	kg/s	kg/s
Base	1	55	101.574	0.09	0.05417	30	7.566E-05	0.815	5.562E-02	7.534E-02
Tw_in Sweep	2	55	101.574	0.09	0.05417	20	7.566E-05	0.815	5.562E-02	7.553E-02
Tw_in Sweep	3	55	101.574	0.09	0.05417	25	7.566E-05	0.815	5.562E-02	7.544E-02
Tw_in Sweep	5	55	101.574	0.09	0.05417	35	7.566E-05	0.815	5.562E-02	7.521E-02
Tw_in Sweep	6	55	101.574	0.09	0.05417	40	7.566E-05	0.815	5.562E-02	7.508E-02
Water Flow Sweep	7	55	101.574	0.09	0.05417	30	6.500E-05	0.815	5.562E-02	6.472E-02
Water Flow Sweep	8	55	101.574	0.09	0.05417	30	7.000E-05	0.815	5.562E-02	6.970E-02
Water Flow Sweep	10	55	101.574	0.09	0.05417	30	8.000E-05	0.815	5.562E-02	7.966E-02
Water Flow Sweep	11	55	101.574	0.09	0.05417	30	8.500E-05	0.815	5.562E-02	8.463E-02
T_{air} Sweep (Constant ω)	12	51	101.574	0.09	0.05417	30	7.566E-05	0.99	5.631E-02	7.534E-02
T_{air} Sweep (Constant ω)	13	53	101.574	0.09	0.05417	30	7.566E-05	0.897	5.596E-02	7.534E-02
T_{air} Sweep (Constant ω)	15	57	101.574	0.09	0.05417	30	7.566E-05	0.741	5.528E-02	7.534E-02
T_{air} Sweep (Constant ω)	16	59	101.574	0.09	0.05417	30	7.566E-05	0.674	5.495E-02	7.534E-02
Air Flow Sweep	17	55	101.574	0.09	0.04500	30	7.566E-05	0.815	4.621E-02	7.534E-02
Air Flow Sweep	18	55	101.574	0.09	0.05000	30	7.566E-05	0.815	5.134E-02	7.534E-02
Air Flow Sweep	20	55	101.574	0.09	0.06000	30	7.566E-05	0.815	6.161E-02	7.534E-02
Air Flow Sweep	21	55	101.574	0.09	0.06500	30	7.566E-05	0.815	6.674E-02	7.534E-02
T_{air} Sweep (Constant RH)	22	51	101.574	0.0723	0.05417	30	7.566E-05	0.815	5.680E-02	7.534E-02
T_{air} Sweep (Constant RH)	23	53	101.574	0.0807	0.05417	30	7.566E-05	0.815	5.622E-02	7.534E-02
T_{air} Sweep (Constant RH)	24	57	101.574	0.1005	0.05417	30	7.566E-05	0.815	5.500E-02	7.534E-02
T_{air} Sweep (Constant RH)	25	59	101.574	0.1121	0.05417	30	7.566E-05	0.815	5.438E-02	7.534E-02

These cases were all solved for and are displayed in graphical form in the following charts (Figure 5.6, Figure 5.7, Figure 5.8, Figure 5.9, and Figure 5.10).

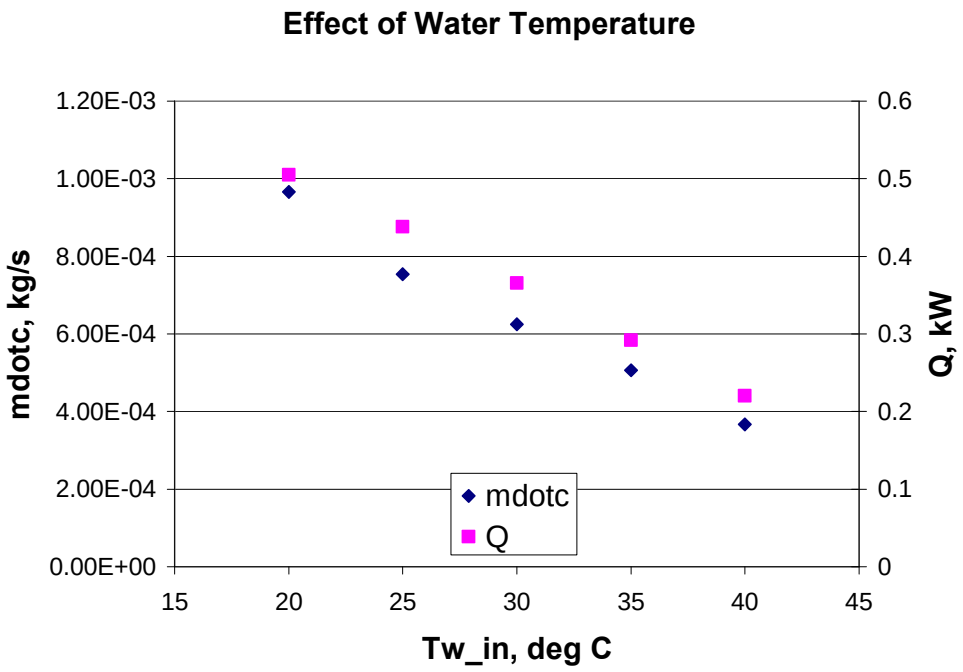

Figure 5.6 Variable Exploration: Water Temperature Sweep

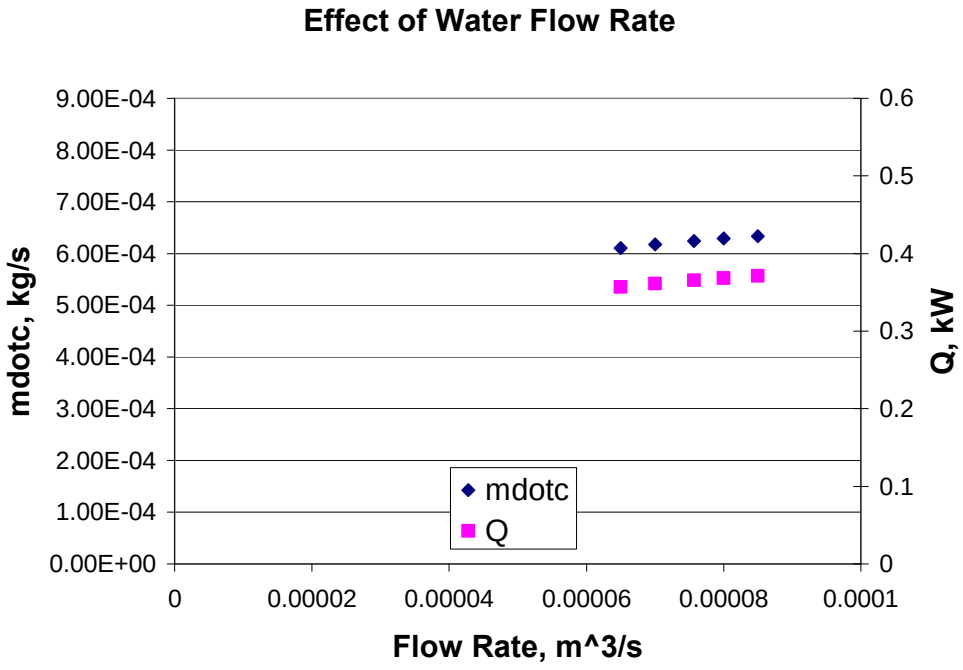

Figure 5.7 Variable Exploration: Water Flow Rate Sweep

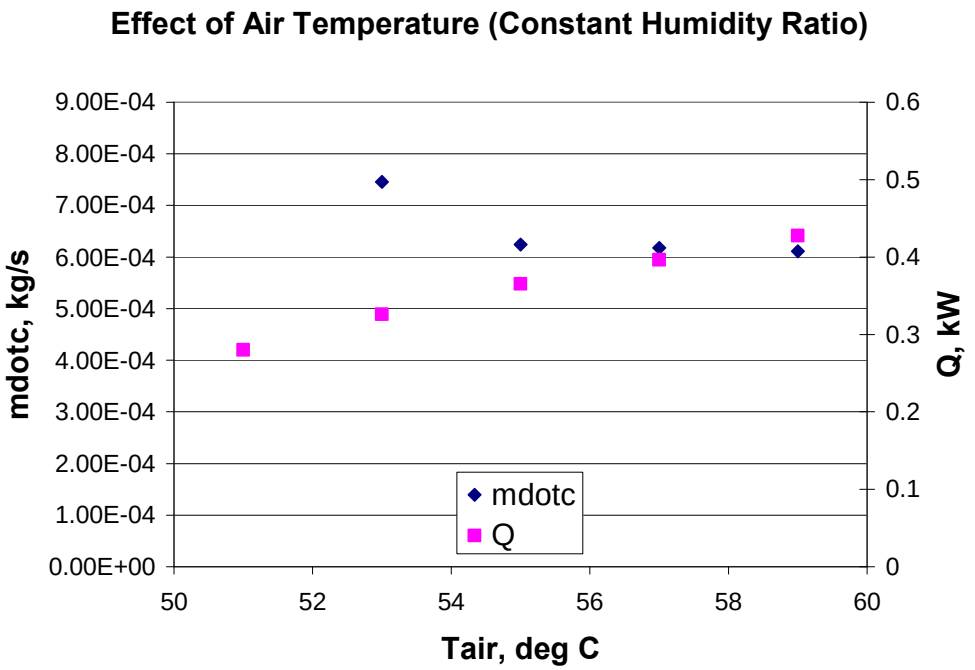

Figure 5.8 Variable Exploration: Air Temperature Sweep

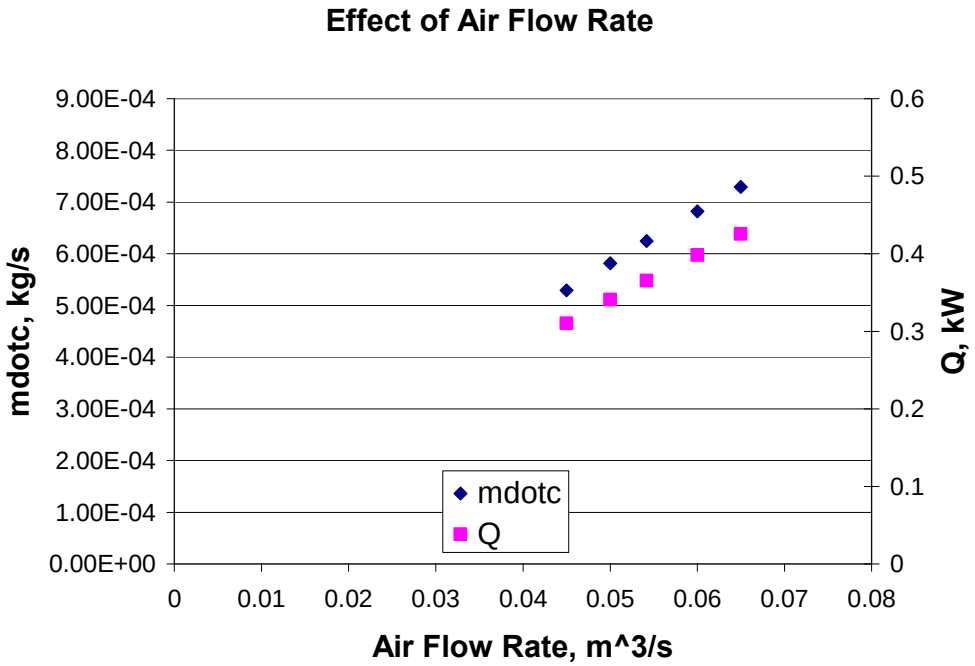

Figure 5.9 Variable Exploration: Air Flow Rate Sweep

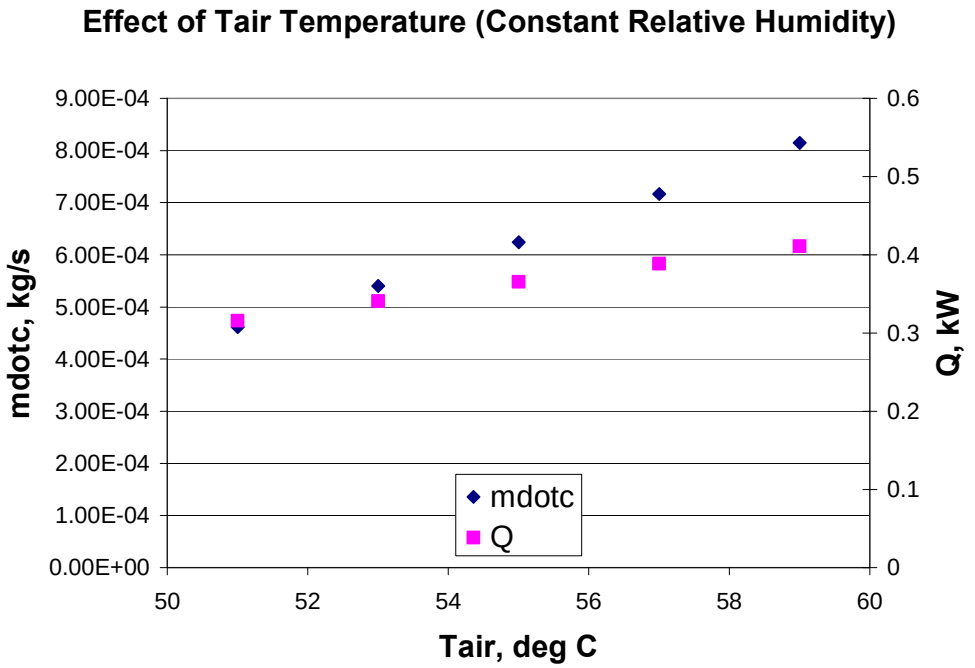

Figure 5.10 Variable Exploration: Air Temperature Sweep

It can be seen from Figure 5.6, that as water temperature increases, the humidity removal rate from the drying fluid decreases as well as the heat transfer decreases. In Figure 5.7, we see that the water flow rate has very little effect on the humidity removal rate and heat transfer. Figure 5.8, as the drying fluid temperature increases at constant humidity ratio, the humidity removal rate decreases while the heat transfer increases – this is a little odd since generally heat and mass transfer are coupled phenomena. This can be explained as the concentration gradient diminishing as air temperature increases at constant humidity ratio. If the *relative humidity* is held constant and the air temperature is increased, we see the behavior shown in Figure 5.10. It is this relative humidity that more directly effects the humidity removal rate than the humidity ratio. Figure 5.9 shows how increasing the air flow rate increases the heat and mass transfer.

CHAPTER 6 - Experimental Results

6.1 Analytical Model Verification

It was of interest to compare the analytical model predicted operation to the actual STE's operation. The dryer has five different operating periods during each drying cycle: the preheat (shown as red), the stabilization (shown as yellow), the high-temperature cycle (shown as green), the low-temperature cycle (shown as blue), and the cool-down (shown as grey). Each of these regions have different characteristics and are shown in Figure 6.1.

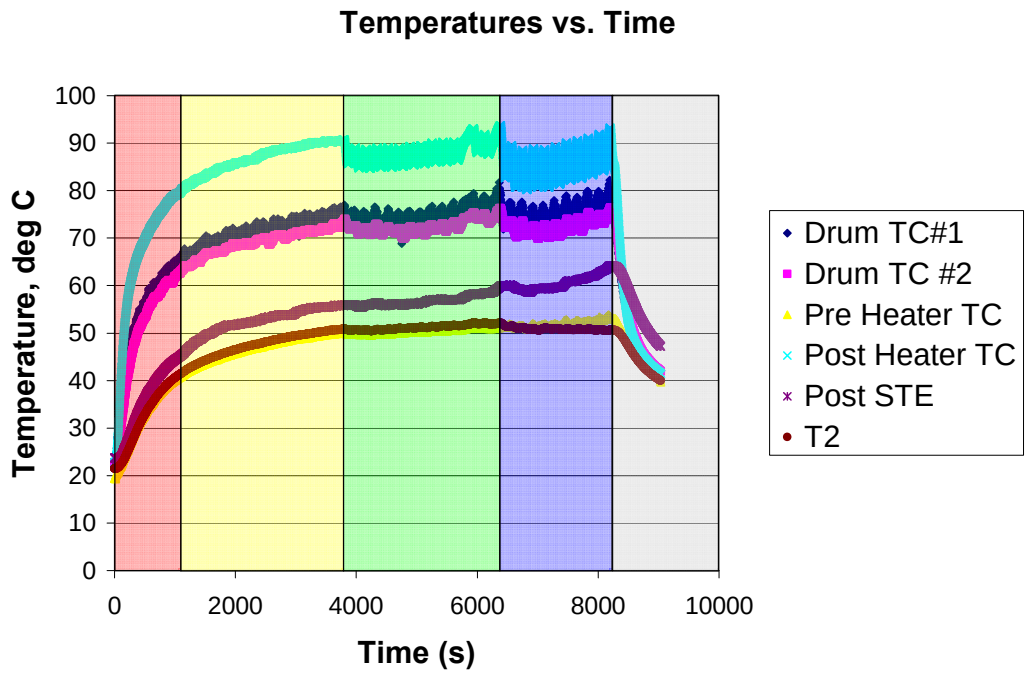

Figure 6.1 Drying Cycle Operating Periods

For each period, three points in time were selected to compare the analytical model with the STE. To accomplish this, the state of the drying fluid and water entering the STE, as well as their respective flow rates at each were feed into the model for one point in time. The model then predicted the output drying fluid and water states, moisture removal rate, and heat transfer rate. Data for the comparison was taken from a single test (STEMOD3.xls). Figure 6.2 shows how the predicted drying fluid temperatures compare with the actual temperatures. In the plot, the brown line represents the temperature of the drying fluid in the drying drum, the blue and red

lines represent the temperature entering and exiting the STE, the blue diamonds and red squares are the discrete data points that were extracted from the data set for comparison analysis, and finally, the green boxes represent the predicted exiting temperature. Thus, if the model perfectly predicts the exiting conditions, the green boxes should fall directly on top of the red ones.

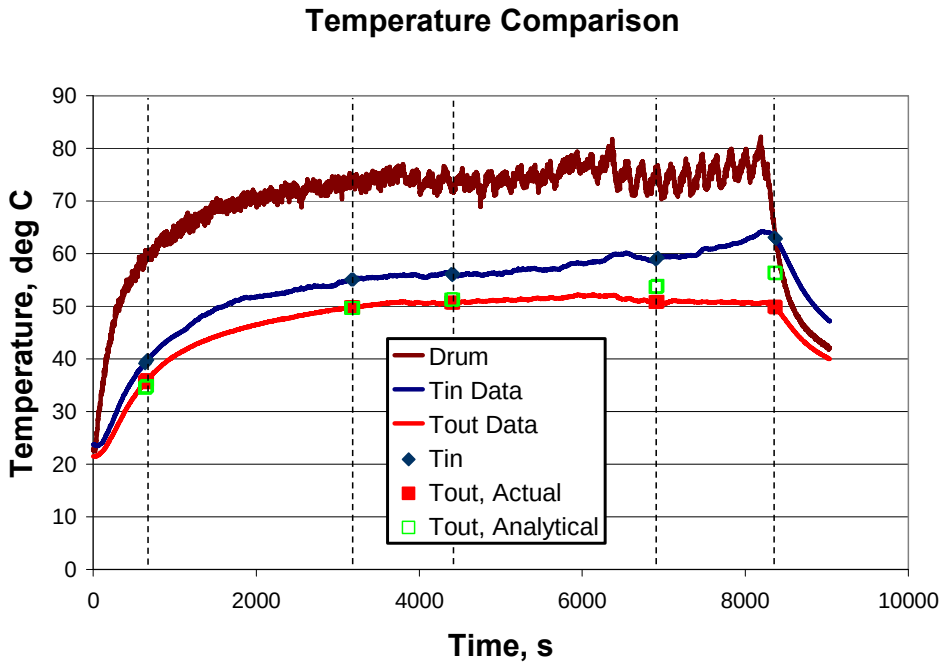

Figure 6.2 Model Verification for Temperature

Similarly, Figure 6.3 shows how the predicted drying fluid humidity ratios compare with the actual humidity ratios. In the plot, the blue and red lines represent the humidity ratios entering and exiting the STE, the blue diamonds and red squares are the discrete data points that were extracted from the data set for comparison analysis, and finally, the green boxes represent the predicted exiting humidity ratio. Thus, the green boxes should fall on the red ones should the model be operating perfectly.

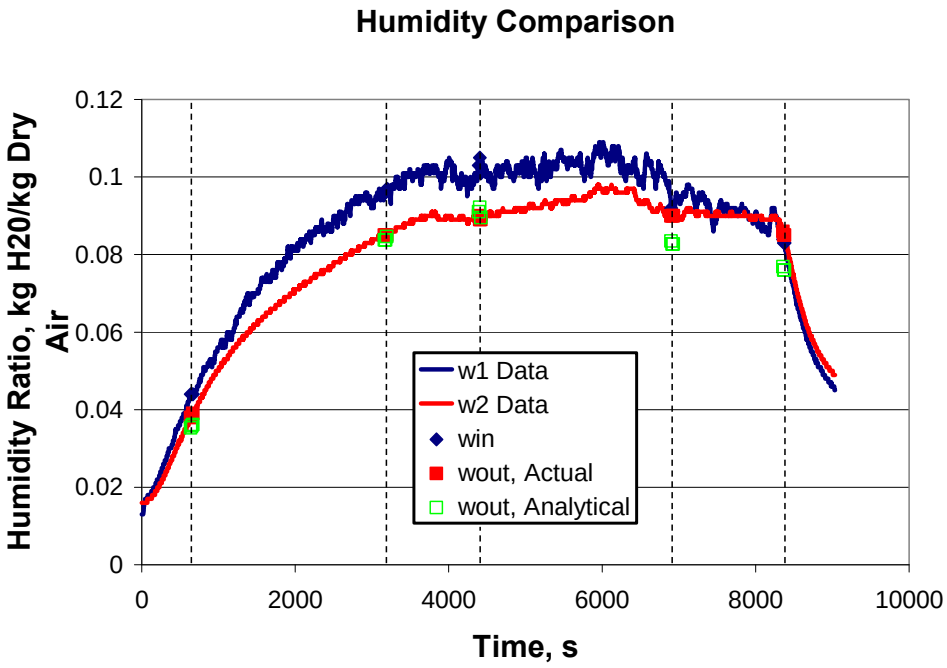

Figure 6.3 Model Verification for Humidity Ratio

A calculation was also performed with the existing data to calculate the actual moisture removal rate. This calculated rate was then compared with the model's predicted rate as shown in Figure 6.4. Just as in the previous plots, the green boxes should fall on the red ones if the model is working perfectly.

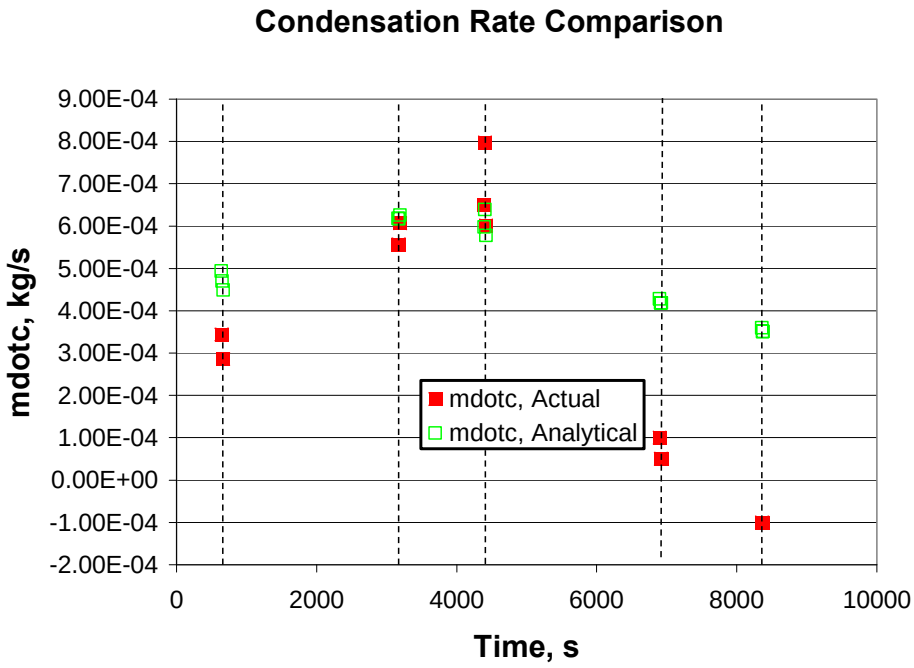

Figure 6.4 Model Verification for Condensation Rate

As one can see, the model very closely predicts the exiting conditions in the first three drying periods but deviates during the last two periods. One possible explanation for this is that during the last two periods, the dryer's control algorithm is causing the temperatures to fluctuate much more than in the previous periods. This transient behavior may be causing temperature and humidity sensors to not be as accurate, and cause the steady-state assumption for the model not be as realistic as in the first three cases.

6.2 Presentation of Condenser vs. STE Results

6.2.1 Operational Comparison

Many things about how the dryer operates were learned by simply watching how temperature, humidity, and power usage fluctuated during the tests. Upon comparing the data of each type of test, several differences in dryer operation were observed. The first is that when the condenser is used, the temperatures in general tend to be higher than in the case of the STE. The temperature of the drum thermocouples are on average 10 °C cooler in the STE case than in the baseline case. This is observable through looking at the temperature versus time plot for each case shown in Figure 6.5 and Figure 6.6.

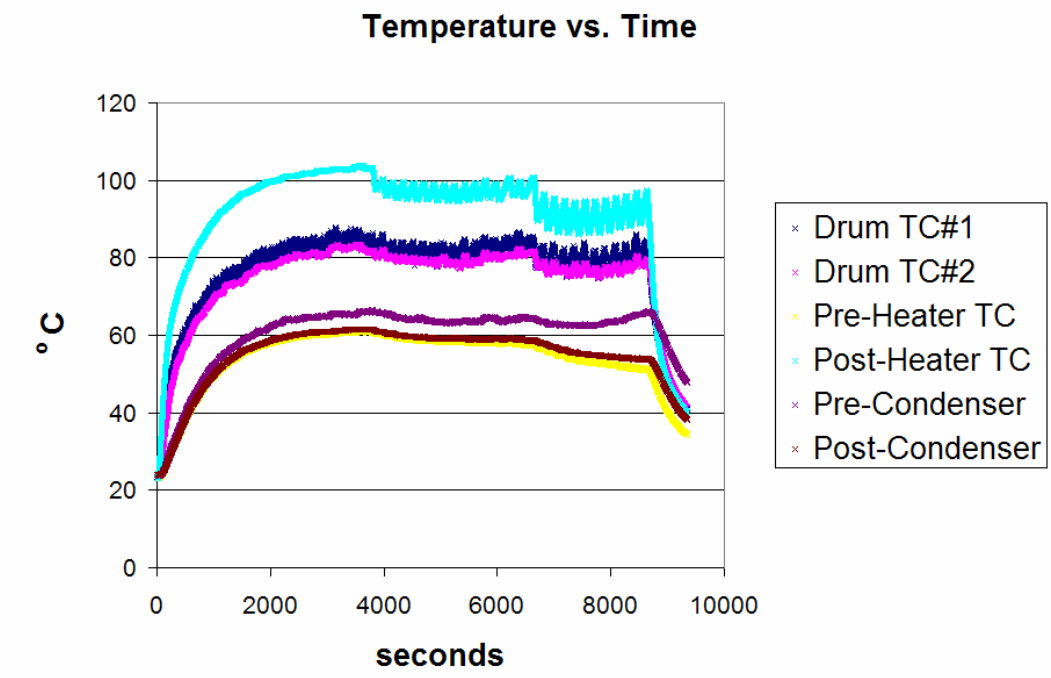

Figure 6.5 Typical Condenser Temperature Plot

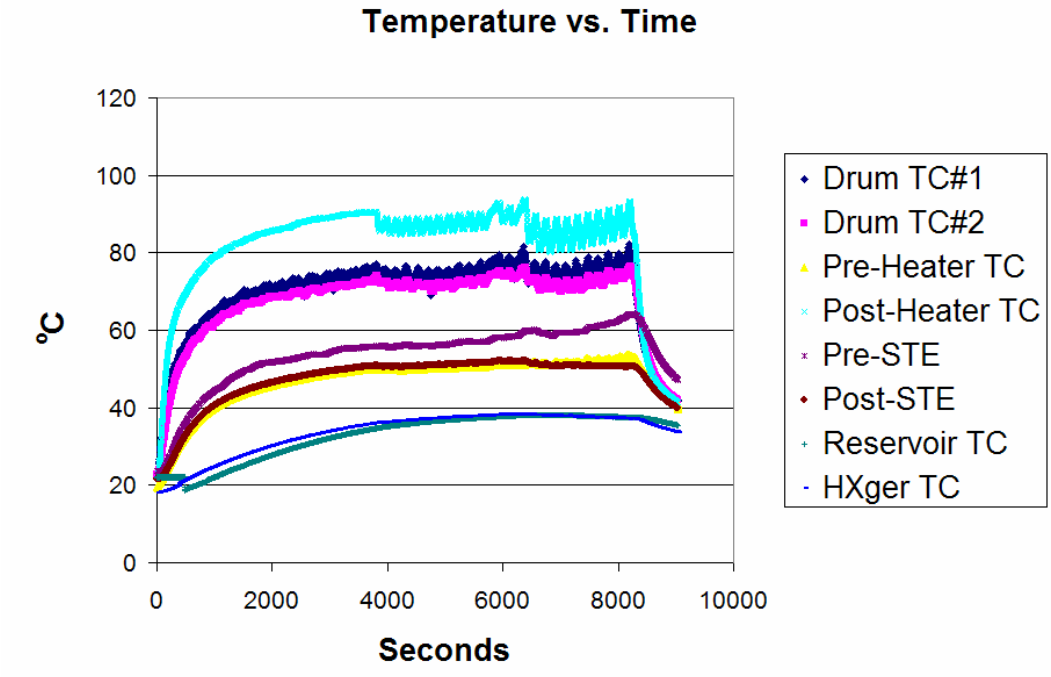

Figure 6.6 Typical STE Temperature Plot

The humidity ratios of the tests are also different, as is observable from the humidity ratio versus time plots. The difference is quite remarkable with the STE humidity ratio nearly half of condenser's ratio. Plots of this data can be seen in Figure 6.7 and Figure 6.8.

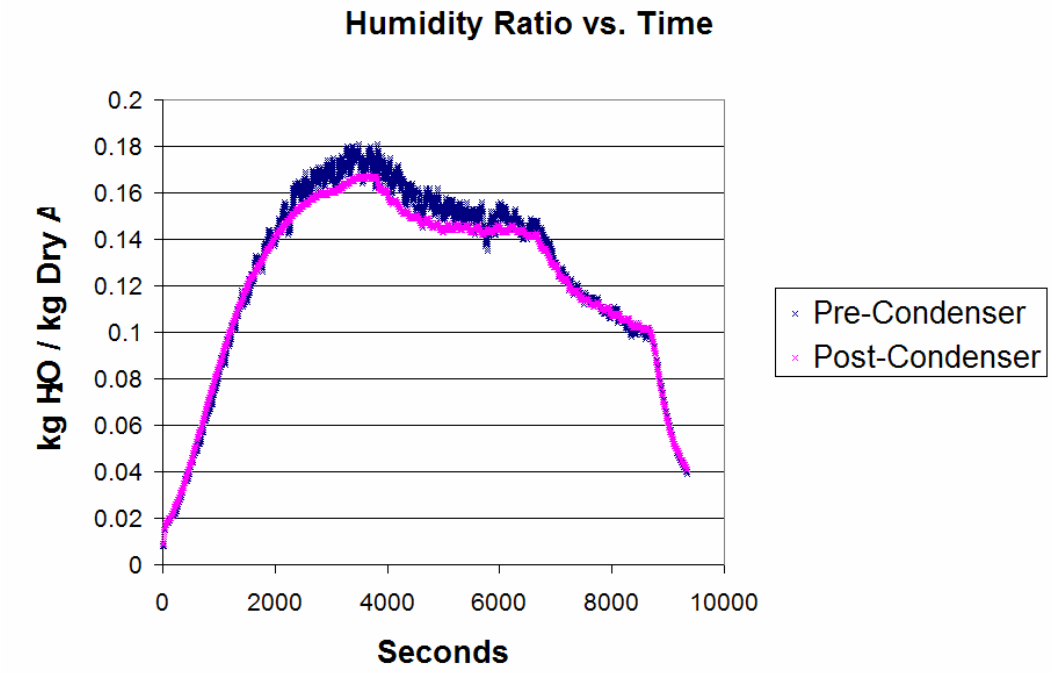

Figure 6.7 Typical Condenser Humidity Ratio Plot

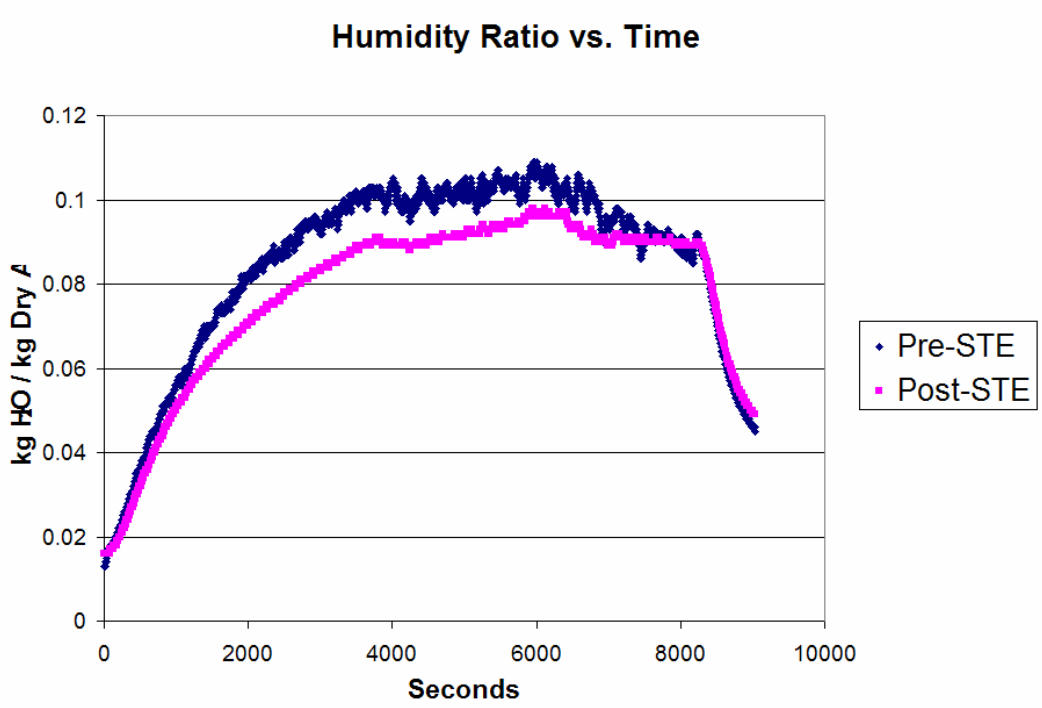

Figure 6.8 Typical STE Humidity Ratio Plot

The power usage did not change very much, but will be shown here for comparison purposes. The heater controller is an on/off relay controller, as can be seen from Figure 6.9 and Figure 6.10. The algorithm controlling the heater has four separate regions – a region where the heater is always on allowing the drum to heat up to temperature, a second where the heater cycles on and off at a high temperature, a third region where the heater cycles on and off at a lower temperature, and a final cool-down region where the heater is off. From the tests, it appears that the transition from the first to the second region is solely a function of time. The second and third transitions are not well understood as to which criteria instigate the transition. The area under the power consumption plots was integrated over time to calculate the total energy consumed.

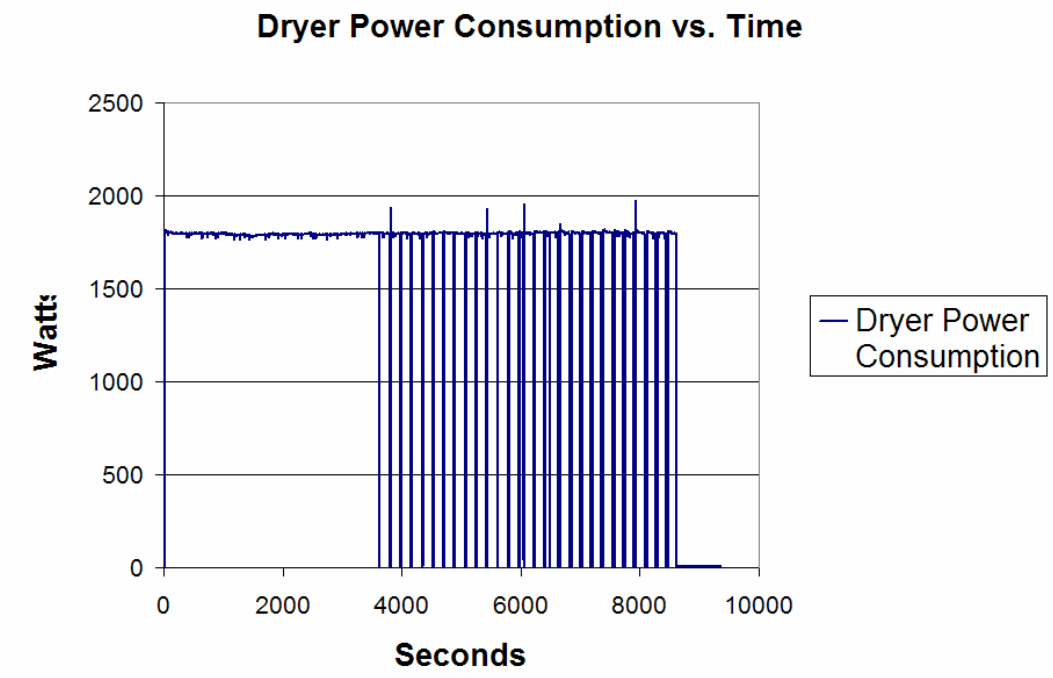

Figure 6.9 Typical Condenser Power Consumption Plot

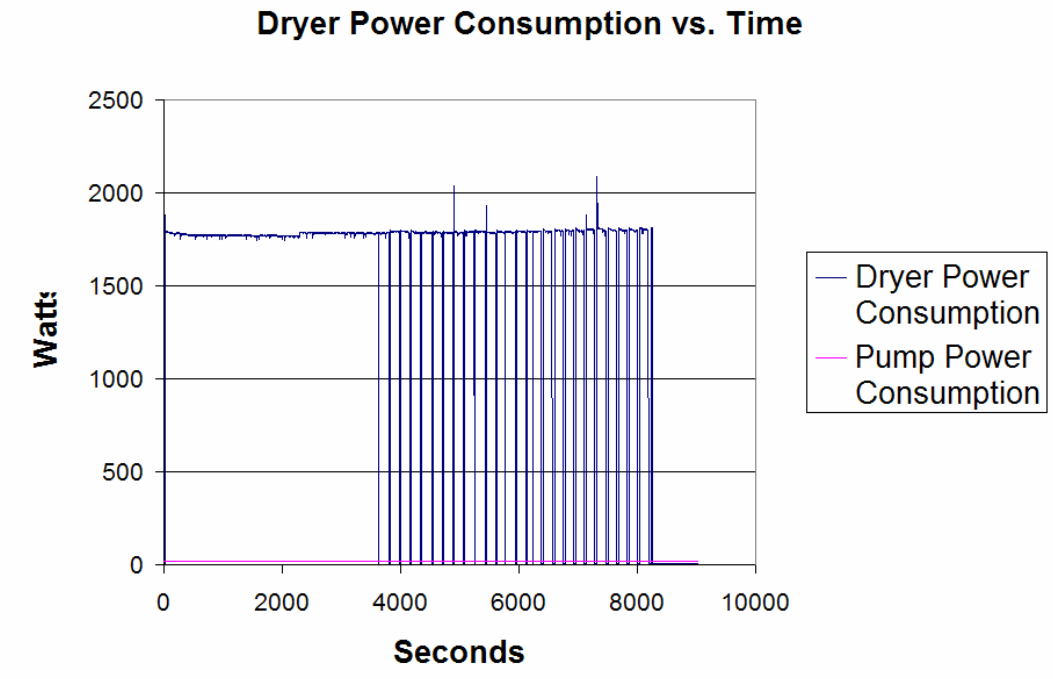

Figure 6.10 Typical STE Power Consumption Plot

6.2.2 Performance Comparison

Upon completion of each type of test, the results from each type were averaged. The parameters of key interest to this study are first and foremost the total energy consumption. Others important parameters included total drying time, final moisture content, and the energy consumed per *kg* of water removed from the textiles. These averaged results can be seen below in Table 6.1.

Table 6.1 Comparison Data

Variable	Units	Condenser Average	STE Average
Dryer Motor Rotation Speed	*RPM*	2691	2693
Pump Setting	*N/A*	*N/A*	4.5 / 10
Load Equilibrium Wt.	*kg*	6.058	6.058
Load Initial Wet Wt.	*kg*	10.061	10.002
Load Final Dry Wt.	*kg*	6.241	6.290
Water Removed	*kg*	3.820	3.713
Initial Moisture Content	*%*	66.08	65.11
Final Moisture Content	*%*	3.02	3.82
Drying Time	*hr*	2.41	2.45
Moisture Removal Rate	*kg H_2O / hr*	1.586	1.518
Total Energy Consumption	*kWh*	3.898 ± 0.007797	3.732 ± 0.007384
IEC Energy Consumption	*kWh / kg Laundry*	0.643 ± 0.001287	0.616 ± 0.001219
IEC Energy Class	*N/A*	*C*	B
Water Removal Consumption	*kWh / kg H_2O*	1.021	1.005
STE Condensate Captured	*kg*	*N/A*	3.058
Extra Condensate Collected	*kg*	3.242	0.207
Water Vapor Loss to Surroundings	*kg*	0.55	0.448
Water Vapor Percent Loss	*%*	14.49	12.09

The most important parameter in this study is the IEC Energy Consumption. According to Table 6.1, the STE's average value is lower than that of the Condenser's average. Figure 6.11 shows the spread of values measured for each type of test. From this, we can clearly see that the STE dryer achieves lower energy consumption per *kg* of laundry than the traditional Condenser dryer is capable of.

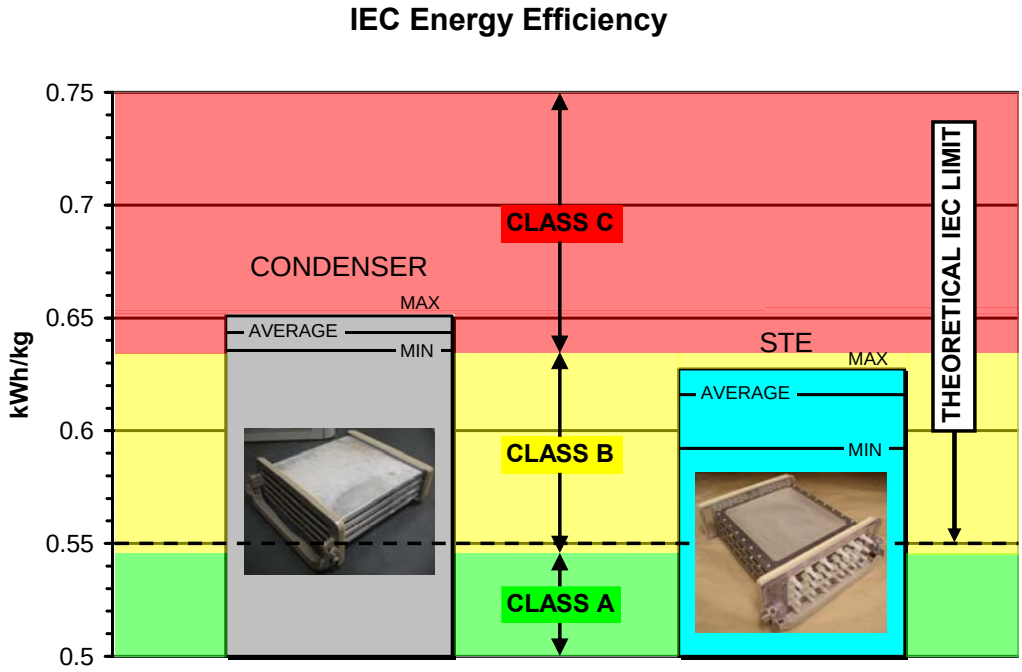

Figure 6.11 IEC Energy Efficiency Comparison

CHAPTER 7 - Conclusions

In this work, the feasibility of using a Surface Tension Element (STE) to remove moisture from a residential condensing clothes dryer was investigated. A condensing dryer was modified such that either an air-to-air heat exchanger/condenser or a STE could be installed as the primary moisture removal device for the dryer.

A STE was designed, fabricated, and bubble-point tested according to the SAE ARP901 standard. The STE consisted of four modules each having two planar STE surfaces which once assembled, had a combined surface area of 0.267 square meters. The interior of the STE was designed such that liquid water could be pumped through it, which was advantageous to applications involving humidity removal from moist air. Bubble-point testing of the STE modules indicated that a minimum of 44.5 microns, a maximum of 54.2 microns, and an average of 46.8 microns.

The operation of the dryer using the air-to-air heat exchanger/condenser designed for use with the dryer by the manufacturer was compared to the operation of the dryer using the STE. Five tests were run for each case and various measurements were taken and then averaged. Of key importance in this study was the dryer's total power consumption per kilogram of dry laundry dried. This efficiency, called IEC efficiency, was the basis of comparison between the two cases.

A simplified analytical model was developed to predict the moisture removal rate and heat transfer rate from the drying fluid as well as the drying fluid and STE water exit states. The effect of drying fluid flow rate, temperature, STE water flow rate, and STE water temperature on the moisture removal rate and heat transfer rate was also analyzed. The order of magnitude of the exit conditions is correctly predicted by the model at all times. The model reasonably predicts the exit drying fluid temperature and humidity when the dryer is operating at steady state; however, it lacks the ability to reasonably predict the exit conditions when the dryer is in the final cool-down period of the drying cycle.

The average IEC efficiency of the air-to-air heat exchanger/condenser was 0.643 kilowatt-hours per kilogram dry laundry opposed to 0.616 kWh per kg for the STE. This indicates that the STE uses less energy to dry than the air-to-air heat exchanger/condenser. This

increase in IEC efficiency causes the dryer to move from the “class C” energy class label to the “class B” energy class label, which can be very important from a marketing standpoint not to mention from an energy conservation viewpoint.

References

Abdulla, M. O., 2006, *"Drying Performance and Thermal Transient Study with Solar Radiation Supplemented by Forced-Ventilation,"* International Journal of Thermal Sciences, Vol. 45, No. 10, pp. 1027-1034.

Ameen, A., and Bari, S., 2004, *"Investigation into the effectiveness of heat pump assisted clothes dryer for humid tropics,"* Energy Conversion and Management, Vol. 45, No. 9, pp. 1397 – 1405.

ASHRAE, 2001, *"2001 ASHRAE Fundamentals Handbook,"* SI edition, American Society of Heating, Refrigerating and Air-Conditioning Engineers, Atlanta, Georgia.

Bush, E. and Nipkow, J., 2006, *"Tests and promotion of energy-efficient heat pump dryers,"* EEDAL, International Energy Efficiency in Domestic Appliances & Lighting Conference, London, UK, June.

Dahlman, T., 2006, *"Heat Pump drier – Electrolux SENSIDRY,"* EEDAL, International Energy Efficiency in Domestic Appliances & Lighting Conference, London, UK, June.

Department of Energy, Energy Information Administration, 2001, *"2001 Residential Energy Consumption Survey, End-Use Consumption of Electricity 2001*," URL: http://www.eia.doe.gov/emeu/recs/recs2001/enduse2001/enduse2001.html [cited 4 April 2007].

Department of Energy, Energy Information Administration, 2005, *"Annual Energy Review 2005,"* Report No. DOE/EIA-0384(2005), pg. 52, URL: http://www.eia.doe.gov/emeu/aer/pdf/aer.pdf [cited 4 April 2007].

Department of Energy, Office of Energy Efficiency and Renewable Energy, 1997. *"10 CFR Part 430 : Energy Conservation Program for Consumer Products: Test Procedure for Clothes Washers and Reporting Requirements for Clothes Washers, Clothes Dryers, and Dishwashers; Final Rule,"* Federal Register, Vol. 62, No. 166, Wednesday, August 27, URL: http://www.eere.energy.gov/buildings/appliance_standards/residential/pdfs/bbcl0827.pdf [cited 22 May 2007].

Faghri, A., and Zhang, Y., 2006, *"Transport Phenomena in Multiphase Systems,"* Academic Press, Elsevier, Burlington, Massachusetts.

Hamid, M., 1991, *"Microwave Drying of Clothes,"* Journal of Microwave Power and Electromagnetic Energy, Vol. 26, No. 2, pp. 107-113.

Hoehn, A., Scovazzo, P., Clawson, J., Gessinger, T., Kalinowski, W., and Pineau, J., 2003 , *"Design, Testing, and Operation of Porous Media for Dehumidification and Nutrient Delivery in Microgravity Plant Growth Systems,"* SAE – paper, 03ICES-157(155), 32nd International Conference On Environmental Systems (ICES), Vancouver, Canada, July.

Incropera, F. P., and DeWitt, D. P., 2002, *"Fundamental of Heat and Mass Transfer,"* 5th ed., Wiley, New York.

International Electrotechnical Commission, 2002, *"International Standard IEC 61121: Tumble dryers for household use – Methods for measuring the performance,"* 3rd ed.

Kowalski, S. J., 2003, *"Thermomechanics of Drying Processes,"* Lecture Notes in Applied and Computational Mechanics, Volume 8, Springer Verlag Berlin Heidelberg, New York.

M. Conde Engineering, 2007, *"Thermophysical Properties of Humid Air, Models and Background,"* URL: http://www.mrc-eng.com/Downloads/Moist%20Air%20Props%20English.pdf [cited 25 May 2007].

Market Transformation Programme, 2006, *"BNW18: EC Energy Labelling of Domestic Tumble Dryers,"* Version 1.1, URL: http://www.mtprog.com/ApprovedBriefingNotes/PDF/MTP_BNW18_2006September5.pdf [cited 4 April 2007].

Molki, M., and Sparrow, E. M., 1986, *"An Emperical Correlation for the Average Heat Transfer Coefficient in Circular Tubes,"* Journal of Heat Transfer, Vol. 108, May.

Munson, B. R., Young, D. F., and Okiishi, T. H., 2002, *"Fundamentals of Fluid Mechanics,"* 4th ed., Wiley, Hoboken, NJ.

Palandre, L., and Clodic, D., 2003, *"Comparison of Heat Pump Dryer and Mechanical Steam Compression Dryer,"* International Congress of Refridgeration 2003, Washington, D. C.

Rollins, J. R., Grove, R. K., and Jaekle, D. E. Jr. (Lockheed Missiles & Space Company, Inc., Sunnyvale, California), 1985, *"Twenty-three years of surface tension propellant management system design, development, manufacture, test, and operation,"* AIAA paper, Issue 85-1199, pg. 1-9.

Roura, P., 2005, *"Thermodynamic derivations of the mechanical equilibrium conditions for fluid surfaces: Young's and Laplace's equations,"* American Journal of Physics, Vol. 73, No. 12, December.

SAE ARP901, 2001, *"Bubble-Point Test Method,"* Rev. A, Society of Automotive Engineers.

Scovazzo, P., Illangasekare, T. H., Hoehn, A., and Todd, P., 2001, *"Modeling of two-phase flow in membranes and porous media in microgravity as applied to plant irrigation in space,"* Water Resources Research, Vol. 37, No. 5, pg. 1231-1243.

van Deventer, H. C. 1997, *"Feasibility of Energy Efficient Steam Drying of Paper and Textile Including Process Integration,"* Applied Thermal Engineering, Vol. 17, No. 8, pg. 1035-1041.

Watts, D. I., 1991, *"Evolution of the modern tumble dryer,"* GEC Review, Vol. 7, Issue 1, pg. 16-25.

Appendix A - Experimental Uncertainty

Dryer and STE Experimental Uncertainties

The sources of uncertainty in the dryer and STE water loop experimental setups are time, temperature, humidity, pressure, power, weight, and IEC efficiency measurements.

Time

Time stamps for the data were referenced from the computer's system clock, having negligible error. The data acquisition equipment first reads the system time, and then measures all signals. All these measurements are assigned the time that read at the beginning. Since the data acquisition took an average of 0.83 seconds to complete a set of measurements, therefore, the true time of each measurement may be shifted by this amount. This was not found to be a significant source of error due to the fact that the transient processes involved in drying take much longer to change than 0.83 seconds.

Temperature Measurements

There were two temperature measurement devices employed in the experimental setup. Thermocouples were used everywhere with the exception of immediately before and after the moisture removal device (condenser or STE). The thermocouples were all analyzed with the HP 34970A data acquisition unit which gives an uncertainty of:

$$u_{thermocouple} = 1^{o} C$$

The other temperature measuring device was the humidity probes. These probes, as previously described had the capability of measuring humidity and temperature simultaneously. The standard uncertainty stated by the manufacturer was:

$$u_{temp,humidity\_probe} = 0.2^{o} C$$

Humidity Measurements

Humidity measurements were made using the aforementioned humidity probes. The standard uncertainty stated by the manufacturer was:

$$u_{humidity} = 1\%RH$$

Pressure Measurements

Pressure measurements of the pressure in the moisture removal device's docking port were made using a simple u-tube type manometer with water as a working fluid. The difference in height was made using a ruler with $^1/_{16}$ inch graduations. The water was at room temperature of 23 deg C, therefore the uncertainty of these measurements was:

$$u_{height} = \frac{1}{16} inch \frac{1}{2} = \frac{1}{32} inch$$
$$u_{pressure} = \rho g u_{height} = 0.0077609 kPa$$

Power Measurements

There were two types of power measurements made – one for the dryer's power consumption and one for the STE flow loop pump's power consumption. The dryer's power consumption was measured with the AC watt transducer as described in Chapter 4. The standard uncertainty quoted by the manufacturer for the device is ± 0.2% of reading. The maximum reading the transducer is capable of is 4 *kW*, therefore the maximum standard uncertainty is:

$$u_{\text{stan}} = 8\, Watts$$

The transducer outputs a 0-10 *Volt* signal corresponding to a 0-4 *kW*, which is read by the HP 34970A data acquisition unit having a standard accuracy of ±(0.005% of reading + 0.004% of range). The data acquisition's uncertainty is therefore:

$$u_{DAQ,\text{stan}} = 0.0009V = 0.0009V \frac{4000\, Watts}{10V} = 0.36\, Watts$$

Therefore the uncertainty of the power measurement is:

$$u_{power,dryer} = \sqrt{\left(u_{\text{stan}}\right)^2 + \left(u_{DAQ,\text{stan}}\right)^2} = 8.008\, Watts$$

The STE flow loop pump's power consumption was measured by using ohm's law to calculate the power based upon the voltage across the DC motor and the current supplied to the motor. The current supplied to the motor was measured by placing a precision resistor in line with the supply voltage line, and measuring the voltage drop across this resistor. The precision resistor's resistance was 0.5Ω ± 0.005Ω. The voltage measured across this resistor was in the 0-

1 *Volt* range. Voltages were measured using the HP 34970 DAQ. The equation used to calculate the current is:

$$I = \frac{V_1}{R}$$

The uncertainty of the first voltage measurement (for current calculation purposes) is:

$$u_{V_1} = 0.00009\,V$$

The uncertainty of the current measurement is:

$$u_I = \sqrt{\left(\frac{\partial I}{\partial V_1}u_{V_1}\right)^2 + \left(\frac{\partial I}{\partial R}u_R\right)^2} = \sqrt{\left(\frac{u_{V_1}}{R}\right)^2 + \left(-\frac{V_1}{R^2}u_R\right)^2} = 0.020000\,Amps$$

The power measurement is calculated by:

$$P = IV_2$$

The voltage measured was 0-25 *V* with the data acquisition measuring in the 0-100 *V* range. The uncertainty of the second voltage measurement (for power calculation purposes) is:

$$u_{V2} = 0.0051\,V_2$$

The uncertainty of the power measurement is therefore:

$$u_{power} = \sqrt{\left(\frac{\partial P}{\partial I}u_I\right)^2 + \left(\frac{\partial P}{\partial V}u_{V_2}\right)^2} = \sqrt{(Vu_I)^2 + (Iu_{V_2})^2} = 0.50000\,Watts$$

Weight

As stated in the experimental setup chapter, all weight measurements were recorded using an Arlyn Scales model SAW-H high accuracy Surface Acoustic Wave scale. The manufacturer's stated accuracy is ±0.01% full scale which results in an uncertainty of ±0.0088 *kg*.

IEC Efficiency Measurements

The IEC energy efficiency is calculated by summing the product of the instantaneous power consumption of the dryer multiplied by the discrete time step of the data. This quantity is then divided by the dry weight of the test load:

$$IEC = \frac{\sum P_n \cdot \Delta t_n}{W_o}$$

We assume that the uncertainty of the time measurement is nil since the time step is from the computer's clock. We also assume that the uncertainty of the weight does not significantly affect the measurement. The uncertainty of the IEC efficiency is therefore:

$$u_{IEC} = \frac{\sum u_P}{W_o}$$

This uncertainty is affected by each test length, as shown in Table A..

Table A.1 IEC Efficiency Uncertainties

Data Set	Uncertainty (kWh/kg)
Baseline 1	0.001301
Baseline 2	0.001271
Baseline 3	0.001302
Baseline 4	0.001277
Baseline 5	0.001283
STE 1	0.001239
STE 2	0.001242
STE 3	0.001171
STE 4	0.001206
STE 5	0.001237

Bubble-Point Experimental Uncertainties

The sources of uncertainty in the Bubble-Point measurements were the pressure measured by the transducer, the temperature of the IPA, and the immersion depth of the STE in IPA. As previously stated in Chapter 4, the pressure transducer used in the Bubble-Point Tests was first calibrated using a micro-manometer in the range of 0-10 inches of water column. Table A.2 shows the data from this calibration.

Table A.2 Pressure Transducer Calibration Data

Pressure (psi)	Measured Voltage (volts)	Trend-line Voltage (volts)	Deviation
0	0.0010854	0.0011	-0.0000146
0.036127292	0.0014614	0.001454047	7.35254E-06
0.072254584	0.0018143	0.001808095	6.20508E-06
0.108381876	0.0021735	0.002162142	1.13576E-05
0.144509168	0.0025483	0.00251619	3.21102E-05
0.18063646	0.0028697	0.002870237	-5.37308E-07
0.216763752	0.0032476	0.003224285	2.33152E-05
0.252891044	0.0035765	0.003578332	-1.83223E-06
0.289018336	0.0039499	0.00393238	1.75203E-05
0.325145628	0.0042804	0.004286427	-6.02715E-06
0.36127292	0.0046691	0.004640475	2.86254E-05

This range was used because the pressures encountered in bubble-point testing never exceeded 0.35 *psi*. Figure A.1 shows the calibration data points with the calibration equation fitted to the data.

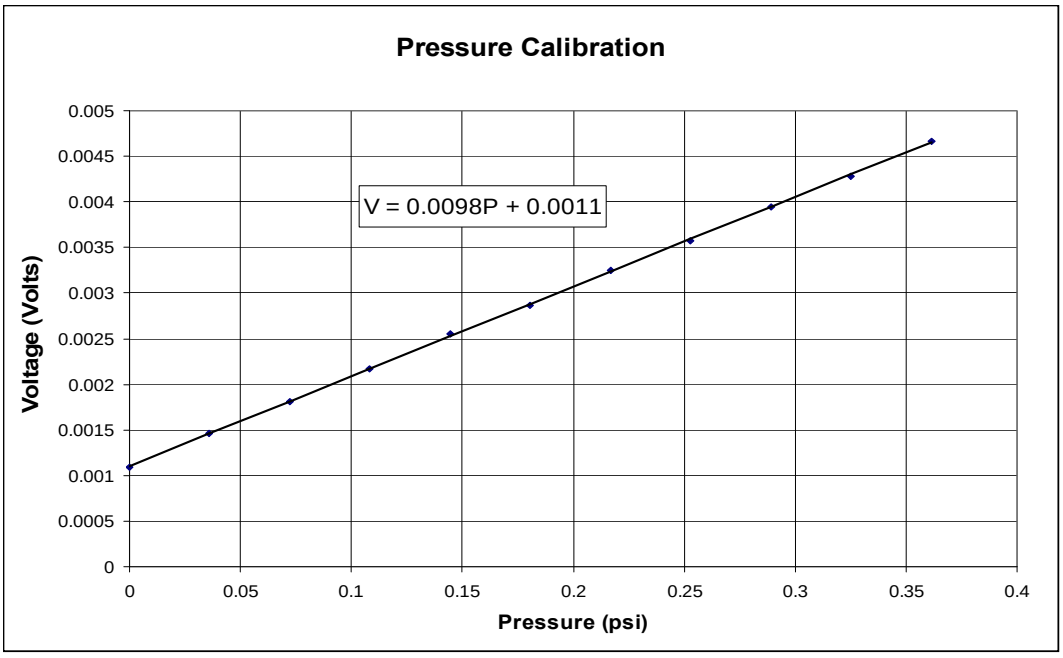

Figure A.1 Pressure Transducer Calibration Data and Calibration Equation

Rearranging the calibration equation, one obtains the working equation for the pressure measured by the transducer where V is in *volts* and P is in *psi*:

$$P = 102.04082V - 0.11224490 \qquad \textbf{Equation 56}$$

The accuracy of the pressure transducer is stated by the manufacturer as ±0.1% BFSL. According to Table A.2, the maximum pressure measurement for the bubble-point calibration had a voltage reading of 0.0046691 *Volts*, the standard uncertainty is therefore:

$$u_{\text{stan}} = (0.1\%)reading = (0.001)\cdot 0.0046691V = 4.6691\cdot 10^{-6}V$$

The calibration data acquisition equipment is a 12-bit A/D converter operating in the 0-50 *mV* range, thus the resolution uncertainty is:

$$u_{res} = \left(\frac{0.05V}{2^{12}\,states}\right)\frac{1}{2} = 1.2207\cdot 10^{-5}V$$

The linearity uncertainty for the calibration is:

$$u_{lin} = t_{95,9}S_{yx} = (2.262)(1.9924\cdot 10^{-5}) = 4.5068\cdot 10^{-5}V$$

Thus, the uncertainty in the voltage measured is:

$$u_{volt} = \sqrt{u_{s\,\text{tan}}^2 + u_{res}^2 + u_{lin}^2} = 4.6925\cdot 10^{-5}V$$

Therefore, the uncertainty in the pressure measurement is:

$$u_{transducer,total} = 102.04082(u_{volt}) = 0.0047883\,psi$$

The temperature measurement was made with a T-type thermocouple. The thermocouple's voltage output was measured by the data acquisition which has an overall uncertainty of ±1°C, stated by the manufacturer. This temperature measurement is used to read the surface tension of the IPA test liquid off of a chart provided in the SAE ARP901A document. The temperature throughout the experiment was constant, giving a surface tension of 0.000122848 $\frac{lbf}{in}$. An uncertainty of reading the values off of the figure is assumed to be ±0.2 *dynes/cm*, taking into account the temperature uncertainty of the above temperature measurement. This translates into:

$$u_{\sigma,total} = 1.142029\cdot 10^{-6}\,\frac{lbf}{in}$$

The temperature measurement is also used to read the density of IPA off of a chart. The temperature throughout the experiment was constant, giving a density for the IPA of 0.028229866 $\frac{lbf}{in^3}$. An uncertainty of reading the values off the chart is assumed to be ±0.01

grams/cm^3, taking into account the temperature uncertainty of the above temperature measurement. This translates into:

$$u_{\rho,total} = 3.6127 \cdot 10^{-4} \frac{lb}{in^3}$$

The immersion depth of the STE was made with a ruler having a resolution of $^1/_{16}$ of an inch. The average immersion depth was 0.5625 inches. The uncertainty of the immersion depth due to resolution is therefore:

$$u_{h,total} = \frac{1}{16} inch \cdot \frac{1}{2} = \frac{1}{32} inch$$

The corrected bubble-point pressure is determined by:

$$P = P_{transdu} - \rho_{IPA}\, gh_{immersion}$$

The uncertainty of the corrected bubble-point pressure is:

$$u_{bp\_corrected} = \sqrt{\left(\frac{\partial P}{\partial P_{bp}} u_{transducer,total}\right)^2 + \left(\frac{\partial P}{\partial \rho} u_{\rho,total}\right)^2 + \left(\frac{\partial P}{\partial h} u_{h,total}\right)^2}$$

$$u_{bp\_corrected} = \sqrt{\left(u_{transducer,total}\right)^2 + \left(-gh \cdot u_{\rho,total}\right)^2 + \left(-\rho g \cdot u_{h,total}\right)^2}$$

$$u_{bp\_corrected} = \sqrt{\left(.0047883 \frac{lbf}{in^2}\right)^2 + \left(-0.00020321 \frac{lbf}{in^2}\right)^2 + \left(-0.00088218 \frac{lbf}{in^2}\right)^2}$$

$$u_{bp\_corrected} = 0.0048731 \frac{lbf}{in^2}$$

And the micron rating is determined by:

$$D = \frac{4\sigma}{P}$$

Therefore, the uncertainty of the micron rating is:

$$u_{micron} = \sqrt{\left(\frac{\partial D}{\partial \sigma} u_{\sigma,total}\right)^2 + \left(\frac{\partial D}{\partial P} u_{bp\_corrected}\right)^2}$$

$$u_{micron} = \sqrt{\left(\frac{4}{P} u_{\sigma,total}\right)^2 + \left(-\frac{4\sigma}{P^2} u_{bp\_corrected}\right)^2}$$

$$u_{micron} = \sqrt{\left(0.000012645in\right)^2 + \left(-0.000018347in\right)^2} = 0.000022282in = 0.56597\mu m$$

Appendix B - STE Apparatus Engineering Drawings

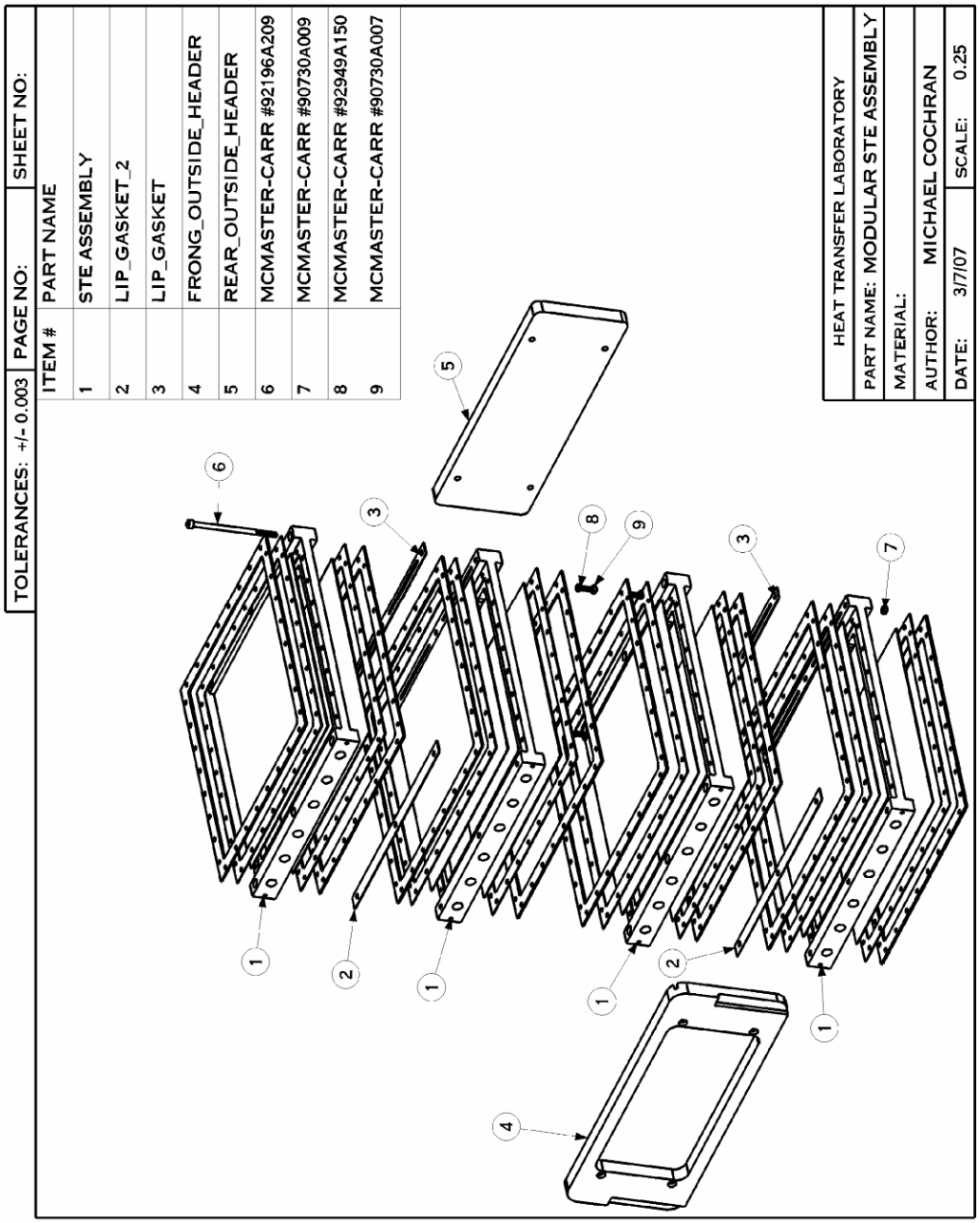

Figure B.1 STE Drawing 1

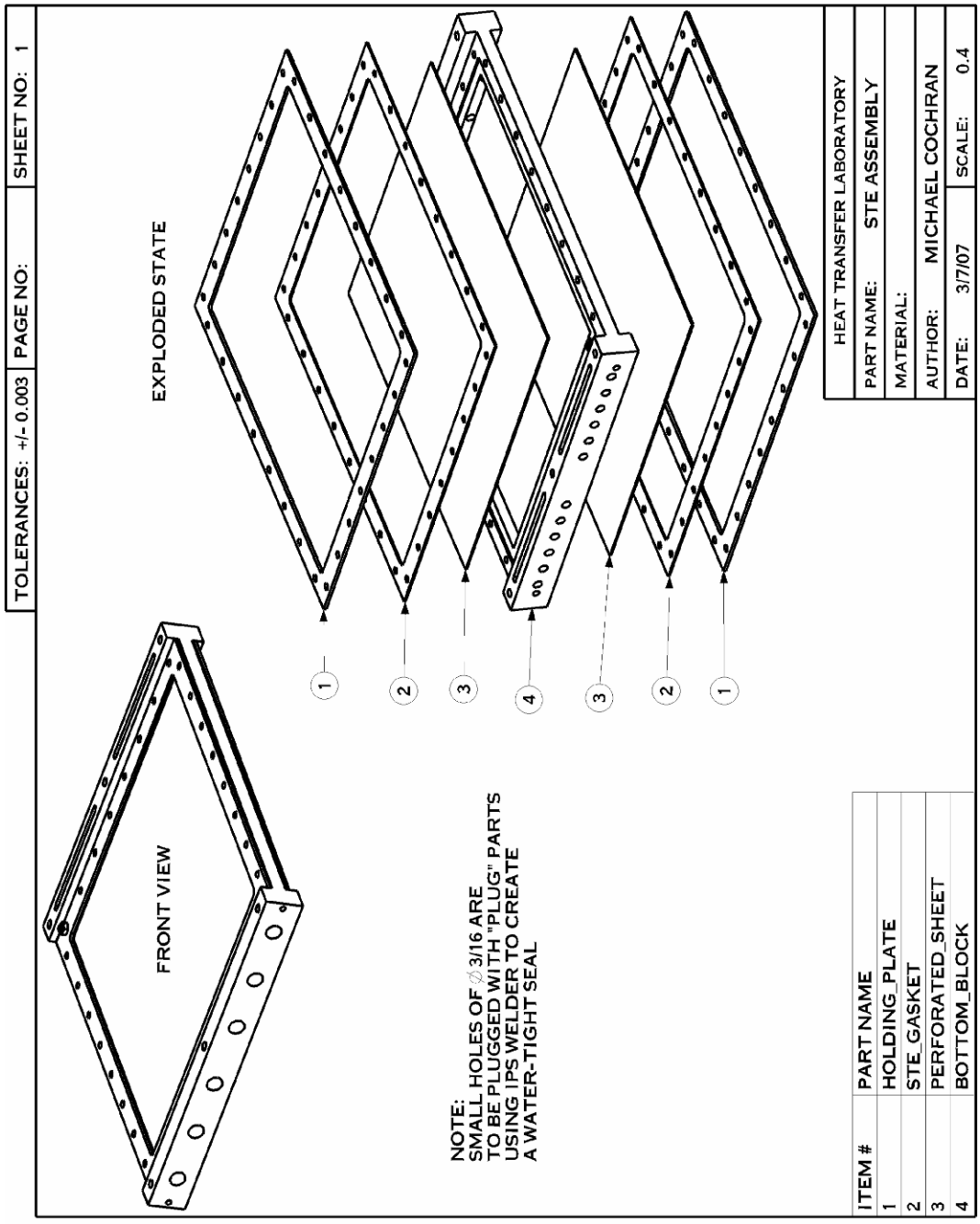

Figure B.2 STE Drawing 2

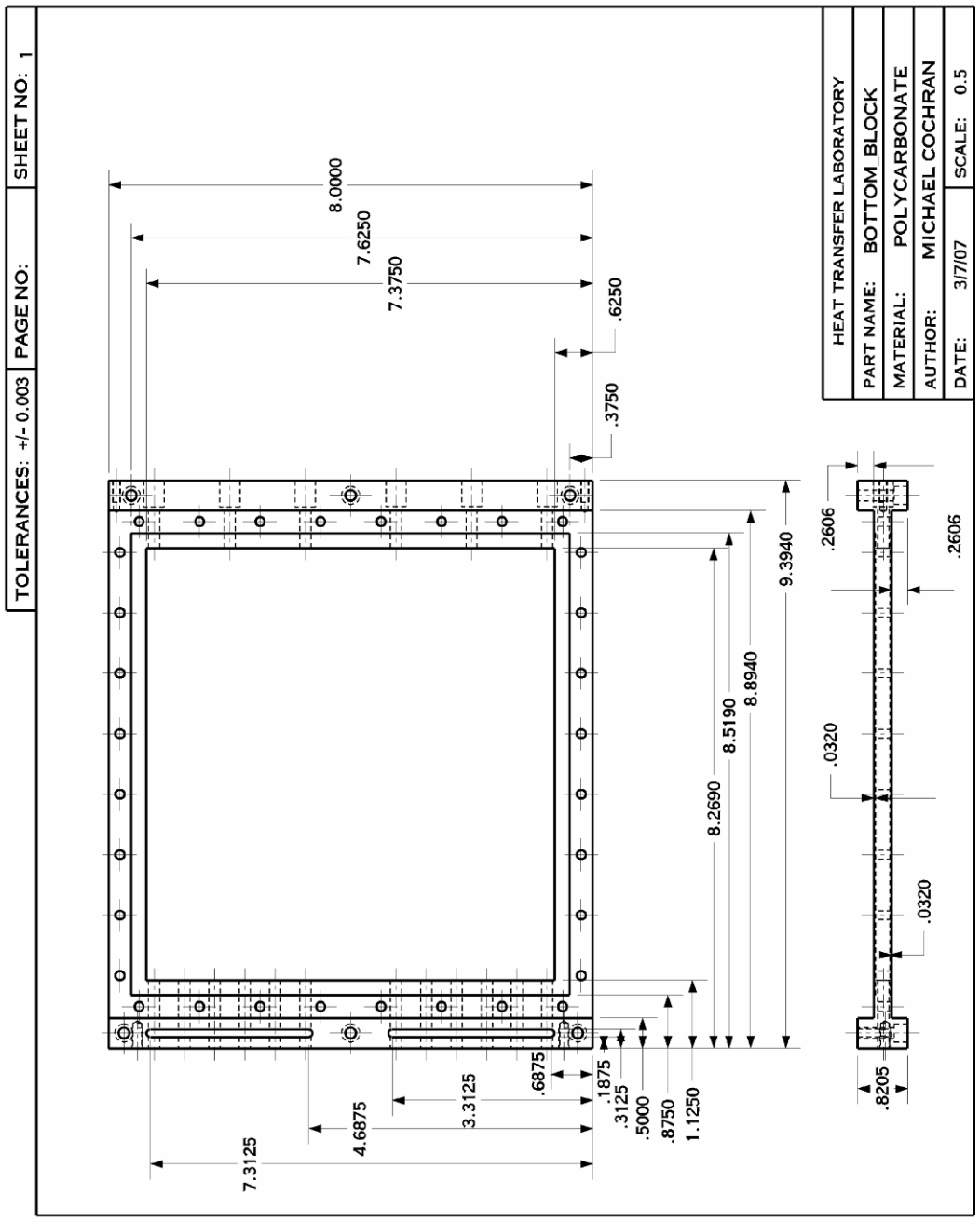

Figure B.3 STE Drawing 3

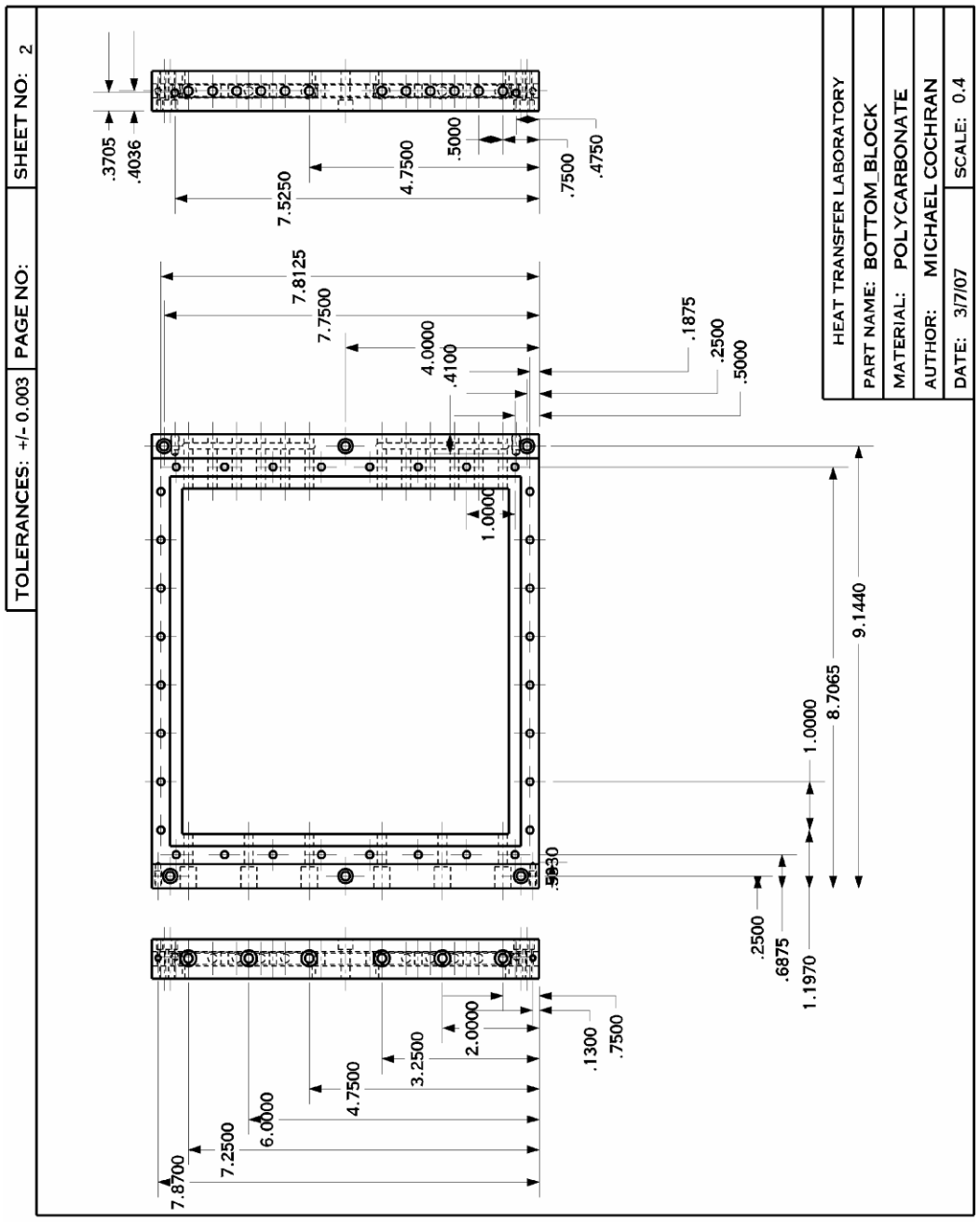

Figure B.4 STE Drawing 4

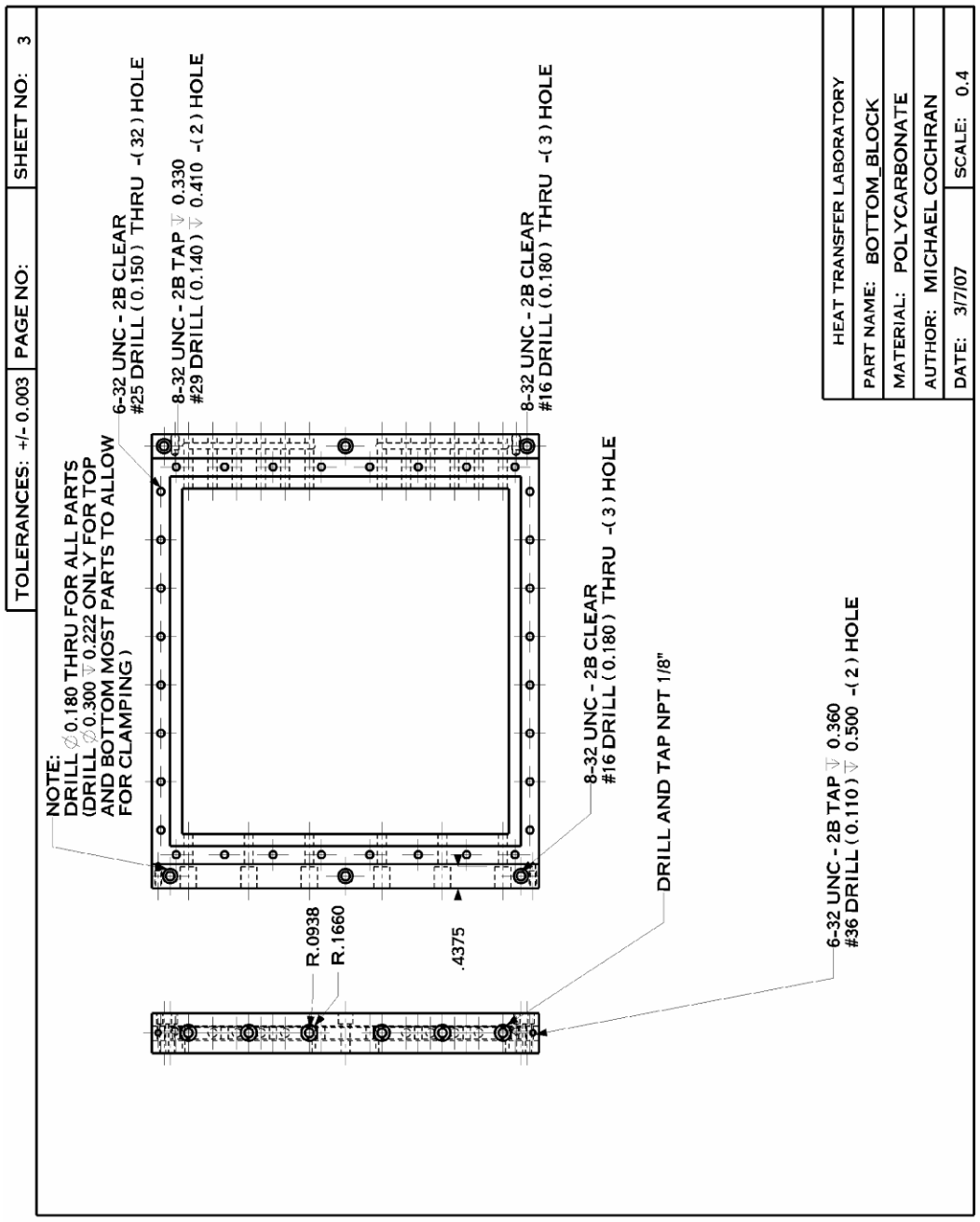

Figure B.5 STE Drawing 5

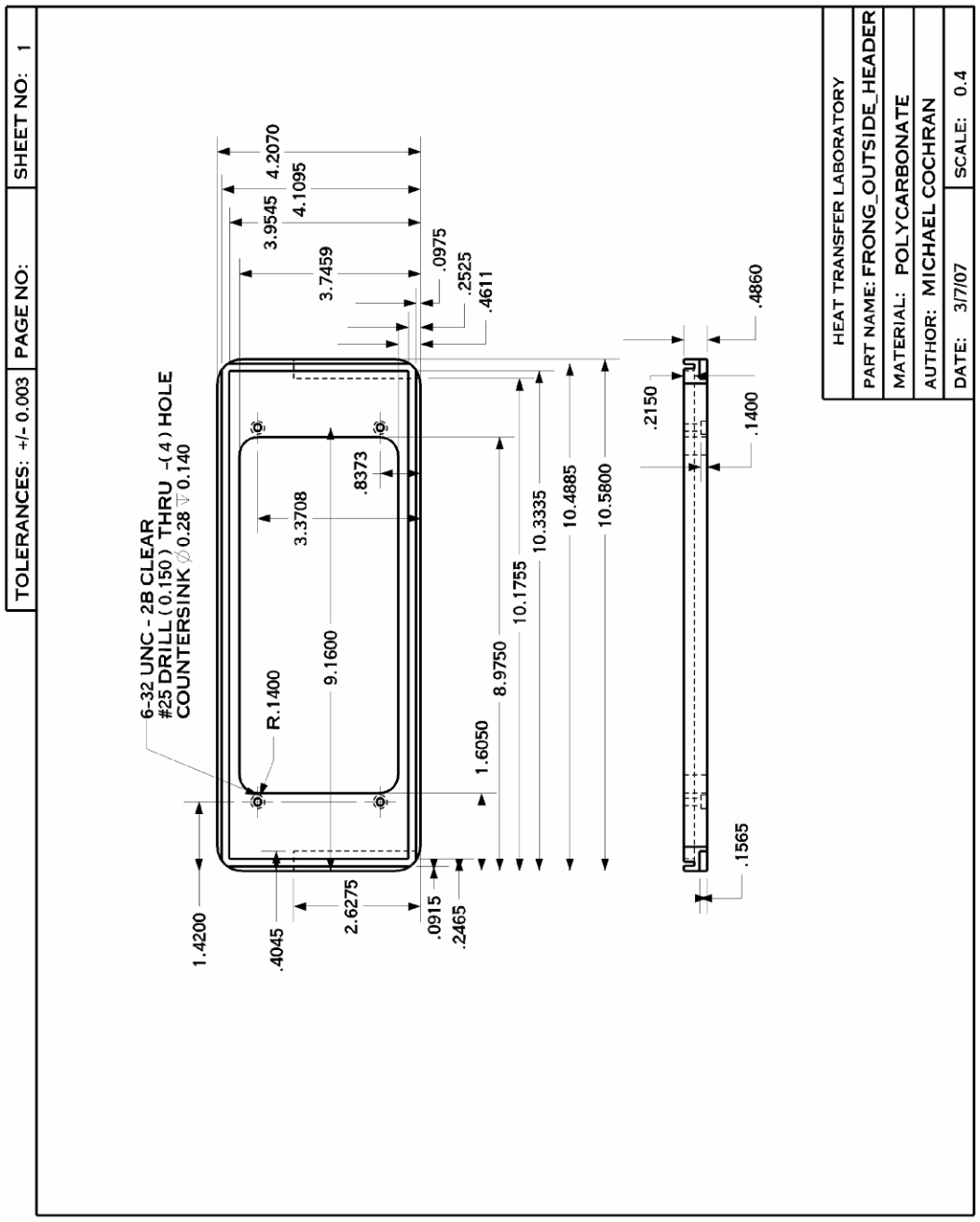

Figure B.6 STE Drawing 6

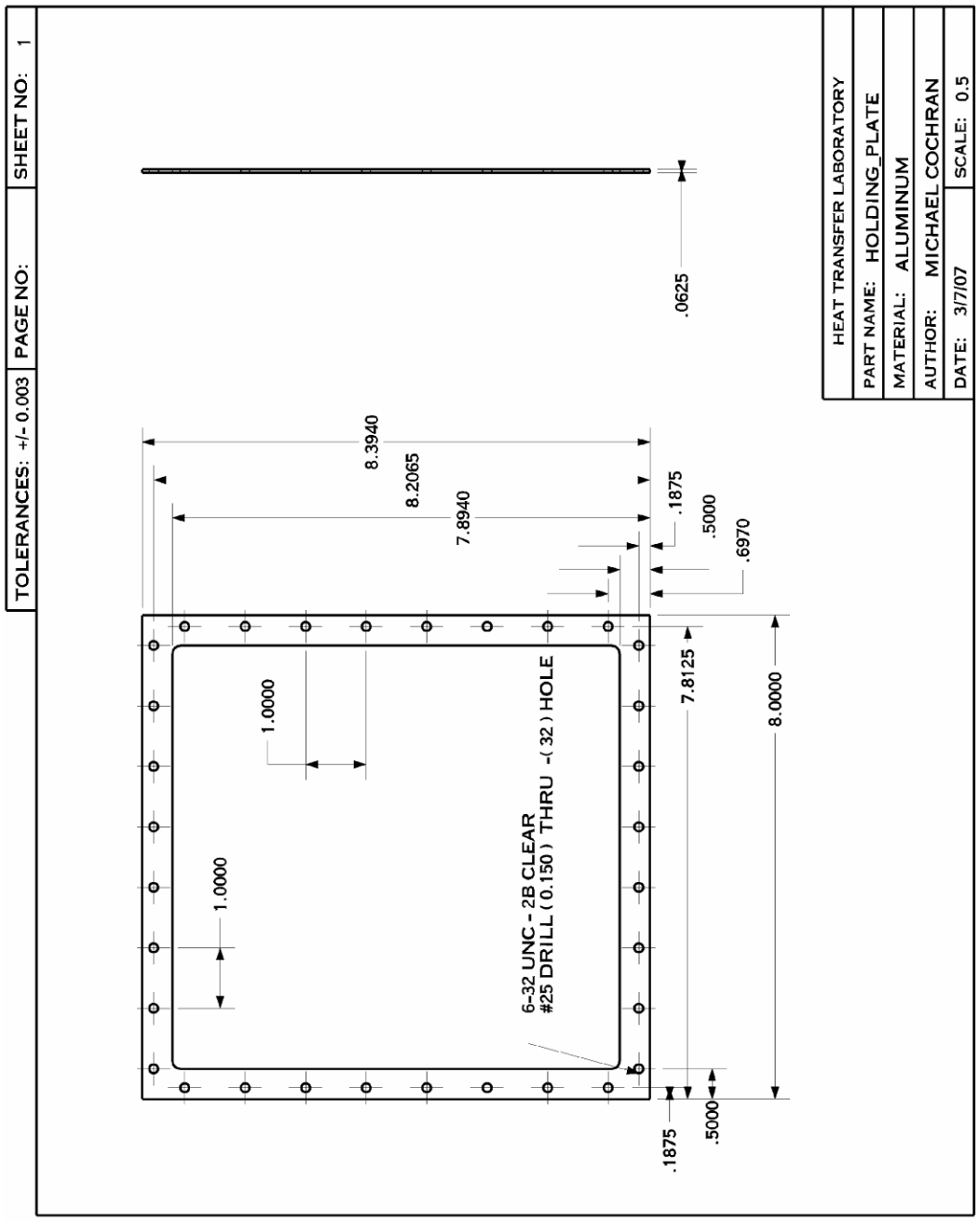

Figure B.7 STE Drawing 7

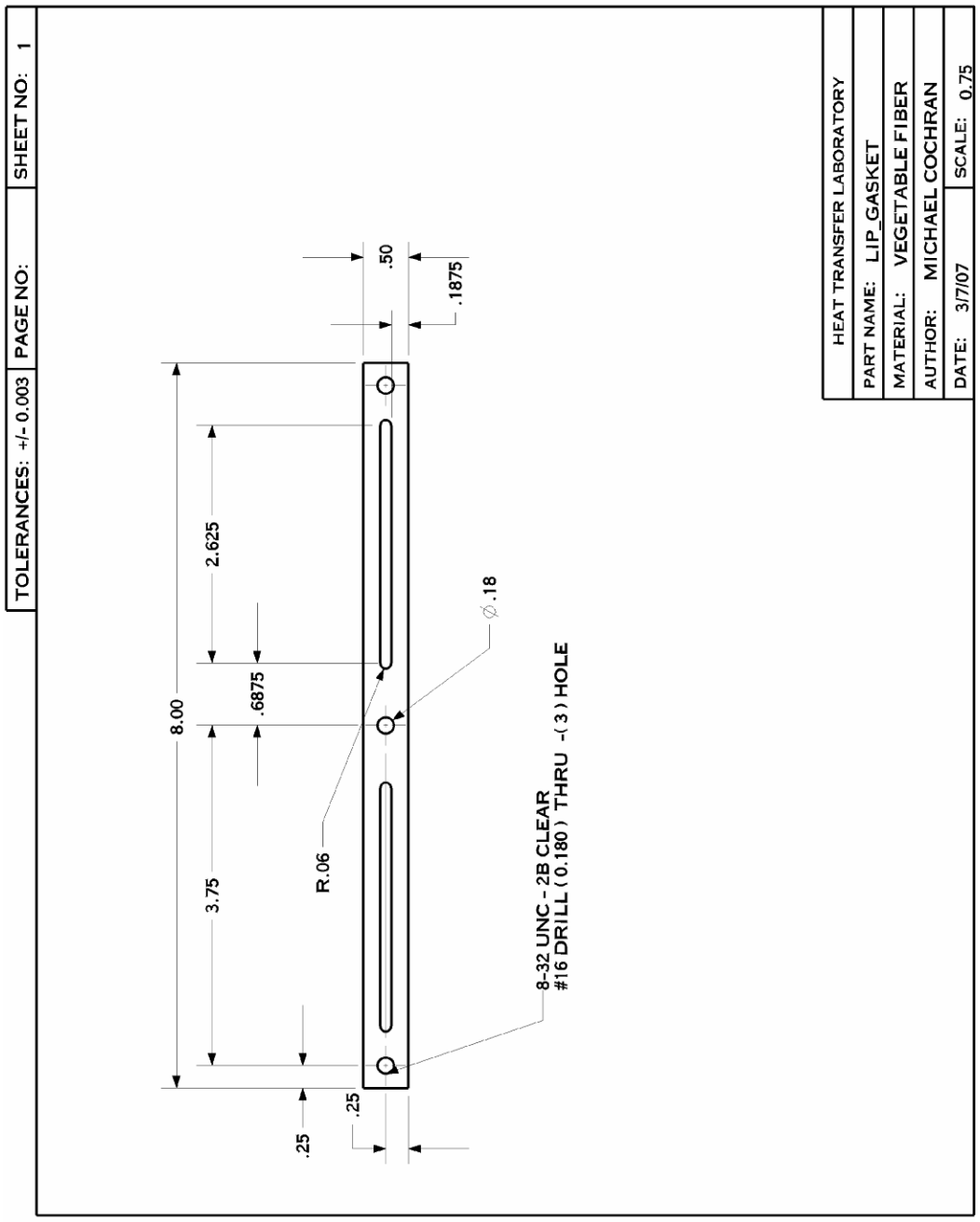

Figure B.8 STE Drawing 8

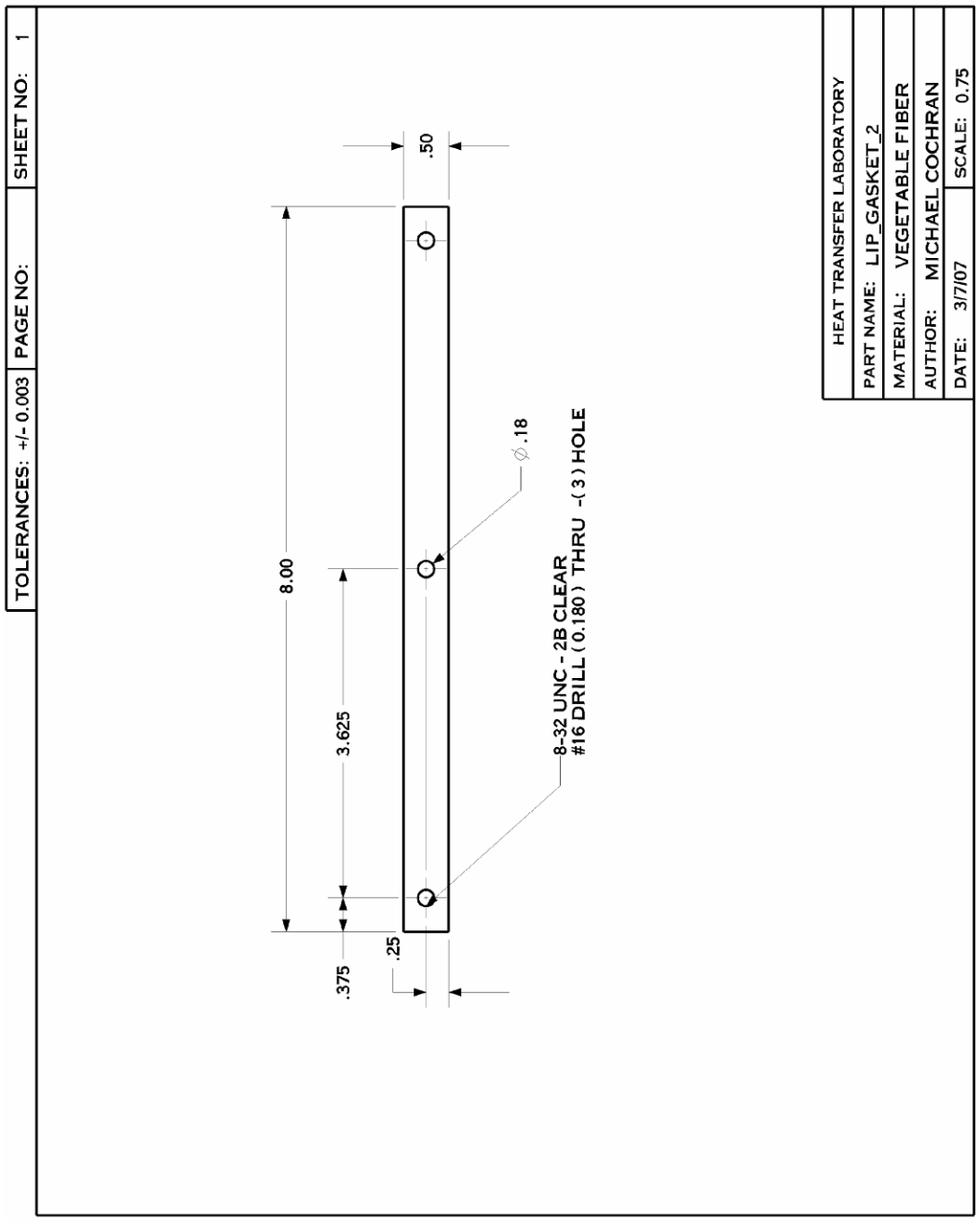

Figure B.9 STE Drawing 9

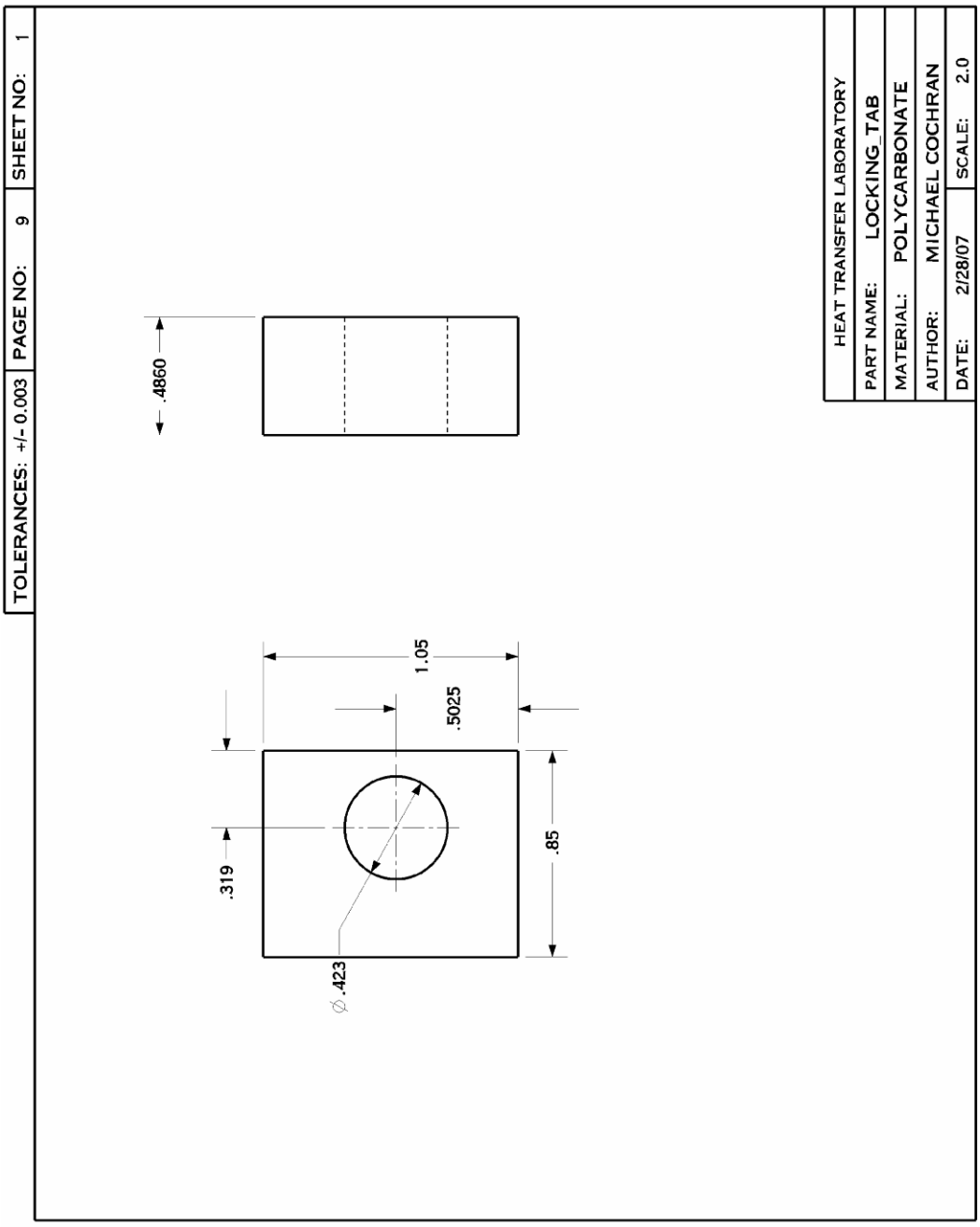

Figure B.10 STE Drawing 10

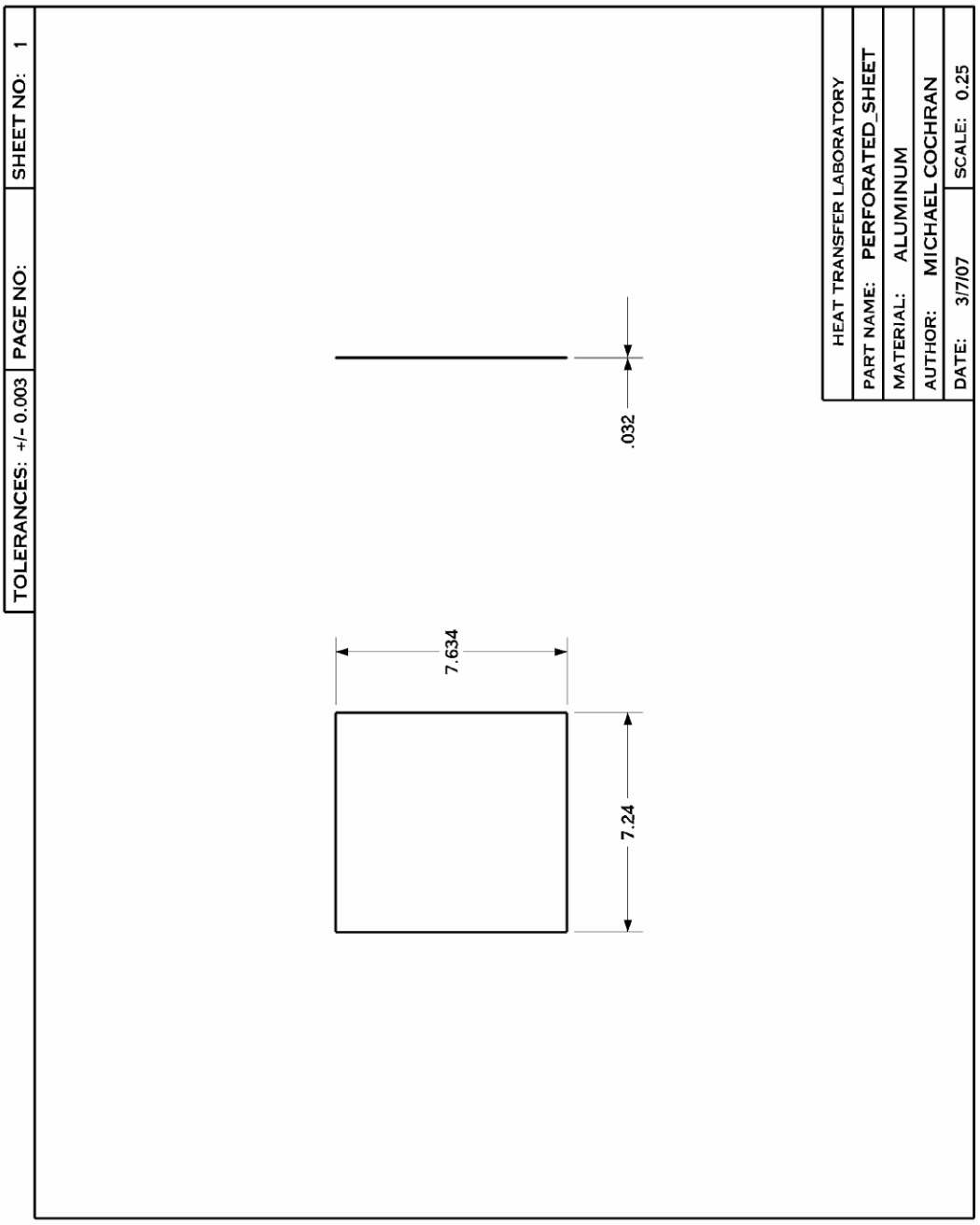

Figure B.11 STE Drawing 11

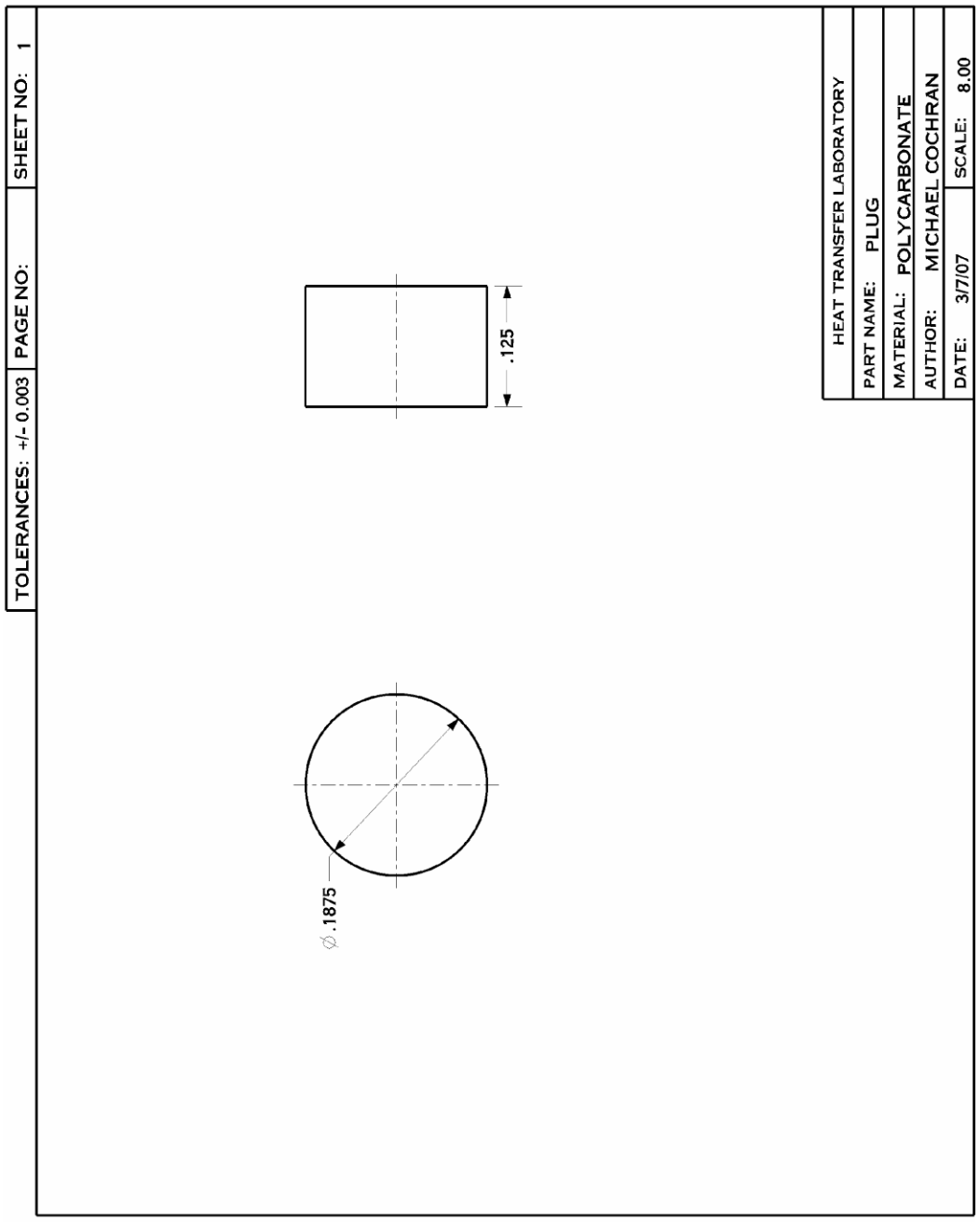

Figure B.12 STE Drawing 12

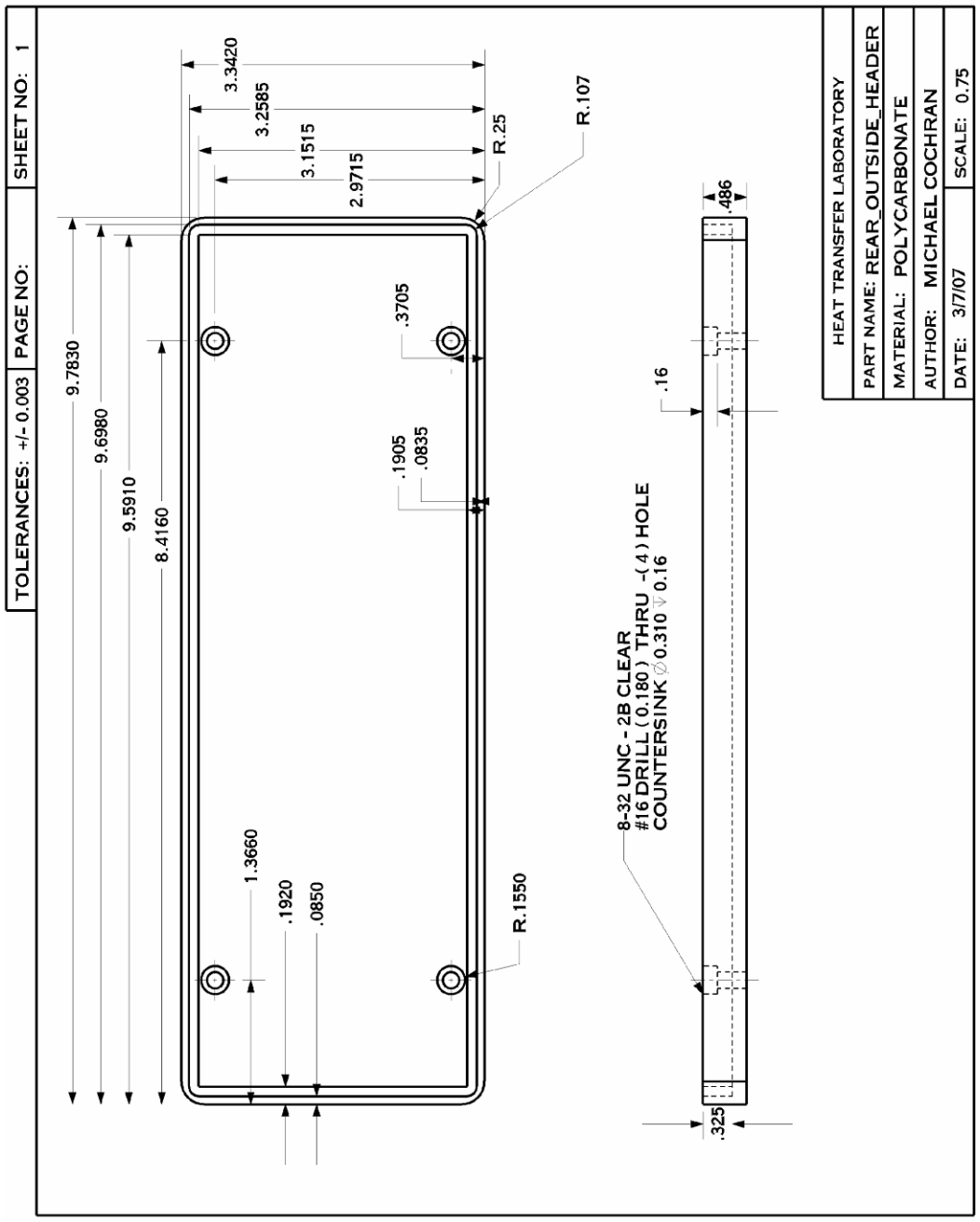

Figure B.13 STE Drawing 13

Appendix C - MATLAB m-file code

STE.m

```
%--------------------------------------------------------------------------
% File Name:  STE.m
% Author: Michael Cochran
% Date: 6-11-2007
% Matlab Version: 7.1
%
% Notes:  This function calculates key properties for the analytical model
% that predicts the moisture removal operation of a STE
%--------------------------------------------------------------------------

% Input Drying Fluid Properties
Drying_Fluid_Temp = 55.933;     % Air Dry Bulb Temp, deg C
Drying_Fluid_Pres = 101.574;    % Air Pressure, kPa
Drying_Fluid_w = .105;          % Air Humidity Ratio, kg H2O/kg Dry Air
Water_Temp = 35.924;            % STE Flow Loop Water Temp, deg C
Water_Flow = 3/39.65/1000;      % Volumetric Flow Rate, m^3 / s

% Drying Fluid Properties
Drying_Fluid_Flow = 195/3600;   % Volumetric Flow Rate, m^3 / s

% Drying Fluid Flow Characteristics
e = 0.5/1000;                   % Surface Roughness, m
A_flow = 0.01162;               % STE Cross-sectional Flow Area, m^2
A_channel = 0.002823;           % STE Channel Cross-section Flow Area, m^2
P_channel = .4529;              % STE Channel Wetted Perimeter, m
L = .2032;                      % Plate Length, m

% STE mass and heat transfer characteristics
As = 0.267137;                  % STE Condensation Surface Area, m^2
As_thermal = 0.34659;           % STE Thermal Surface Area, m^2

%--------------------------------------------------------------------------
% Calculate Drying Fluid Properties
% Note:  The following properties have the following dimensions:
% X_a - unitless air mole fraction
% X_w - unitless water mole fraction
% v - specific volume in (m^3)/kg
% cp - specific heat in kJ/(kg*K)
% mu - dynamic viscosity in (N*s)/(m^2)
% k - conductivity in W/(m*K)
% nu - kinematic viscosity in (m^2)/s
% alpha - thermal diffusivity in (m^2)/s
% Pr - unitless Prandlt number
% D - Binary Diffusion Coefficient (m^2)/s
```

```
% Sc - unitless Schmidt Number
%-------------------------------------------------------------------------
[mf_a,mf_w,X_a,X_w,v,cp,mu,k,nu,alpha,Pr,D,Sc] = ...
    Properties3(Drying_Fluid_Temp,Drying_Fluid_Pres,Drying_Fluid_w);

%-------------------------------------------------------------------------
% Calculate Drying Fluid Flow Characteristics
%-------------------------------------------------------------------------
Dh = 4*A_channel/P_channel;
V_STE = Drying_Fluid_Flow / A_flow;   % Drying Fluid Velocity, m/s
Re_Dh = V_STE*Dh/v/mu;

% Calculate darcy friction factor (see pg. 53, notes)
f = fzero(@(f)2.0*log10((e/Dh)/3.7 + 2.51/(Re_Dh*real(f^.5))) ...
    + 1/real(f^.5),.05);

% Calculate Entrance Length Effects (see pg. 61, notes)
C = 23.99*(Re_Dh^(-.230));
m = (-2.08e-6)*Re_Dh + 0.815;
f_entry = 1 + C/((L/Dh)^m);             % Entry-length correction factor

% Calculate Sherwood number based on heat-mass transfer analogy
Sh_Dh_FD = ((f/8)*(Re_Dh-1000)*Sc)/(1+12.7*((f/8)^.5)*((Sc^(2/3))-1));
Sh_Dh = Sh_Dh_FD*f_entry;

% Calculate mass transfer coefficient, m/s
hm = Sh_Dh*D/Dh;

% Calculate Nusselt number from Sherwood number (heat-mass transfer
% anology)
Nu_Dh_FD = ((f/8)*(Re_Dh-1000)*Pr)/(1+12.7*((f/8)^.5)*((Pr^(2/3))-1));
Nu_Dh = Nu_Dh_FD*f_entry;

% Calculate heat transfer coefficient, kW/m^2
h = Nu_Dh*k/Dh/1000;

% Calculate Water Properties at inlet
% v_water - m^3/kg
% psat_water - N/m^2
% sigma_water - N/m
[v_water,psat_water,sigma_water,Pr_water,k_water,mu_water,hfg_water...
    ] = H2O_Properties_1(Water_Temp);

% Setup up solving variables
Tw_in = Water_Temp + 273.15;
Tin = Drying_Fluid_Temp + 273.15;
win = Drying_Fluid_w;
R = 8.314/18.02;
Pin = Drying_Fluid_Pres;
Pout = Pin;
mdot = Drying_Fluid_Flow/v;
mdota = mdot*mf_a;
mdotv_in = mdot*mf_w;
mdotw_in = Water_Flow/v_water;
```

```
Psat_in = 1/1000*exp(-5800.2206/Tw_in+1.3914993-0.048640239*Tw_in...
    +0.000041764768*(Tw_in^2)-1.4452093e-8*(Tw_in^3)+...
    6.5459673*log(Tw_in));
Pv_in = win*Pin/(win + 0.62198);
hin = 1.006*(Tin-273.15)+win*(2501+1.805*(Tin-273.15));
hw_in = 4.187*(Tw_in - 273.15) + 0.0681;
hfg = 2501+1.805*(Tw_in-273.15)-(4.187*(Tw_in-273.15)+0.0681);
phiin = Pv_in/(1/1000*exp(-5800.2206/Tin+1.3914993-0.048640239*Tin...
    +0.000041764768*(Tin^2)-1.4452093e-8*(Tin^3)+...
    6.5459673*log(Tin)));
```

Properties3.m

```
%-------------------------------------------------------------------------
% File Name:  Properties3.m
% Author: Michael Cochran
% Date: 5-10-2007
% Matlab Version: 7.1
% Input Variables:  Moist Air Temperature in deg C (Tin), Pressure in kPa
% (Pin), and Humidity Ratio in kg H2O / kg Dry Air (win).
% Output Variables:
%       Air Mole Fraction
%       Water Vapor Mole Fraction
%
%
% Notes:  This function calculates the properties of a moist air mixture
% using the ideal gas assumption
%-------------------------------------------------------------------------

function [mf_a mf_w X_a X_w v cp mu k nu alpha Pr D Sc] = ...
    Properties3(Tin,Pin,win)

% Temperature in degrees K
T = Tin + 273.15;
% Pressure in kPa
P = Pin;
% Humidity Ratio in kg H2O / kg Dry Air
w = win;

% Constants
M_a = 28.9645;   % Molecular Weight of Dry Air - g/mol
M_w = 18.016;    % Molecular Weight of Water - g/mol
R = 8.314;      % Universal Gas Constant - J/(mol*K)

% Calculate Molar Fractions of Mixture
X_a = 1/(1 + 1.607793*w);
X_w = w/(0.62197058 + w);

% Calculate Mass Fractions of Mixture
mf_a = (X_a*M_a)/(X_a*M_a + X_w*M_w);
mf_w = (X_w*M_w)/(X_a*M_a + X_w*M_w);

% Calculate Molecular Weight of Mixture
M = X_a*M_a + X_w*M_w;
```

```
% Calculate specific volume of mixture
v = 8.314*T/P/M;

%*************************************************************************
% Calculate Thermodynamic Properties
%*************************************************************************

%-------------------------------------------------------------------------
% Specific Heat, cp ( kJ/(kg*K) )
cpair = (1.9327E-10*(T^4)-7.9999E-7*(T^3)+1.1407E-03*(T^2)-...
    0.4489*T+1057.5)/1000;
cpvapor = 8.314/18.02*(4.07-1.108e-3*T+4.152e-6*(T^2)-...
    2.964e-9*(T^3)+0.807e-12*(T^4));
cp = mf_a*cpair + mf_w*cpvapor;



%*************************************************************************
% Calculate Transport Properties
%*************************************************************************

%-------------------------------------------------------------------------
% Dynamic Viscosity, mu ( N*s/(m^2) )
%-------------------------------------------------------------------------
% Calculate Viscosity of Water Vapor at Temperature T
mu_w = -0.97494e-6 + T*0.359061e-7 + (T^2)*0.241612e-12;
% Calculate Viscosity of Dry Air at Temperature T
mu_a = 0.143387e-5 + T*0.656244e-7 - (T^2)*0.29905e-10;
% Calculate G functions
G_w_a = 0.277609*((1+1.12605*((mu_w/mu_a)^0.5))^2);
G_a_w = 0.2189366*((1+0.8880603*((mu_a/mu_w)^0.5))^2);
% Calculate Viscosity
mu = mu_a/(1+G_a_w*(X_w/X_a))+mu_w/(1+G_w_a*(X_a/X_w));

%-------------------------------------------------------------------------
% Thermal Conductivity, k ( W/(m*K) )
%-------------------------------------------------------------------------
% Calculate Conductivity of Water Vapor at Temperature T
k_w = -0.35376e-2 + T*0.654755e-4 + (T^2)*0.17446e-7;
% Calculate Conductivity of Dry Air at Temperature T
k_a = 0.669881e-3 + T*0.942482e-4 - (T^2)*0.327450e-7;
% Calculate G functions
G_w_a = 0.277609*((1+1.12605*((mu_w/mu_a)^0.5))^2);
G_a_w = 0.2189366*((1+0.8880603*((mu_a/mu_w)^0.5))^2);
% Calculate Conductivity
k = k_a/(1+G_a_w*(X_w/X_a))+k_w/(1+G_w_a*(X_a/X_w));

%-------------------------------------------------------------------------
% Kinematic Viscosity, nu ( m^2/s )
%-------------------------------------------------------------------------
nu = mu*v;

%-------------------------------------------------------------------------
% Thermal Diffusivity, alpha ( m^2/s )
%-------------------------------------------------------------------------
```

```
alpha = k/cp*v/1000;

%-------------------------------------------------------------------------
% Prandtl Number, Pr
%-------------------------------------------------------------------------
Pr = nu/alpha;

%-------------------------------------------------------------------------
% Coefficient of Binary Diffusivity of Water Vapor in Air, D ( (m^2)/s )
%-------------------------------------------------------------------------
if (T-273.15)<=80
    D = (104.91143e-6)*(T^1.744)/(P*1000);
elseif (T-273.15)>80 && (T-273.15)<300
    D = (805.2375e-6)/(P*1000)*(T^(5/2))/(T+190);
else
    error
end

%-------------------------------------------------------------------------
% Schmidt Number, Sc
%-------------------------------------------------------------------------
Sc = mu*v/D;
```

H2O_Properties_1.m

```
%-------------------------------------------------------------------------
% File Name:  H2O_Properties_1.m
% Author: Michael Cochran
% Date: 5-10-2007
% Matlab Version: 7.1
% Input Variables:  Water Temperature in deg C (Tin).
% Output Variables:
%
% Notes:  This function calculate liquid water properties solely as a
% function of temperature.
%-------------------------------------------------------------------------

function [v psat sigma Pr k mu hfg] = H2O_Properties_1(T)

% Calculate Density, kg/m^3
rho = -1.0362E-07*T^4 + 3.6196E-05*T^3 - 7.1802E-03*T^2 + 4.4255E-02*T ...
    + 9.9993E+02;
v = 1/rho;

% Calculate Dynamic Viscosity, N*s/m^2
mu = 4.0724E-15*T^6 - 1.5965E-12*T^5 + 2.6307E-10*T^4 ...
- 2.4281E-08*T^3 + 1.4378E-06*T^2 - 6.0171E-05*T + 1.7869E-03;
% Calculate Vapor Pressure, N/m^2
psat= 9.6495E-04*T^4 - 3.3243E-02*T^3 + 3.5535E+00*T^2 + 1.8204E+01*T ...
    + 6.6075E+02;
% Calculate Surface Tension, N/m
sigma = 1.5436E-09*T^3 - 4.9801E-07*T^2 - 1.3237E-04*T + 7.5590E-02;
% Calculate Prandtl Number
Pr = -5.7915E-12*T^6 - 3.4783E-10*T^5 + 5.5841E-07*T^4 - 1.0156E-04*T^3 ...
    + 8.7612E-03*T^2 - 4.3874E-01*T + 1.3008E+01;
```

```
% Calculate Thermal Conductivity
k = -7.1184E-06*T^2 + 1.8347E-03*T + 5.6806E-01;
% Calculate Heat of Vaporization
hfg = -1.3911E-03*T^2 - 2.2958E+00*T + 2.5010E+03;
```

MathCAD Model

Model Inputs

$T_{in} := 59 + 273.15$

Inlet Air Temperature, K

$\omega_{in} := .1121$

Inlet Air Humidity Ratio, kg H2O/kg Dry Air

$T_{w\_in} := 30 + 273.15$

STE Water Temperature, K

$h := 0.057134$

Heat Transfer Coefficient, kW/(m^2*K)

$h_m := 0.053671$

Mass Transfer Coefficient, m/s

$mdot := 0.054377$

Inlet Air Mass Flow Rate, kg/s

$mdot_{w\_in} := 0.075336$

Water Flow Rate, kg/s

Constants

$A_{mass} := 0.267137$

Mass Transfer Area, m^2

$A_{thermal} := 0.34569$

Heat Transfer Area, m^2

$R := \frac{8.314}{18.02}$

Water Gas Constant, kJ/(kg*K)

$P_{in} := 101.574$

Inlet Air Pressure, kPa

$$mf_{a\_in} := \frac{1}{1 + \omega_{in}}$$

$$mf_{a\_in} = 0.899$$

$$mf_{v\_in} := 1 - mf_{a\_in}$$

$$mf_{v\_in} = 0.101$$

$$mdot_a := mdot \cdot mf_{a\_in}$$

$$mdot_{v\_in} := mdot \cdot mf_{v\_in}$$

Calculate Water Vapor Saturation Pressure, kPa:

$$P_{sat\_in} := \frac{e^{\left(\frac{-5800.2206}{T_{w\_in}} + 1.3914993 - 0.048640239 T_{w\_in} + 0.000041764768 T_{w\_in}^2 - 1.4452093 \cdot 10^{-8} T_{w\_in}^3 + 6.5459673 \cdot \ln\left(T_{w\_in}\right)\right)}}{1000}$$

$$P_{out} := P_{in}$$

$$P_{v\_in} := \frac{\omega_{in} \cdot P_{in}}{\omega_{in} + 0.62198}$$

Water Vapor Partial Pressure, kPa

$$h_{in} := 1.006 \cdot \left(T_{in} - 273.15\right) + \omega_{in} \cdot \left[2501 + 1.805 \cdot \left(T_{in} - 273.15\right)\right]$$

$$h_{w\_in} := 4.187 \cdot \left(T_{w\_in} - 273.15\right) + 0.0681$$

$$h_{fg} := 2501 + 1.805 \cdot \left(T_{w\_in} - 273.15\right) - \left[4.187 \cdot \left(T_{w\_in} - 273.15\right) + 0.0681\right]$$

$$\phi_{in} := \frac{P_{v\_in}}{\frac{e^{\left(\frac{-5800.2206}{T_{in}} + 1.3914993 - 0.048640239 T_{in} + 0.000041764768 T_{in}^2 - 1.4452093 \cdot 10^{-8} T_{in}^3 + 6.5459673 \cdot \ln\left(T_{in}\right)\right)}}{1000}}$$

$$\phi_{in} = 0.815$$

Unknown guesses:

$$mdot_c := -.00005$$

$$P_{sat\_out} := P_{sat\_in} + 1$$

$$P_{v\_out} := P_{v\_in} - 1$$

$$\omega_{out} := \omega_{in} - .01$$

$$q := -.3$$

$$h_{w\_out} := h_{w\_in}$$

$h_{out} := h_{in}$

$T_{out} := T_{in} - 5$

$T_{w\_out} := T_{w\_in} + 5$

$\phi_{out} := \phi_{in}$

$h_c := 2532$

Given

Equation 1

$$mdot_c = h_m \cdot A_{mass} \cdot \left[\frac{\left(\frac{P_{sat\_out}}{R \cdot T_{w\_out}} - \frac{P_{v\_out}}{R \cdot T_{out}} \right) - \left(\frac{P_{sat\_in}}{R \cdot T_{w\_in}} - \frac{P_{v\_in}}{R \cdot T_{in}} \right)}{\ln \left[\frac{\left(\frac{P_{sat\_out}}{R \cdot T_{w\_out}} - \frac{P_{v\_out}}{R \cdot T_{out}} \right)}{\left(\frac{P_{sat\_in}}{R \cdot T_{w\_in}} - \frac{P_{v\_in}}{R \cdot T_{in}} \right)} \right]} \right]$$

Calculate Water Vapor Saturation Pressure, kPa

$$P_{sat\_out} = \frac{e^{\left(\frac{-5800.2206}{T_{w\_out}} + 1.3914993 - 0.048640239 T_{w\_out} + 0.000041764768 T_{w\_out}^2 - 1.4452093 \cdot 10^{-8} T_{w\_out}^3 + 6.5459673 \cdot \ln(T_{w\_out}) \right)}}{1000}$$

$$P_{v\_out} = \frac{\omega_{out} \cdot P_{out}}{\omega_{out} + 0.62198}$$

$$\omega_{out} = \frac{mdot_{v\_in} + mdot_c}{mdot_a}$$

Equation 2

$$q = h \cdot A_{thermal} \cdot \left[\frac{\left(T_{w\_out} - T_{out} \right) - \left(T_{w\_in} - T_{in} \right)}{\ln \left[\frac{\left(T_{w\_out} - T_{out} \right)}{\left(T_{w\_in} - T_{in} \right)} \right]} \right]$$

Equation 3 (STE Water CV Energy Balance)

Note: the direction of "q" is from the STE to the Air

$$q = mdot_{w\_in} \cdot h_{w\_in} - \left(mdot_{w\_in} - mdot_c \right) \cdot h_{w\_out} - mdot_c \cdot h_c$$

$$h_{w\_out} = 4.187 \cdot \left(T_{w\_out} - 273.15 \right) + 0.0681$$

$$h_c = 2501 + 1.805 \cdot \frac{\left[\left(T_{in} - 273.15 \right) + \left(T_{out} - 273.15 \right) \right]}{2}$$

Equation 4 (Air CV Energy Balance

$$-q = mdot_a \cdot \left(h_{in} - h_{out}\right) + mdot_c \cdot h_c$$

$$h_{out} = 1.006 \cdot \left(T_{out} - 273.15\right) + \omega_{out} \cdot \left[2501 + 1.805 \cdot \left(T_{out} - 273.15\right)\right]$$

Calculate Other Properties

$$\phi_{out} = \frac{P_{v\_out}}{\frac{e^{\left(\frac{-5800.2206}{T_{out}} + 1.3914993 - 0.048640239 T_{out} + 0.000041764768 T_{out}^{2} - 1.4452093 \cdot 10^{-8} T_{out}^{3} + 6.5459673 \cdot \ln\left(T_{out}\right)\right)}}{1000}}$$

$$\text{Find}\left(mdot_c, P_{sat\_out}, P_{v\_out}, \omega_{out}, q, h_{w\_out}, h_{out}, h_c, T_{out}, T_{w\_out}, \phi_{out}\right) =$$

	0
0	$-8.14796 \cdot 10^{-4}$
1	6.49472
2	13.51214
3	0.09544
4	-0.41112
5	157.56374
6	299.90088
7	$2.60114 \cdot 10^{3}$
8	325.10386
9	310.76539
10	0.99367

Constraint: if relative humidity is greater than 100%, place constraint above the find command, if not, place constraint below the find command.

$$\phi_{out} = 1$$